



Université du Québec  
Institut national de la recherche scientifique  
Centre Eau-Terre-Environnement

## Potentiel des systèmes de pompes à chaleur géothermique au Nunavik: aspects souterrains

Par  
Hubert Langevin

Mémoire présenté pour l'obtention du grade de  
Maître en sciences (M.Sc.)  
en Sciences de la Terre

### Jury d'évaluation

Président du jury et  
Examinateur interne

Jean-Michel Lemieux  
Université Laval

Examinateur externe

Andrew Wigston  
Ressources naturelles Canada

Directeur de recherche

Jasmin Raymond  
INRS – centre Eau-Terre-Environnement

Codirecteur de recherche

Louis Gosselin  
Université Laval

Codirecteur de recherche

Martin Bourbonnais  
Cégep de Jonquière



## **REMERCIEMENTS**

Je tiens à remercier mon directeur de recherche Jasmin Raymond pour ses conseils, sa disponibilité et pour son soutien dans les activités que j'ai entreprises que ce soit dans un contexte académique ou professionnel. Son ouverture d'esprit, son aide et sa patience m'ont permis de développer des compétences et de vivre des expériences qui me seront utiles à long terme. Je tiens aussi à remercier Nicolò Giordano pour les nombreux conseils et discussions qui ont été utiles pour compléter les différentes étapes du projet.

Merci à mes co-directeurs de maîtrise, Louis Gosselin et Martin Bourbonnais, pour leurs conseils et échanges qui ont permis d'améliorer la qualité de ce travail et d'enrichir mon apprentissage. Je tiens à également à remercier Jean-Michel Lemieux et Andrew Wigston pour l'évaluation de ce mémoire de maîtrise. Merci à Félix-Antoine Comeau de m'avoir accompagné en contribuant aux projets de recherche que j'ai entrepris depuis mon arrivée à l'INRS.

Je tiens à remercier les employés ainsi que des communautés de Whapmagoostui, de Kuujjuarapik et du Centre d'études nordiques ayant été impliqués dans ce projet.

Merci aux collègues à l'INRS et de l'Université Laval pour avoir partagé les séances d'études et pour collaborer de près ou de loin à ce projet. Ces discussions ont significativement enrichi cette expérience.

Claudia, ton soutien inconditionnel et ta compréhension m'auront permis de réaliser des projets que je n'aurais pas cru possibles et je t'en remercie infiniment. Finalement, je dédie un immense merci à ma famille et mes amis pour leur constant soutien et leurs encouragements qui sont une partie essentielle de mon cheminement.

## RÉSUMÉ

Les communautés nordiques sont alimentées avec des micro-réseaux énergétiques autonomes et dépendant des énergies fossiles, utilisés pour fournir le chauffage et l'électricité. Elles doivent alors trouver des solutions permettant d'intégrer diverses énergies renouvelables afin de réduire leur consommation en diesel. Les systèmes géothermiques assistés par des panneaux solaires photovoltaïques (PV), tels que les pompes à chaleur géothermique couplées à des échangeurs de chaleur conventionnels à boucle fermée verticale (BHE) ou des systèmes d'emmagasinement thermique souterrain (BTES), présentent un fort potentiel. Ces systèmes permettent de réaliser des économies d'énergie pour le chauffage en extrayant une partie de l'énergie thermique à partir du sol tout en utilisant de l'électricité dérivée d'autres formes d'énergies renouvelables. Cependant, plusieurs défis techniques et économiques caractérisent les régions nordiques comme le Nunavik et il est nécessaire d'offrir des outils pouvant contribuer à améliorer la conception de ces systèmes.

Une nouvelle méthode pour réaliser un essai de réponse thermique oscillatoire (O-TRT) utilisant un câble chauffant a été développée afin d'estimer les propriétés thermiques des matériaux géologiques meubles. La méthode a été utilisée avec un matériel standardisé en laboratoire et sur le terrain dans un dépôt naturel sableux pour estimer leur conductivité et diffusivité thermique respective à l'aide d'une approche analytique. Cette approche a également été validée à l'aide d'une méthode numérique pour constater que l'approche analytique permet de déterminer des valeurs de propriétés thermiques avec moins de 2% de différence. L'importance d'utiliser des valeurs de propriétés thermiques exacte a été étudiée dans une étude paramétrique. Cette étude a été utilisée pour comprendre les principaux paramètres affectant le dimensionnement d'un BTES en climat subarctique. Ces résultats ont été intégrés dans une troisième étude afin de comparer leur efficacité et leur potentiel d'implémentation au Nunavik comparativement à des BHE. Des observations de terrain ont été utilisées pour développer des modèles numériques complexes simulant l'opération de ces systèmes géothermiques assistés ou non par des PV et couplés à des pompes à chaleur géothermique afin de déterminer leur consommation et leurs coûts énergétiques. L'option la plus rentable lorsque le système n'est pas assisté par des PV est une pompe à chaleur alimentée par une énergie fossile couplée à un BHE. Lorsque le système est assisté par une quantité suffisante de PV, il devient pertinent d'utiliser des pompes à chaleur alimentées par électricité couplées à : un BHE pour répondre à une faible demande en chauffage en raison de la température du sol près du point de congélation de l'eau et des charges du bâtiment qui sont déséquilibrées ; ou encore un BTES pour répondre à une demande en chauffage élevée puisque l'injection de chaleur dans le sol permet de rééquilibrer le bilan thermique du sous-sol débalancé par la demande du bâtiment.

## AVANT-PROPOS

Ce mémoire de maîtrise est composé d'une synthèse des travaux de recherche et présente trois chapitres. Le chapitre 1 correspond à un article soumis à la revue *International Journal of Heat and Mass Transfer* décrivant la méthode et les résultats des O-TRT qui ont été développés au cours de ce projet. Ce chapitre a une valeur importante au sein du projet de maîtrise puisqu'il décrit une méthode novatrice développée pour estimer la conductivité thermique et la capacité thermique volumique de différents matériaux, mais aussi pour simuler l'opération des systèmes géothermiques aux chapitres 2 et 3. De plus, cette nouvelle méthode possède un bon potentiel de développement dans le domaine de la géothermie comme elle présente plusieurs avantages pour estimer les propriétés thermiques comparativement aux méthodes conventionnelles utilisées. Le chapitre 2 est un article de conférence présenté au 2<sup>nd</sup> Canadian Geothermal Students' Days dévoilant les résultats d'une étude paramétrique sur la performance de BTES en contexte subarctique. Ce chapitre est une étude permettant de comprendre l'influence des paramètres simulés sur la performance des BTES dans le chapitre 3. Le chapitre 3 est un article prêt à soumettre comparant l'efficacité et la consommation énergétique de pompes à chaleur couplées à des BTES et des BHE en région nordique. Ces trois chapitres attestent des développements encourus dans ce projet de maîtrise.

- Chapitre 1: Article soumis dans la revue International Journal of Heat and Mass Transfer.  
*Oscillatory thermal response test using heating cables: a novel method for in situ thermal property analysis.*
- Chapitre 2: Article de conférence présenté au 2<sup>nd</sup> Canadian Geothermal Students' Days. *Design considerations for thermal energy storage systems in subarctic climate.*
- Chapitre 3: Article prêt à soumettre. *Solar assisted geothermal to reduce diesel consumption in off-grid communities in a subarctic climate: comparison between borehole thermal energy storage and borehole heat exchanger systems in Nunavik, Canada*

## TABLE DES MATIÈRES

REMERCIEMENTS .....	ii
RÉSUMÉ.....	iii
AVANT-PROPOS .....	iv
LISTE DES TABLEAUX .....	viii
LISTE DES FIGURES .....	ix
NOMENCLATURE.....	xiii
I. Synthèse .....	1
1. Introduction .....	2
2. Définition du problème .....	6
3. Objectifs .....	8
4. Approche méthodologique .....	8
II. Articles.....	10
Chapitre 1 .....	11
1.1 Introduction.....	13
1.2 Material and methods.....	17
1.2.1 Analytical Approach.....	17
1.3 Experimental .....	21
1.3.1 Ottawa sand C-109 .....	21
1.3.2 Whapmagoostui-Kuujjuarapik sand .....	21
1.3.3 Analytical approach correction.....	23
1.3.4 Numerical approach validation.....	23
1.3.4.1 Ottawa sand C-109 .....	24
1.3.4.2 Whapmagoostui-Kuujjuarapik sand .....	26
1.4. Results.....	27
1.4.1 Ottawa sand C-109 .....	27

1.4.2 Whapmagoostui-Kuujjuarapik sand .....	29
1.5 Discussion .....	30
1.6 Conclusions.....	34
Chapitre 2 .....	36
2.1 Introduction.....	38
2.2 Methods.....	38
2.3 Results.....	42
2.4 Discussion.....	44
2.5 Conclusions.....	45
Chapitre 3 .....	46
3.1. Introduction .....	49
3.2. Geographical, hydro-, and thermo-geological setting .....	52
3.3. Method .....	54
3.3.1 Conceptual Models .....	54
3.3.2 Fluid flow mechanisms .....	61
3.3.3 Heat transfer mechanisms .....	61
3.3.4 Domain discretization .....	62
3.3.5 Input parameters.....	62
3.3.6 Models boundary conditions.....	68
3.3.7 Initial conditions and simulation procedure.....	71
3.3.8 Energy consumption and costs.....	73
3.4. Results .....	74
3.4.1 Simulated geothermal systems.....	74
3.4.2 Comparison between scenarios .....	77
3.5. Discussion .....	83
3.5.1 Assumptions and uncertainty for the simulated geothermal systems .....	83
3.5.2 Geothermal systems in northern climate.....	84

3.6. Conclusions .....	86
III. Conclusions .....	87
1. Synthèse des résultats .....	88
2. Conclusions du mémoire de maîtrise .....	90
Références .....	92
IV. Annexes.....	99
Annexe I - Numerical models calibration .....	100
Annexe II – Analyses détaillées des essais de réponse thermique oscillatoires .....	103
Annexe III – Subsurface georadar assessment at the CEN research station.....	106
Annexe IV – Regional hydrogeological numerical model .....	108
Annexe V – Ground temperature monitoring and assessment of the linear heat transfer coefficient .....	116
Annexe VI –Thermal response test .....	118

## LISTE DES TABLEAUX

<b>Table 1.1 :</b> Analytically and numerically solved thermal properties values and calculated correction factors of O-TRTs for the OS sand. ....	28
<b>Table 1.2:</b> Analytically and numerically solved thermal properties values of O-TRTs for the WK sand..	30
<b>Table 2.1:</b> Parameters values to perform the sensitivity analysis. ....	41
<b>Table 2.2:</b> Sensitivity of input parameters on averaged COP. The parameters used in the best case scenario are highlighted in green or stay unchanged from the base case scenario if a variation of the parameter's value does not induce a COP gain. Parameters used in the worst case scenario are highlighted in red.....	43
<b>Table 3.1 :</b> Hydraulic and thermal properties assigned to the numerical models. ....	63
<b>Table II.1 :</b> Results from the O-TRT analysis for the OS. ....	103
<b>Table II.2:</b> Results from the O-TRT analysis for the WK.....	103
<b>Table II.3:</b> Correction factors calculated for O TRTs performed in the OS. ....	104
<b>Table II.4:</b> Results from the O-TRT numerical simulations for the OS.....	105
<b>Table II.5:</b> Results from the O-TRT numerical simulations for the WK. ....	105

## LISTE DES FIGURES

<b>Fig.1:</b> Diagramme conceptuel des différents chapitres inclus dans le mémoire de maîtrise.....	7
<b>Fig.1.1 :</b> Minimal oscillatory periods required to perform an O-TRT according to the minimal $r_p=0.1$ Eskilson's criterion [18]. Values of $t_0$ are plotted against an arbitrary range of $\alpha_{gr}$ values varying from 0.1 to $1.5 \text{ mm}^2 \text{ s}^{-1}$ on a $\log_{10} - \log_{10}$ scale.....	15
<b>Fig.1.2:</b> Steps for temperature data analysis of an O-TRT after Giordano (2021): (a) inferred $T_0$ and $\Delta T$ calculation for the evaluation of $\lambda$ with the slope method (steps 1 and 2); (b) processing to extract the oscillatory thermal response (step 3); (c) oscillatory thermal response parameters implied in Eq (3) (step 4); (d) curve fitting method to calculate $\phi$ for the $\alpha$ assessment (step 4).1.2.2 Measurement setup.....	19
<b>Fig.1.3:</b> Diagram of an oscillatory thermal response test with a buried heating cable in a trench.....	20
<b>Fig.1.4 :</b> Specifications of DST centi-T (Star Oddi) and Nautical Lite (Alpha Mach) sensors and temperature measurements for O-TRT with period of oscillation $t_0 = 4 \text{ h}$ , power amplitude $Q_{Amp} \approx 4 \text{ W m}^{-1}$ , phase shift difference $\Delta\phi_{(1)-(2)} = 0.031 \text{ rad}$ , and oscillatory thermal resistance $R_{osc(1)-(2)} = 0.173 \text{ }^\circ\text{C}$ .....	20
<b>Fig.1.5:</b> Temperature and power data recovered from the O-TRTs performed in the OS at laboratory conditions and view of the wooden box (A) half filled with the OS with temperature sensors attached to the heating cable and; (B) fully filled with the OS.....	21
<b>Fig.1.6:</b> Temperature and power data obtained from the O-TRTs performed at the study site in Whapmagoostui-Kuujjuarapik and (A) general view of the trench and excavated material at the study site in Whapmagoostui-Kuujjuarapik and; (B) close-up of the heating cable and temperature sensors installed at the bottom of the trench.....	22
<b>Fig.1.7:</b> Three-dimensional mesh and boundary conditions for the numerical model developed for the OS case.....	26
<b>Fig.1.8:</b> Three-dimensional mesh and boundary conditions for the numerical model of the WK case.....	27
<b>Fig.1.9:</b> a) Simulated temperature (black line) representative of the optimized thermal properties (orange star in subfigures b and c) obtained by minimizing the RMSE calculated with temperature data of sensors D1 (orange circle), D2 (blue triangle), D3 (red diamond) and D4 (green square) for the O-TRT-1. RMSE interpolation trend function of b) $\lambda$ , and c) $\alpha$ according to the simulated scenarios for the O-TRT-1.....	28
<b>Fig.1.10:</b> a) Simulated temperature (black line) representative of the optimized thermal properties (orange star in subfigures b and c) obtained by minimizing the RMSE calculated with temperature data of sensors D2 (blue triangle), D3 (red diamond) and D4 (green square) for the O-TRT-14. RMSE interpolation trend function of b) $\lambda$ , and c) $\rho C$ according to the simulated scenarios for the O-TRT-14.....	30
<b>Fig.1.11:</b> Comparison between analytical and numerical solutions of the phase shift parameter averaged for each O-TRTs in OS (left figure) and WK (right figure).....	32

<b>Fig.2.1 :</b> a) Mesh construction and BC applied to BTES numerical model; b) energy yearly profile of the BTES where power extracted from the ground is the blue area, power injected into the ground is the red area and power from the heat load or the heat injection profiles not involved into BTES models is the grey area.....	40
<b>Fig.2.2:</b> Base case scenario's simulated temperature and COP .....	43
<b>Fig.3.1:</b> Location of data and infrastructures in Whapmagoostui-Kuujjuarapik and at the CEN research station.....	53
<b>Fig.3.2:</b> Yearly averaged temperature, rain, or snow precipitations from 2012 and 2013 measured by the Kuujjuarapik no.7103536 meteorological station of Environment Canada (2021).....	54
<b>Fig.3.3:</b> Simplified conceptual model of a typical building with a heat pump coupled to a) a BHE b) a BTES <sub>sand</sub> c) and BTES <sub>bedrock</sub> . Conceptual models represented are not to scale.....	58
<b>Fig.3.4:</b> GHE a) internal configuration, and interconnections for b) a BHE split in two parallel arrays and c) a BTES during heat injection/extraction split in two parallel arrays. GHE proportions are exaggerated in b and c .....	60
<b>Fig.3.5:</b> Thermal properties variations used during a year to represent groundwater recharge periods in numerical models for the silty sand material.....	65
<b>Fig.3.6:</b> Yearly energy profile of heat extraction/injection scenarios for a) BHE and b) BTES models providing heat to one building where $P_{HD1}$ (blue line) represents 80% of the total heating demand provided by a heat pump, $P_{HD2}$ (blue line) represents 20% of the total heating demand provided by a backup diesel furnace, $P_{EPV}$ (green lines) represents the PV electricity production available according to different solar panels area and $P_{HPV}$ (red line) represents the thermal energy injected to the ground for BTES numerical models. By convention, energy models' inflows are considered negative.....	68
<b>Fig.3.7:</b> Hydraulic gradient variations used during a year to represent groundwater recharge periods in numerical models. ....	69
<b>Fig.3.8:</b> Discretized numerical models for the a) BHE case and b) BTES cases.....	71
<b>Fig.3.9:</b> Initial temperature profile obtained after a two-year simulation for the a) BHE, b) BTES installed in silty sand and c) BTES installed in bedrock numerical models. ....	72
<b>Fig.3.10:</b> Simulated scenarios.....	73
<b>Fig.3.11:</b> Scheme of the energy consumption and costs calculations for the numerical models. ....	74
<b>Fig.3.12:</b> Temperature profiles at the center of the numerical models during midwinter after 6,980 days of operation (blue lines) and midsummer after 7,160 days of operation (red lines) for BHE (a, b), BTES <sub>sand</sub> (c, d) and BTES <sub>bedrock</sub> (e, f) scenarios. ....	75
<b>Fig.3.13:</b> Ground temperature in fall after 7,200 days of operation (20 days under a groundwater recharge period with $\nabla h = 0.0175 \text{ m m}^{-1}$ ) for the BHE (a), BTES <sub>sand</sub> (b) and BTES <sub>bedrock</sub> (c) scenarios.....	77

<b>Fig.3.14:</b> Simulated temperature at the ground source heat pump inlet for the scenarios providing the heating demand of a) one building and b) two buildings.....	78
<b>Fig.3.15:</b> PV area used vs. electricity needs covered by the PV area and average $P_{TP}$ consumed by the heating systems simulated for one (a, c) and two (b, d) buildings. ....	79
<b>Fig.3.16:</b> CO <sub>2</sub> emissions, $Cost_{HSYS}^{customer}$ and $Cost_{HSYS}^{societal}$ of the simulated scenarios providing the heating demand of one (a,c,e) and two residential buildings (b,d,f). .....	81
<b>Fig.3.17:</b> $Cost_{HSYS}^{customer}$ vs. CO <sub>2</sub> emissions a) and $Cost_{HSYS}^{societal}$ vs. CO <sub>2</sub> emissions b) of the simulated scenarios. Each scenario has eight symbols representing the electrical assistance of a PV area where a line gets thicker from the smallest area of 0 m <sup>2</sup> (smaller symbols) towards the largest area of 336 m <sup>2</sup> (bigger symbols) with constant steps of 48 m <sup>2</sup> . ....	82
<b>Fig.I.1:</b> Temperature and power data recovered from the C-TRTs performed in the OS (left figures) and WK (right figures). ....	100
<b>Fig.I.2:</b> RMSE calculated at different distance from the heating cable in the OS C-TRT and optimized values.....	101
<b>Fig.I.3:</b> RMSE calculated at different distance from the heating cable in the WK sand C-TRT and optimized values.....	102
<b>Fig.III.1:</b> Location of the GPR survey lines at the CEN research station. ....	106
<b>Fig.III.2:</b> Common midpoint and reflection analysis at the CEN research station.....	107
<b>Fig.IV.1:</b> a) 3D view of the mesh showing top and bottom boundary conditions of the regional groundwater numerical model b) x-y top view showing the elevation, lateral and top boundary conditions of the regional groundwater numerical model.....	110
<b>Fig.IV.2:</b> Material properties of the regional groundwater numerical model.....	110
<b>Fig.IV.3:</b> Calibrated material properties of the regional groundwater numerical model.....	111
<b>Fig.IV.4:</b> Hydraulic head simulated without the influence of the P1 and P2 pumping wells for the regional numerical model.....	112
<b>Fig.IV.5:</b> Hydraulic head simulated with the influence of the P1 and P2 pumping wells for the regional numerical model.....	112
<b>Fig.IV.6:</b> Drawdown simulated at the end of the 72-h pumping test for the regional numerical model. .	113
<b>Fig.IV.7:</b> Hydraulic head observed vs. simulated of the calibrated regional numerical model.....	113
<b>Fig.IV.8:</b> Comparison of hydraulic conductivity measurements with the Guelph permeameter method, the numerically calibrated method, and the literature range of values for silt and sand (Freeze and Cherry, 1979). .....	114
<b>Fig.V.1:</b> Temperature reference used to represent air temperature at top of the numerical models. ....	116

<b>Fig.V.2:</b> Comparison of the solved temperature with a linear heat transfer coefficient of $20 \text{ W m}^{-2} \text{ }^{\circ}\text{C}^{-1}$ at a) 0.5 and 0.7 m where temperature was measured in 2018 to 2019, and b) 1.0 and 2.0 m where temperature was measured in 2019 to 2020.....	117
<b>Fig.VI.1:</b> Layout diagram of the constant thermal response test in the TF05-12 observation well.....	119
<b>Fig.VI.2:</b> Summary of the constant thermal response test showing a) calculated heat injection rate data, b) measured temperature data and c) calculated thermal conductivity for temperature sensors #1 to #16. ..	120

## NOMENCLATURE

$A$	génération interne de chaleur	[W m <sup>-3</sup> ]
$C$	chaleur spécifique	[kJ kg <sup>-1</sup> K <sup>-1</sup> ]
$Cal$	facteur de calibration	[ $\cdot$ ]
$Co$	nombre de Courant	[ $\cdot$ ]
$D$	diesel	[ $\cdot$ ]
$F$	facteur de correction	[ $\cdot$ ]
$h$	charge hydraulique	[m]
$K$	conductivité hydraulique	[m s <sup>-1</sup> ]
$l$	coefficient de transfert de chaleur	[W m <sup>-2</sup> K <sup>-1</sup> ]
$L$	longueur	[m]
$m$	pente utilisée pour l'analyse de la conductivité thermique	[°C]
$\dot{m}$	débit	[m <sup>3</sup> s <sup>-1</sup> ]
$P$	puissance	[W]
$Pe$	nombre de Peclet	[ $\cdot$ ]
$q$	vitesse de Darcy	[m s <sup>-1</sup> ]
$r$	rayon	[m]
$R$	résistance thermique linéaire	[m K W <sup>-1</sup> ]
$rp$	critère d'Eskilson	[ $\cdot$ ]
$S$	emmagasinement spécifique	[m <sup>-1</sup> ]
$t$	temps	[s]
$T$	température	[°C]
$\bar{T}$	température moyenne	[°C]
$v$	vitesse	[m s <sup>-1</sup> ]
$W$	flux entrant/sortant d'énergie	[W]
$X$	distance entre deux nœuds du maillage numérique	[m]

### Symbols grecs

$\alpha$	diffusivité thermique	[mm <sup>2</sup> s <sup>-1</sup> ]
$\Delta$	différence	[ $\cdot$ ]
$\partial$	dérivée partielle	[ $\cdot$ ]
$\kappa$	dispersion mécanique	[m]
$\nabla$	gradient	[m <sup>-1</sup> ]
$\delta$	erreur relative (incertitude) de l'estimation	[%]
$\gamma$	constante Euler-Mascheroni, 0.5772156649...	[ $\cdot$ ]

$\lambda$	conductivité thermique [W m <sup>-1</sup> K <sup>-1</sup> ]
$\phi$	déphasage [radian]
$\rho$	masse volumique [kg m <sup>-3</sup> ]
$\sigma$	écart type [-]
$\theta$	porosité[-]

### Indices et abréviations

acc	exactitude
Amp	amplitude
bh	puits
BHE	puits à boucle fermée vertical
BTES	système d'emmagasinement thermique souterrain avec puits à boucle fermée vertical
cbl	câble chauffant
COP	coefficient de performance
eff	effective
EPV	électricité produite par des panneaux solaires photovoltaïques
eq	équivalent
f	fluide
GHE	échangeur de chaleur dans le sol
gr	sol
HCF	fluide caloporpateur
HD	demande en chauffage
HPV	chaleur produite dérivée de panneaux solaires photovoltaïques
HSYS	système de chauffage
LO	longitudinal
ref	référence
s	solide
TP	centrale thermique
TR	transverse

# **I. Synthèse**

## 1. Introduction

Les communautés nordiques du Nunavik utilisent majoritairement le diesel pour alimenter les bâtiments en électricité et en chauffage comme elles ne sont pas branchées au réseau hydroélectrique de la province de Québec. Ces communautés sont localisées dans un climat subarctique à arctique où les bâtiments doivent être chauffés presque toute l'année en raison d'une région caractérisée par plus de 8000 degrés-jours de chauffage sous une température limite de 18 °C (HDD<sub>18</sub>; Atlas climatique du Canada, 2019). En se référant à la consommation totale de combustibles fossiles des communautés nordiques du Canada, le chauffage des bâtiments consomme trois fois plus de combustibles fossiles que la production d'électricité par les centrales thermiques (Senate of Canada, 2014). Cette situation expose le besoin évident de diminuer la consommation de mazout liée au chauffage à l'aide d'énergies renouvelables tel que les systèmes géothermiques. L'énergie issue du sous-sol (ou géothermique) peut être exploitée à l'aide de pompes à chaleur géothermique couplées à un échangeur de chaleur installé dans le sol (GHE) et permet d'effectuer des économies substantielles en chauffage. Les systèmes géothermiques peuvent fournir en continu le chauffage des bâtiments en consommant peu d'énergie, en offrant une bonne fiabilité et de faibles coûts de maintenance (Kavanaugh et Rafferty, 2014; Belzile et al., 2017; Gunawan et al., 2020). Différentes configurations de GHE sont disponibles et certaines d'entre elles ont plus de potentiel que d'autres pour le contexte nordique.

Les GHE à boucle fermée peuvent être disposés horizontalement dans des tranchées ou verticalement dans des puits géothermiques (BHE). Les GHE horizontaux sont habituellement installés à environ 2 m de profondeur. Ils nécessitent une grande surface de terrain pour les installer en raison de la faible température du sol et des faibles valeurs de propriétés thermiques. Belzile (2017) a simulé un GHE horizontal d'une longueur de 165 à 260 m disposé en « slinky ». Cette longueur dépendait de la plage de valeurs de la conductivité thermique du sol attendu pour fournir en chaleur une résidence construite après la complétion de leur étude à Kangiqsualujjuaq (Québec). Ils ont aussi recommandé d'utiliser une pompe à chaleur fabriquée sur mesure puisque la température du fluide caloporteur à l'entrée de la pompe à chaleur diminuait à -10 °C, alors que les pompes à chaleur disponibles sur le marché arrêtent généralement de fonctionner à -6.7 °C (Geosmart Energy, 2013; Robur, 2014).

L'épaisseur des dépôts meubles dans le Nunavik est variable d'un endroit à un autre et il n'est pas toujours possible d'installer les GHE horizontaux aux profondeurs voulues. Malgré leurs coûts d'installation plus élevés que les GHE horizontaux, principalement en raison du coût lié au forage, les BHE peuvent être installées partout que ce soit dans le roc comme dans les dépôts meubles. Le guide de l'ASHRAE (Kavanaugh et Rafferty, 2014) fournit d'ailleurs une procédure pour dimensionner ces BHE. Cependant, cette procédure a majoritairement été expérimentée au centre des États-Unis et non dans un climat nordique

où il y a des défis considérables de conception. En résumé, les GHE horizontaux et BHE sont tous les deux intéressants pour le contexte nordique. Cependant, ce travail se concentre sur les BHE puisqu'ils sont plus facilement implémentables sur tout le territoire du Nunavik alors que l'implémentation de GHE horizontaux implique plusieurs contraintes.

Les BHE sont conventionnellement installés dans la partie peu profonde du sol (< 150 m selon la demande en chauffage) afin de forer au moins d'endroits possibles. Si la demande en chauffage du bâtiment est trop grande pour un seul BHE d'une longueur de 150 m, d'autres BHE sont forés et connectés à la pompe à chaleur pour fournir la chaleur au bâtiment. Les BHE sont alors disposés de façon qu'il n'y ait pas d'interaction thermique entre eux afin de ne pas diminuer les performances de la pompe à chaleur. Les systèmes de stockage thermique souterrain avec échangeurs de chaleur verticaux (BTES) reposent quant à eux sur l'opération de plusieurs GHE disposés de façon à avoir une interaction thermique optimisée pour injecter des surplus énergétiques dans le sol (produits avec d'autres énergies renouvelables) et de les récupérer lors de la période hivernale lorsque la demande en chauffage est maximale (Hellström, 1991). Les BTES présentent un fort potentiel pour les communautés nordiques puisque ce système permet de chauffer le sol de façon dynamique et d'assurer l'efficacité et le fonctionnement des pompes à chaleur. De plus, cette technologie est indépendante des conditions météorologiques et permet de maximiser l'utilisation d'énergies renouvelables intermittentes telles que l'énergie solaire. En effet, au nord du 55<sup>e</sup> parallèle, le soleil est visible pendant plus de 17 h par jour en période estivale, tandis que l'exposition au soleil est inférieure à 8 h par jour en hiver. Les panneaux solaires photovoltaïques (PV) produisent des surplus énergétiques en été, contrairement en hiver lorsque la demande en chauffage est maximale et que la réduction de la consommation en mazout est désirée. Les BTES optimisent l'utilisation des PV en emmagasinant ces surplus énergétiques en été et en les récupérant en hiver lorsqu'il y a une demande énergétique de pointe en chauffage du bâtiment. Giordano et Raymond (2019) ont simulé le fonctionnement d'un BTES de grande dimension sans pompe à chaleur et couplé à un champ de panneaux solaires thermiques sur une période de 5 années pour étudier l'efficacité du BTES dans le climat subarctique de Kuujjuaq (Québec). Ils ont estimé que ce système peut réaliser, dès la 3<sup>ième</sup> année d'exploitation, des économies annuelles de 13%, soit de 7 000 L de mazout consommés pour le chauffage de l'eau potable dans une station de pompage.

Les GHE sont couplés à des pompes à chaleur pour accroître l'énergie thermique du sol et fournir la demande en chauffage d'un bâtiment. L'utilisation d'une pompe à chaleur est pertinente puisque la température du sol au Nunavik est très basse et cette technologie permet de transférer l'énergie thermique du sol à un bâtiment tout en réalisant des économies de consommation d'énergie. Les pompes à chaleur à compression (COMP) sont communément utilisées, car elles offrent des économies d'énergie importantes

en raison d'un coefficient de performance (COP) élevé. Garber-Slaght et Peterson (2017) ont étudié des installations à Fairbanks (Alaska) couplant une COMP et un GHE horizontal et ils ont calculé un COP de 3.7 la première année d'exploitation. Cependant, l'électricité dans les communautés nordiques est produite par des centrales thermiques ayant une efficacité entre 31 et 35% (Deslauriers, 2008). Cette situation diminue le potentiel d'économiser du mazout et il est important de comparer les COMP à d'autres types de pompe à chaleur utilisant peu d'électricité. Les pompes à chaleur à absorption (ABS) consomment significativement moins d'électricité qu'une COMP. Elles peuvent réduire la consommation en énergies fossiles lié au chauffage puisqu'elles utilisent un compresseur thermique alimenté par des énergies fossiles dont le fonctionnement est programmé par un système électronique à faible ampérage. Belzile (2017) a estimé que les économies d'énergie sont plus élevées avec une ABS faite sur mesure ayant un COP  $\approx$  1.2 qu'avec une COMP. Ceci est en majorité causée par une consommation trop importante d'électricité, produite de façon inefficace, par la COMP dans un contexte où l'électricité produite par des PV n'est pas considérée comme source d'alimentation. Par contre, Gunawan (2020) a comparé les résultats de simulations d'un BHE couplé à une COMP et d'une ABS alimentées par de l'électricité produite par des PV et ils ont conclu que la COMP a un potentiel d'économie énergétique et monétaire plus élevé qu'une ABS. Par conséquent, la consommation totale de mazout et d'électricité pour l'alimentation des COMP et ABS doit être évaluée en raison des contextes climatique et énergétique particuliers du Nunavik.

La consommation énergétique d'une pompe à chaleur dépend aussi des interactions thermiques entre les GHE et le sol dans lesquels ils sont installés. Selon le contexte hydrogéologique et le type de GHE, l'écoulement d'eau souterraine peut fournir ou dissiper de l'énergie thermique et ainsi affecter les performances de la pompe à chaleur (Gehlin, 2002; Catolico, Ge et McCartney, 2015). Les incertitudes liées au contexte thermo-géologique exercent également une influence considérable sur l'efficacité du système et il est recommandé d'évaluer de façon *in situ* les propriétés du sol (Casasso et Sethi, 2014). La conductivité thermique ( $\lambda$ ) et la diffusivité thermique ( $\alpha$ ) *in situ* sont des paramètres critiques pour évaluer la performance des systèmes géothermiques. La  $\lambda$  est conventionnellement déterminée avec des essais de réponse thermique, alors que la  $\alpha$  est communément sélectionnée à partir de données de littérature ou des analyses en laboratoire impliquant des incertitudes importantes. Une alternative à ces méthodes est d'utiliser un essai de réponse thermique oscillatoire (O-TRT) afin de déterminer la  $\lambda$  et la  $\alpha$  indépendamment. Des études récentes (Oberdorfer, 2014; Giordano et al. 2021) ont permis de réaliser et d'analyser des O-TRT en circulant un fluide réchauffé dans des BHE. Cependant, la durée des essais qu'ils ont réalisés devait être élevée ( $> 7$  jours) afin de minimiser l'effet de la résistance thermique des forages sur le calcul de la  $\alpha$ . Cette méthode peut être adaptée en utilisant des câbles chauffants ayant une faible résistance thermique pour les placer en contact direct avec le sol afin de diminuer la durée des essais. Cette procédure a un potentiel

intéressant comme l'appareillage nécessaire demeure peu coûteux, facile d'utilisation et permet d'éviter l'effet composite du BHE.

À ce jour, peu d'études ont évalué la viabilité de systèmes géothermiques dans un contexte similaire à celui du Nunavik (Belzile et al., 2017; Garber-Slaght et Peterson, 2017; Giordano et Raymond, 2019; Gunawan et al., 2020). Parmi ces études, aucune d'entre elles comparent la consommation d'énergie et l'efficacité de différents systèmes géothermiques. Elles se concentrent plutôt sur l'évaluation de la faisabilité technique ou économique d'un GHE horizontal (Belzile et al., 2017; Garber-Slaght and Peterson, 2017), d'un BHE (Gunawan et al., 2020) et d'un BTES (Giordano et Raymond, 2019) sur leur site à l'étude respectif. Les données et les méthodes utilisées dans ces études peuvent être bonifiées avec des données in situ, des observations de terrain et une modélisation numérique avancée impliquant les phénomènes de gel et dégel du sol pour réduire les incertitudes liées à l'efficacité des systèmes géothermiques en climat subarctique. La comparaison de différents types de GHE sur un même site offre aussi une meilleure idée de leur efficacité et de leurs limites puisque des défis de conception sont anticipés dans chaque cas. La température du sol en climat subarctique à arctique est près du point de congélation de l'eau et la demande en chauffage est importante en raison des conditions météorologiques extrêmes, du taux d'occupation des bâtiments et des particularités associées aux bâtiments nordiques (Gouvernement du Québec, 2020). De ce fait, la demande énergétique est débalancée au cours d'une année et une extraction de chaleur du sol excessive peut induire des changements de phase de l'eau dans les pores du sol (Dalla Santa et al., 2019). Garber-Slaght et Peterson (2017) ont estimé que le COP de leur pompe à chaleur a diminué de 14% en seulement trois années d'exploitation du système géothermique en raison de la formation de glace autour des GHE. Ils ont également suggéré qu'une recharge thermique du sol sous 1 m de profondeur, tel l'exploitation d'un BTES, est nécessaire pour répondre à la demande énergétique débalancée du bâtiment. Dans de tels contextes, la modélisation numérique est une méthode intéressante pour simuler à la fois l'effet de la chaleur sensible et latente du sol en tenant compte des proportions d'eau à l'état liquide et solide dans les pores du sol et de son influence sur l'écoulement de l'eau souterraine (Kane et al., 2001; McKenzie, Voss et Siegel, 2007; Anbergen et al., 2015).

La station de recherche du Centre d'études nordiques (CEN) à Whapmagoostui-Kuujjuarapik (longitude -77.7470°, latitude 55.2765°, élévation 19 m) est localisée au sud du territoire du Nunavik. Ces communautés totalisant 1400 habitants ont été choisies comme site d'étude pour évaluer la performance de systèmes géothermiques dans un contexte de communauté nordique. Ce village est caractérisé par un climat subarctique avec la présence de pergélisol discontinu et 7 700 HDD<sub>18</sub>. Le CEN a une station de recherche ouverte toute l'année depuis 1971. Un grand nombre de données est disponible, en plus d'une accessibilité

aux installations, ce qui est utile pour enregistrer les paramètres importants pour une étude approfondie comparant différents types de systèmes géothermiques.

## 2. Définition du problème

Bien que les travaux précédents (Belzile et al., 2017; Garber-Slaght et Peterson, 2017; Kanzari 2019; Giordano et Raymond, 2019; Gunawan et al., 2020) aient permis de dresser le potentiel des systèmes géothermiques au Nunavik, de nombreux questionnements concernant leur implantation demeurent. En effet, ces études se sont concentrées sur l'évaluation d'un type de GHE en particulier alors qu'ils ont tous des avantages et inconvénients méritant d'être comparés entre eux. De plus, ces études ont analysé l'opération de systèmes géothermiques en supposant des simplifications importantes pour simuler les processus de transfert thermique dans le sous-sol. La simplification de certains de ces phénomènes dont la chaleur latente peut affecter la performance des systèmes géothermiques et il est impératif d'évaluer leur impact en climat nordique.

Les BTES ont un fort potentiel pour le contexte nordique, mais cette technologie a seulement été étudiée au Nunavik dans un contexte pour chauffer de l'eau potable alors qu'il y a plusieurs autres applications possibles tel que le chauffage de bâtiments. Les travaux réalisés par Giordano et Raymond (2019) supposaient le déploiement d'un BTES et d'un champ de PV très volumineux présentant une application spécifique n'utilisant pas de pompe à chaleur. Un BTES de plus faible volume avec une application répandue, tel le chauffage d'un bâtiment, est un exemple plus reproductible pour ces communautés et peut favoriser un déploiement rapide de cette technologie. Afin de donner une meilleure idée de son potentiel, il est pertinent de comparer le BTES à une technologie conventionnelle comme un BHE pour différencier leur application respective au sein du territoire du Nunavik. Comme ces deux types de GHE ont des interactions thermiques différentes avec le sol, il est nécessaire de faire une analyse comparative approfondie des systèmes en fonction du sol. À ce jour, le couplage entre un BTES et une pompe à chaleur n'a jamais été étudié au Nunavik alors que cette méthode est pertinente pour une région nordique où la température du sol est près du point de congélation de l'eau. De plus, les études précédentes se sont basées sur des simplifications importantes pour simuler l'interaction entre les GHE affectant la performance des GCHP. Il est donc nécessaire d'étudier l'interaction entre le sol et chaque type de GHE couplé à une COMP et une ABS pour avancer l'état des connaissances dans le contexte nordique qui est complexe.

Pour estimer adéquatement la performance des systèmes, les essais de réponse thermique *in situ* doivent être priorisés afin de minimiser les incertitudes liées aux calculs. Les seuls essais effectués dans le domaine permettent d'estimer la  $\lambda$  alors que la  $\alpha$  demeure un paramètre important pour estimer la

performance des BTES. L'utilisation de câbles chauffants pour réaliser un O-TRT est une méthode prometteuse afin d'estimer  $\lambda$  et  $\alpha$  au cours du même essai. Cependant, cette méthode n'a pas été appliquée auparavant et il apparaît nécessaire de la valider.

Ce travail se divise en deux parties. La première partie (Chapitre 1) cherche à développer et valider la méthode de l'O-TRT en tranchée pour estimer de façon in situ la  $\lambda$  et la  $\alpha$ . Pour ce faire, la méthode a été expérimentée dans deux matériaux granulaires différents : un matériel granulaire de référence (sable d'Ottawa C-109) pour valider la méthode dans un matériel où les valeurs de la  $\lambda$  et  $\alpha$  sont connues; et un dépôt sableux situé à la station du CEN pour valider la méthode sur le terrain. La deuxième partie se concentre sur l'estimation de la performance des systèmes géothermiques en contexte nordique. Des modèles numériques ont été développés pour simuler l'opération des pompes à chaleur et estimer leur économie d'énergie en fonction du contexte géologique de la station de recherche du CEN. Afin de mieux définir l'efficacité d'un BTES en région nordique, une deuxième étude (Chapitre 2) vise à évaluer l'influence des paramètres impliqués dans l'opération d'un BTES sur l'efficacité énergétique du système. Finalement, une troisième étude (Chapitre 3) compare l'interaction et la viabilité d'un BHE et d'un BTES couplés à une COMP et à une ABS.

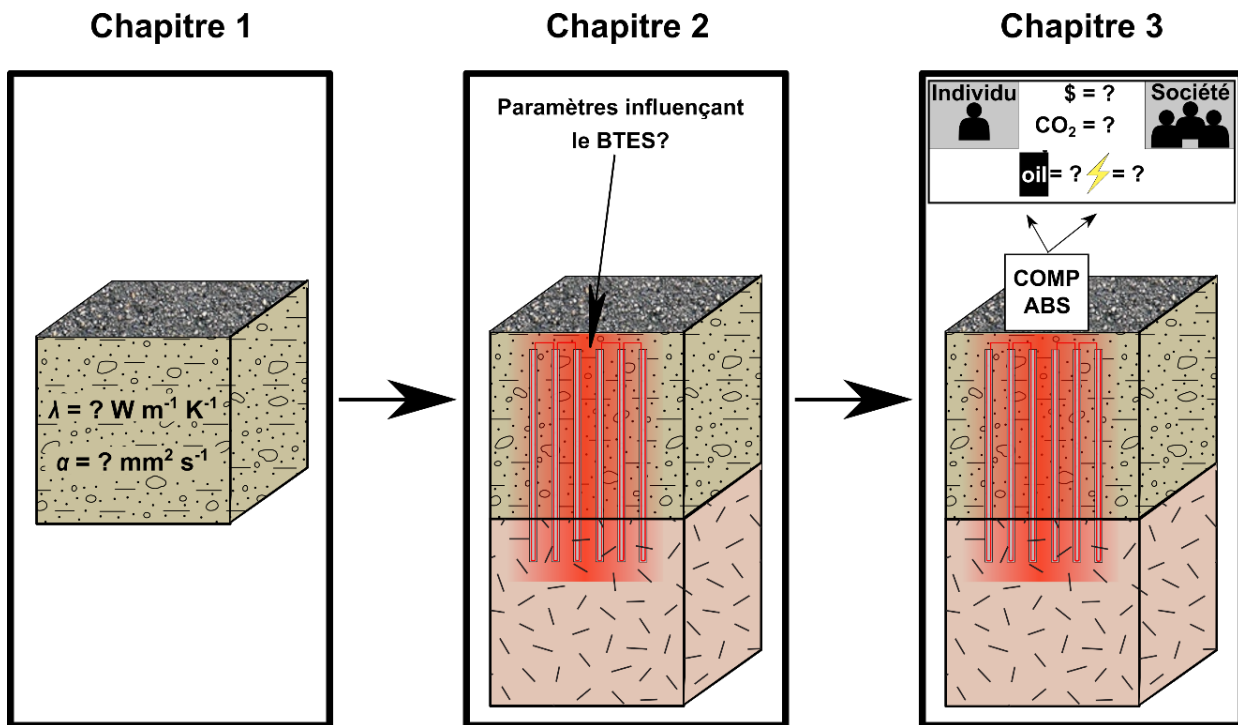


**Fig.1:** Diagramme conceptuel des différents chapitres inclus dans le mémoire de maîtrise.

### **3. Objectifs**

Ce projet de maîtrise vise à évaluer, en fonction d'une étude approfondie du sous-sol, le potentiel de différents GHE couplées avec des pompes à chaleur pour répondre aux besoins énergétiques de bâtiments en région nordique. Pour réaliser ces évaluations, divers objectifs spécifiques ont été fixés :

1. Développer une méthode pour réaliser des essais afin d'estimer de façon in situ la  $\lambda$  et la  $\alpha$  des dépôts meubles du sol ;
2. Comprendre les phénomènes majeurs impliqués dans l'exploitation de systèmes géothermiques interagissant entre les GHE en climat subarctique ;
3. Comparer le potentiel de pompes à chaleur couplées à un BHE et à un BTES en climat nordique.

### **4. Approche méthodologique**

Afin de réaliser ces objectifs, il est nécessaire d'élaborer une méthodologie appropriée. Celle-ci a été définie comme suit :

1. Développer une méthode pour réaliser des essais afin d'estimer de façon in situ la  $\lambda$  et la  $\alpha$  des dépôts meubles du sol:
  - Déploiement de l'appareillage en laboratoire avec un matériel standardisé et en tranchée en contact direct avec des dépôts meubles.
  - Développement d'une approche analytique de l'O-TRT avec câble chauffant.
  - Validation de l'approche analytique avec une approche numérique.
2. Comprendre les phénomènes majeurs impliqués dans l'exploitation de systèmes géothermiques interagissant entre les GHE en climat subarctique:
  - Développement de modèles numériques pour simuler l'opération d'un BTES.
  - Réaliser une analyse de sensibilité sur tous les paramètres d'entrée considérés pour les simulations.
  - Comparer le COP de la pompe à chaleur simulée pour quantifier l'analyse de sensibilité.
3. Comparer l'efficacité de pompes à chaleur couplées à un BHE et à un BTES en climat nordique:
  - Développement de modèles numériques pour simuler l'opération de BHE et de BTES couplés à des COMP et ABS.
  - Évaluer la consommation d'énergie pour chaque modèle numérique selon une quantité de PV disponible.
  - Comparer la perturbation thermique du sol, l'efficacité de la pompe à chaleur, la consommation énergétique et les coûts énergétiques selon les résultats de simulation numérique.



## **II. Articles**

# Chapitre 1

## Oscillatory thermal response tests using heating cables: A novel method for in situ thermal property analysis

### **Titre traduit**

Utilisation de câbles chauffant dans des essais de réponse thermique oscillatoires : Une méthode novatrice pour l'analyse de propriétés thermiques in situ

### **Auteurs**

Hubert Langevin<sup>1,2</sup>, Nicolò Giordano<sup>2</sup>, Jasmin Raymond<sup>1</sup>, Louis Gosselin<sup>3</sup>

<sup>1</sup>Institut national de la recherche scientifique, Centre Eau-Terre-Environnement, 490 rue de la Couronne, Quebec City, QC, G1K9A9, Canada

<sup>2</sup>Géotherma solutions Inc., 490 rue de la Couronne, Office 4332, Quebec City, QC, G1K9A9, Canada

<sup>3</sup>Université Laval, Mechanical Engineering Department, 1065 avenue de la Médecine, Québec, QC, G1V0A6, Canada

### **Soumis**

*International Journal of Heat and Mass Transfer*

### **Mots-clés**

conductivité thermique; diffusivité thermique; test de réponse thermique oscillatoire; câble chauffant

### **Keywords**

thermal conductivity; thermal diffusivity; oscillatory thermal response test; heating cable

## Résumé

La conductivité thermique ( $\lambda$ ) et la diffusivité thermique ( $\alpha$ ) in situ sont des paramètres critiques pour le dimensionnement des systèmes géothermiques. La  $\lambda$  est conventionnellement déterminée avec des essais de réponse thermique (TRT), alors que la  $\alpha$  est communément sélectionnée à partir des données de littérature ou d'analyses en laboratoire. Alternative, chacune de propriétés peuvent être estimées indépendamment avec un essai de réponse thermique oscillatoire (O-TRT) qui consiste à chauffer le sol à un taux de chaleur oscillatoire et à enregistrer la perturbation thermique résultante. En raison de leur flexibilité et de leur volume relativement faible, les câbles chauffants peuvent être utilisés pour effectuer des essais dans des dépôts sédimentaires non consolidés et peu profonds dans le cadre d'un dimensionnement d'un système géothermique intégrant un échangeur de chaleur horizontal. La durée des tests est faible par rapport à un échangeur de chaleur vertical (fractions de jour), car la résistance thermique des matériaux du câble chauffant est presque nulle. L'objectif de ce travail était de développer un appareillage et une approche analytique utilisant des facteurs de correction pour évaluer  $\lambda$  et  $\alpha$  à partir d'O-TRT réalisés dans des dépôts meubles. Neuf O-TRT différents ont été réalisés en laboratoire pour un matériau standardisé en condition sèche et cinq O-TRT ont été réalisés en condition in situ dans un dépôt sableux naturel. Après validation par modélisation numérique, les résultats montrent que l'approche analytique utilisant des facteurs de correction a permis d'estimer  $\lambda$  et  $\alpha$  avec une précision < 2%. Cette étude démontre que l'O-TRT est une méthode utile pour estimer à la fois  $\lambda$  et  $\alpha$ . Des essais supplémentaires dans d'autres matériaux de référence et avec différentes configurations d'appareils sont nécessaires pour améliorer la configuration expérimentale et étendre l'O-TRT vers de nouvelles applications.

## Abstract

In situ subsurface thermal conductivity ( $\lambda$ ) and thermal diffusivity ( $\alpha$ ) are critical parameters to design ground-coupled heat pump systems (GCHP).  $\lambda$  is conventionally determined from thermal response tests (TRT), whereas  $\alpha$  is commonly selected from literature data or with laboratory analyses. Alternatively, both thermal properties can be assessed independently with an oscillatory thermal response test (O-TRT), which consists of heating the subsurface at an oscillatory rate and monitor the resulting thermal perturbation. Due to their flexibility and relatively small radius, heating cables can be used to carry out tests in shallow unconsolidated deposits in the scope of horizontal GCHP design. Duration of the tests is small compared to vertical ground heat exchangers (fractions of a day) since the thermal resistance between the heating cable and the soil is negligible. The objective of this work was to develop an apparatus and an analytical approach to assess  $\lambda$  and  $\alpha$  from an O-TRT carried out in shallow unconsolidated deposits. Nine different O-TRTs were performed in the lab for a dry standard material and five O-TRTs were performed in situ in a

natural sandy deposit. After validation via numerical modelling, results show that the analytical approach using correction factors allowed estimating  $\lambda$  and  $\alpha$  with accuracy  $< 2\%$ . The study demonstrates that O-TRTs is a useful method to estimate both  $\lambda$  and  $\alpha$ . Further testing in other reference materials and with different apparatus configurations is needed to enhance the experimental setup and extend O-TRTs towards new applications.

## 1.1 Introduction

Constant heat injection rate thermal response tests (C-TRT) are commonly used to estimate the subsurface heat transfer properties to design ground-coupled heat pumps systems (GCHP) providing heating and cooling to a building. The total length of vertical ground heat exchanger (V-GHE) has to be properly estimated to provide the expected energy savings and meet requirements such as those of the ENERGY STAR program (Environmental Protection Agency, 2021). A C-TRT is typically carried out before designing GCHP with a heat injection rate of  $50\text{--}80 \text{ W m}^{-1}$  by circulating heated water through a GHE for a minimal duration of 36 h (ASHRAE, 2001). Temperature, power, and flow rates are measured during the test to estimate the effective thermal conductivity ( $\lambda$ ) of the subsurface surrounding the GHE. Typically, the infinite line-source (ILS) or cylindrical-source (ICS) analytical solutions describing heat conduction in a homogeneous and isotropic medium are used to reproduce the observed temperature response (Carslaw, 1945; Ingersoll, Zobel et Ingersoll, 1954; Deerman et Kavanaugh, 1991). The borehole thermal resistance  $R_{bh}$  of the GHE can also be estimated with a C-TRT, but a-priori knowledge of the subsurface volumetric heat capacity ( $\rho C$ ), usually chosen from literature values, is required. Electric heating or fiber-optic cables were recently used to perform C-TRT with a low heat injection rate of the order of  $10\text{--}25 \text{ W m}^{-1}$  (Raymond, Lamarche et Malo, 2015; Márquez et al. 2018; Zang et al., 2020). This method requires only 1–2 kW power and is flexible enough to carry out in situ testing in a GHE, an open well or any other type of material providing that there is proper thermal contact with the subsurface. Temperature sensors placed along or inside the heating cable record temperature, which is then analyzed via the conventional slope method (Ingersoll, Zobel et Ingersoll, 1954; Carslaw et Jaeger, 1947) or any other newly developed method (Raymond et al., 2011; Pasquier, 2018; Beier, 2020).

C-TRT analysis with heating cables can provide a subsurface thermal conductivity profile, but  $R_{bh}$  cannot be properly assessed due to the unknown position of the cable in the well. However, even though  $R_{bh}$  can be analyzed with a conventional water-circulation C-TRT, a typical ground  $\rho C$  range of variability of 1.5 to  $3.2 \text{ MJ m}^{-3} \text{ K}^{-1}$  influences the deduced subsurface thermal diffusivity ( $\alpha$ ) by  $\pm 40\%$ , and thus  $R_{bh}$  by  $\pm 10\text{--}23\%$ . As a result, the total drilling length of GHE can be affected by  $\pm 6\text{--}7\%$  as an example for GHE installed in bedrock (Giordano, Lamarche et Raymond, 2021). In unconsolidated sediments,  $\rho C$  range of variability is greater than in rocks due to their high porosity ( $n$ ) and variable water saturation (0.3 to

$3.8 \text{ MJ m}^{-3} \text{ K}^{-1}$ ) (Dalla Santa et al., 2020). Therefore, the required GHE length can be influenced by up to  $\pm 50\%$ . Horizontal ground heat exchanger (H-GHE) and underground thermal energy storage systems (UTES) are likely designed in unconsolidated sediments. H-GHE can experience significant fluctuation of water content (and thus  $\rho C$ ) over an entire season due to precipitations, snow accumulation and melting, and evapotranspiration. It is also important to accurately estimate  $\rho C$  for UTES since it defines the thermal storage dynamics of the subsurface (Skarphagen et al. 2019; Langevin et al. 2021). Laboratory methods are available to estimate this parameter from samples collected in the field to determine ground thermal properties before designing a GCHP and determine the required length of GHE to provide enough heat to a geothermal system. However, their use remains limited due to poor reliability and the difficulty to represent in situ conditions.

An alternative to laboratory analysis is provided by the oscillatory thermal response test method (O-TRT). Recent studies have shown the analysis of the subsurface thermal response of O-TRT with a conventional water-circulation unit (Giordano, Lamarche et Raymond, 2021; Oberdorfer, 2014). Oberdorfer (2014) carried out an O-TRT within 17 days with oscillatory periods  $t_0$  ranging from  $\approx 0.7$  to  $48$  h in a 95-mm-radius GHE. The authors highlighted the potential of the method to acquire more information than conventional C-TRT on both the subsurface and the grouting material. Giordano (2021) have properly assessed the subsurface  $\alpha$  with a 15% uncertainty via a 6-days oscillatory thermal injection in a 57-mm-radius GHE. However, they concluded that the understanding of the oscillatory heat transfer occurring in the composite heat source (heat carrier fluid, plastic, grout) needs to be improved to reduce uncertainty.

In the light of this, the use of a heating cable in direct contact with the subsurface appears to be one of the easiest, adaptable, and low-cost methods to perform an O-TRT. Indeed, it can be used in saturated or unsaturated shallow deposits, thus eliminating the composite effect of the GHE. A heating cable embodies an electrical resistance wrapped in a thin rubber sheath, whose thermal resistance can be overlooked provided that it is directly in contact with the analyzed ground (e.g., laid out in a trench). The radius of the heat source corresponds to the heating cable radius  $r_{\text{cbl}}$ . This allows to have a quicker test according to the criterion proposed by Eskilson (1987). The  $r_{\text{cbl}}$  requires oscillatory period  $t_0$  between 1 to 14 h, compared to 1,050-15,750 h for  $r_{\text{bh}} = 95$  mm, and to 670-10,080 h for a typical  $r_{\text{bh}} = 76$  mm considering the same  $\alpha$  range (Fig.1.1). These two  $r_{\text{bh}}$  values are typical of a borehole that would be used for a TRT since the heat source is the GHE whether heating cables are used or not.

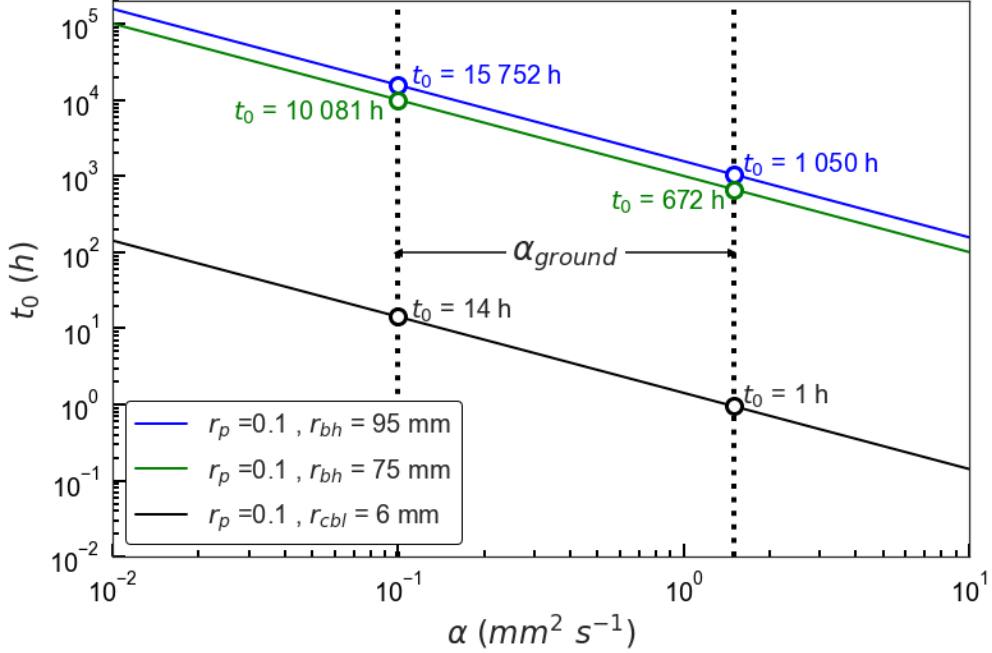


**Fig.1.1 :** Minimal oscillatory periods required to perform an O-TRT according to the minimal  $rp=0.1$  Eskilson's criterion [18]. Values of  $t_0$  are plotted against an arbitrary range of  $\alpha_{gr}$  values varying from 0.1 to  $1.5 \text{ mm}^2 \text{ s}^{-1}$  on a  $\log_{10} - \log_{10}$  scale.

To the authors' knowledge, the O-TRT method has not yet been validated in standard materials to determine  $\lambda$  and  $\alpha$ . Agar-gelled water, glycerine or Ottawa sand (OS) would be the most common and plausible materials to validate O-TRT (ASTM, 2008). However, agar-gel and glycerine have significantly different composition, contact resistance with the heating cable, and thermal properties compared to usual subsurface conditions. On the other hand, OS can properly represent a granular subsurface and was chosen as a reference material for the O-TRT validation.

One of the most frequently used standard OS is the ASTM graded sand (C-109) from Ottawa Silica Co., Ottawa, IL, USA. It is widely used due to its homogeneity and almost pure composition of silica ( $\text{SiO}_2$ ). Some studies have been carried out to determine  $\lambda$  and  $\alpha$  of OS at dry conditions with the guarded hot-plate (Kersten, 1949; Farouki, 1986), the thermostated water baths (Ukrainczyk, 2009) or the thermal conductivity probe methods (Yun et Santamarina, 2008; Tarnawski et al., 2009). Tarnawski (2009) estimated  $\lambda$  of this material with a thermal conductivity probe which uses a transient heat conduction method. They tested the sand in dry conditions under different compaction conditions, varying  $n$  from 0.32 to 0.40. The OS was also tested at different  $T$  ranging from 25 to 70 °C. They measured the highest  $\lambda = 0.350 \text{ W m}^{-1} \text{ K}^{-1}$  value when the thermal contact between grains was maximized at  $n = 0.32$  and for  $T = 70 \text{ }^\circ\text{C}$ . The lowest  $\lambda = 0.250 \text{ W m}^{-1} \text{ K}^{-1}$  was measured at  $n = 0.40$  and  $T = 25 \text{ }^\circ\text{C}$  (Tarnawski et al., 2009).

Ukrainczyk (2009) estimated  $\alpha$  of the OS C-109 with an experimental setup implying two water baths and using a transient heat conduction method to analyze this thermal property in laboratory conditions. In their study, they did not compact the sand and they calculated  $\alpha = 0.232 \text{ mm}^2 \text{ s}^{-1}$  at  $T = 22.5^\circ\text{C}$  and  $n = 0.39$  using a numerical inverse solution for 1D heat conduction (Ukrainczyk, 2009).

Reference materials can also be used to correct measured values from an apparatus. The standard needle probe method is a well-known procedure using a conventional measurement technique recommending to correct measured  $\lambda$  values with a reference material such as the OS (ASTM, 2008). To achieve this, a correction factor  $F$ , which is the ratio between a referenced theoretical  $\lambda$  value and the measured  $\lambda$  value, is calculated to adjust measurements estimated with a specific apparatus.  $F$  is used to account for estimation errors because the ILS equation described in Carslaw (1945) represents a simplification of a complex system, and the apparatus used to perform the tests has its own characteristics and layout. Hanson (2004) also showed that  $F$  is a function of  $\lambda$  using a large diameter needle probe due to the apparatus's heat storage.

The primary hypothesis of this study is that O-TRT using heating cables installed in granular deposits is an accurate method to estimate  $\rho C$  by evaluating independently  $\lambda$  and  $\alpha$  via an analytical approach. A secondary hypothesis is that  $\lambda$  and  $\alpha$  correction factors can be used to increase the accuracy of the analytical estimation. Thus, research was made with the objective of developing an apparatus and method to analyzed O-TRT conducted horizontally in granular deposits. This work includes: nine O-TRTs performed in Ottawa sand (OS) under laboratory conditions; five O-TRTs carried out in unconsolidated sediments under field conditions in Whapmagoostui-Kuujjuarapik (WK), a Cree and Inuit village located in Nunavik, North of Québec, Canada; and 3D numerical models developed to compare the results of the analytical approach of each aforementioned O-TRTs. Furthermore, a C-TRT was performed in both WK and OS materials to validate  $\lambda$  against the analytical O-TRT approach and the numerical solutions.

This work adopted two validation methods. First, as for the needle probe method, results of the O-TRT in the natural material were corrected by means of correction factors determined from laboratory O-TRT carried out in the standard OS. This was considered rational as both have the same heating cable,  $T$  sensors, ground materials and heat input rates. Second, numerical models representing conditions of a field case were simulated and compared to the analytical results. The analytical solution of the O-TRT proposed by Eskilson (1987) is only valid if the system is linear and time invariant (Giordano, Lamarche et Raymond, 2021; Oberdorfer, 2014), but an O-TRT depends on different variables such as power stability, accuracy of  $T$  sensors, and the properties of the material tested. Numerical models can therefore be used to simulate the temperature response independently from these field variables and assess  $\lambda$  and  $\alpha$  with valid accuracy.

## 1.2 Material and methods

### 1.2.1 Analytical Approach

Analytical solutions proposed by Eskilson (1987) can be used to estimate  $\lambda$  and  $\alpha$  with temperature observations from O-TRT. The linear component of the temperature response can be analyzed to estimate  $\lambda$  with the slope method derived by the ILS similar to the analysis of a C-TRT (Ingersoll, Zobel et Ingersoll, 1954; Carslaw et Jaeger, 1947). An interesting aspect of using a heating cable directly in contact with the analyzed ground is that there is almost no early time data to be neglected because the thermal resistance of the cable is negligible. The analytical approximations described by Eskilson (1987) and used by Oberdorfer (2014) and Giordano2021) can be used to assess  $\alpha$  after the estimation of  $\lambda$ . Finally, the estimated  $\lambda$  and  $\alpha$  from the heating period are used in Eq.1.1 to estimate  $\rho C$  (MJ m<sup>-3</sup> K<sup>-1</sup>).

$$\rho C = \frac{\lambda}{\alpha} \quad (1.1)$$

Following Oberdorfer (2014) and Giordano (2021), the analysis was carried out through the following steps:

1. The initial ground temperature  $T_0$  is inferred from temperature measurements immediately before the heat injection.  $T_0$  is subtracted from  $T$  recordings of the test to keep only the temperature difference  $\Delta T$  (Fig.1.2a).
2. The slope  $m$  is evaluated from thermal recovery observations according to  $\Delta T$  plotted on a logarithmic normalize time scale. A linear regression is calculated from the log linear portion of the data (Fig.1.2b). Power data corresponding to the O-TRT heating period is averaged to estimate the averaged heat injection  $\bar{Q}$  used in Eq.1.2.

$$\lambda = \frac{\bar{Q}}{4\pi \cdot L_{\text{cbl}} \cdot m} \quad (1.2)$$

3. The reference points, which corresponds to maximum, minimum and inflexion temperature oscillations (all separated by  $t_0/4$ ), are used to interpolate a natural log linear equation. The  $\Delta T$  data of the linear component are subtracted from the interpolated equation to keep only the oscillatory component (Fig.1.2c). A time window is selected where the electric signal reasonably approaches a theoretical sinusoidal equation, avoiding disturbed observations diverging from calculated temperature.
4. The analytical equation proposed by Eskilson (1987) describes the temperature behaviour (Eq.1.3) at the heat source ( $r_{\text{cbl}}$ ) in response to an oscillatory heat injection (Eq.1.4) for a linear time invariant system:

$$T_{\text{osc}} = -R_{\text{osc}} \left( \frac{Q_{\text{Amp}}}{L_{\text{cbl}}} \right) \sin \left( \frac{2\pi t}{t_0} - 2\pi\phi \right) \quad (1.3)$$

$$Q_{\text{osc}} = Q_{\text{Amp}} \sin\left(\frac{2\pi}{t_0} t\right) \quad (1.4)$$

The oscillatory thermal response is used to estimate the oscillatory thermal resistance  $R_{\text{osc}}$  and the phase shift  $\phi$  ( $0 < \phi < 1$ ) between the heat injection and the temperature response, which are both related to  $\alpha$  (Eq. 1.5 to 1.8; Fig.1.2d):

$$\phi = \frac{\text{time shift}}{t_0} \quad (1.5)$$

$$R_{\text{osc}}(rp) = \frac{1}{2\pi\lambda} \sqrt{\left(\ln\left(\frac{2}{r_{\text{eq}}\sqrt{2\pi}/\sqrt{\alpha t_0}}\right) - \gamma\right)^2 + \pi^2/16} \quad (1.6)$$

$$\phi(rp) = \frac{1}{2\pi} \tan^{-1}\left(\frac{\pi/4}{\ln\left(\frac{2}{r_{\text{eq}}\sqrt{2\pi}/\sqrt{\alpha t_0}}\right) - \gamma}\right) \quad (1.7)$$

$$rp = r_{\text{cbl}}\sqrt{2\pi}/\sqrt{\alpha t_0} \quad (1.8)$$

Eqs. (1.6) and (1.7) are Eskilson's (1987) expressions approximated to the first terms of the Taylor series expansion of the Kelvin function. They are valid provided that  $rp \leq 0.1$ . A non-linear least squares method is used to minimize the difference between the measurements and a calculated sinusoidal function ( $y = a \cdot \sin(bx - c) + d$ ), allowing to properly fit the analyzed power injection and oscillatory thermal response in the selected time window (Fig.1.2e). The peaks from the fitted equations are then located and used to calculate the averaged  $\phi$  based on the number of peaks pairing available in the time window (Fig.1.2e).  $\phi$  is used in Eqs. (1.7) and (1.8) to estimate  $\alpha$  with an equivalent radius  $r_{\text{eq}}$  because the temperature sensor is placed outside the heat source, causing a temperature delay. Note that  $r_{\text{eq}} = r_{\text{cbl}} + r_{\text{adj}}$  where  $r_{\text{adj}}$  is arbitrarily determined to be half of the DST centi-T temperature sensors thickness (7.5 mm) used in this study. This parameter is one of the most sensitive in the calculation of  $\alpha$ . Performing the O-TRT procedure in the OS reference material allows to correct uncertainties related to this arbitrary value.

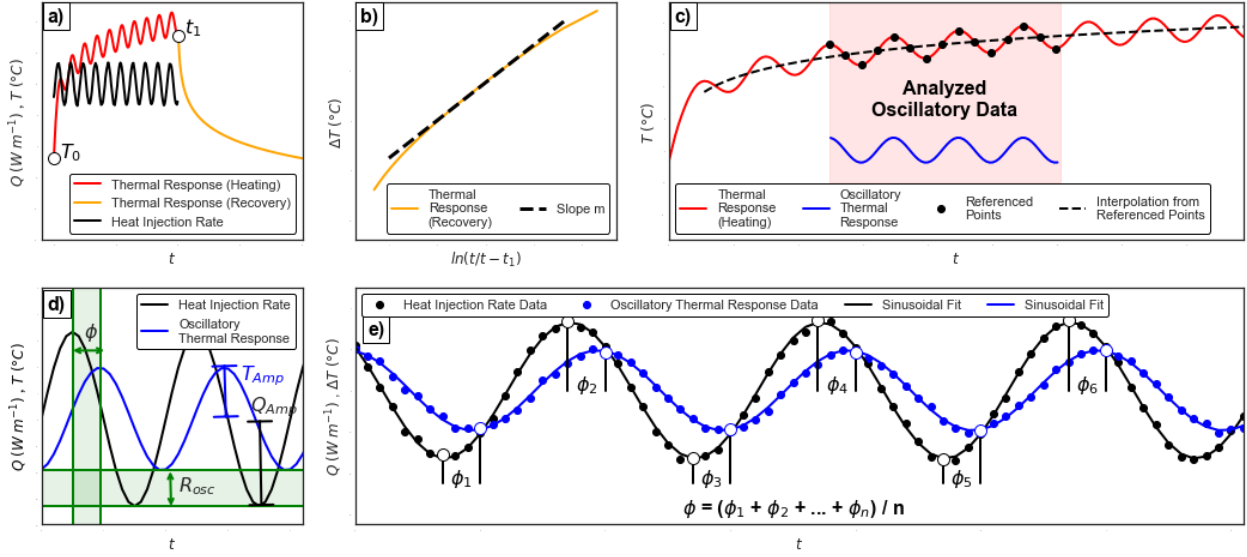


**Fig.1.2:** Steps for temperature data analysis of an O-TRT after Giordano (2021): (a) inferred  $T_0$  and  $\Delta T$  calculation for the evaluation of  $\lambda$  with the slope method (steps 1 and 2); (b) processing to extract the oscillatory thermal response (step 3); (c) oscillatory thermal response parameters implied in Eq (3) (step 4); (d) curve fitting method to calculate  $\phi$  for the  $\alpha$  assessment (step 4). *1.2.2 Measurement setup*

Two different types of material were tested under laboratory and in situ conditions to apply the O-TRT analysis described above. A 2.95-m-long heating cable producing a maximum of  $\approx 45$  W was connected to a power source (120V/15A) that was controlled by an apparatus adapted to produce an oscillatory electric signal (Fig.1.3) (Raymond, Giordano and Langevin, 2020). Oscillatory periods of 2, 4, 6 and 12 h were set according to the  $rp \leq 0.1$  criterion, which depends on the expected  $\alpha$  of the material.

Direct measurements and estimations errors can affect the accuracy at which the subsurface thermal properties can be determined. Data provided by the manufacturers were used to evaluate the uncertainty of direct measurements. Power and temperature data were collected every minute from a Hobo UX120 power data logger (0.5% accuracy) and DST centi-T temperature sensors (0.1 °C accuracy, 0.032 °C resolution, 20 s temperature response time), respectively. The DST centi-T is a commercial data logger provided by Star Oddi and made with a semiconductor sensitive to temperature changes connected to memory recording measurements in a submersible capsule. Normalized root-mean squared error (RMSE) was calculated to determine  $\delta m$  (step 2),  $\delta Q_{Amp}$  and  $\delta T_{osc}$  sinusoidal fits (step 4; Fig.1.2e). Direct measurement and estimations errors are included into  $\delta\lambda$ ,  $\delta\alpha$  and  $\delta\rho C$  according to Witte (2013).

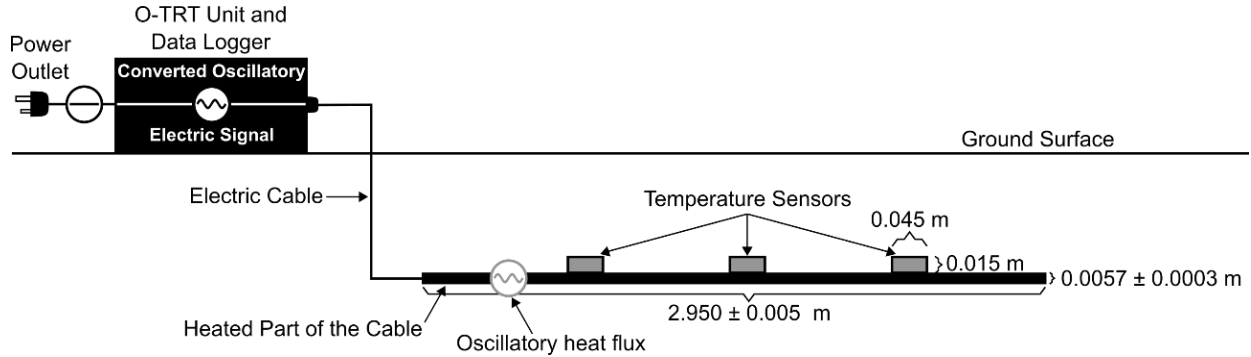


**Fig.1.3:** Diagram of an oscillatory thermal response test with a buried heating cable in a trench.

Temperature response time of  $T$  sensors is a crucial parameter for an O-TRT analysis since  $\alpha$  estimation is time dependant and  $T$  sensors can have significant diameter compared to the cable diameter ( $r_{\text{cbl}} = 2.86 \text{ mm}$ ). To this regard, two types of sensors were compared through O-TRT laboratory analyses for the same heat injection rate (Fig.1.4). DST centi-T sensors were selected for this study as it revealed better temperature sensitivity response time.

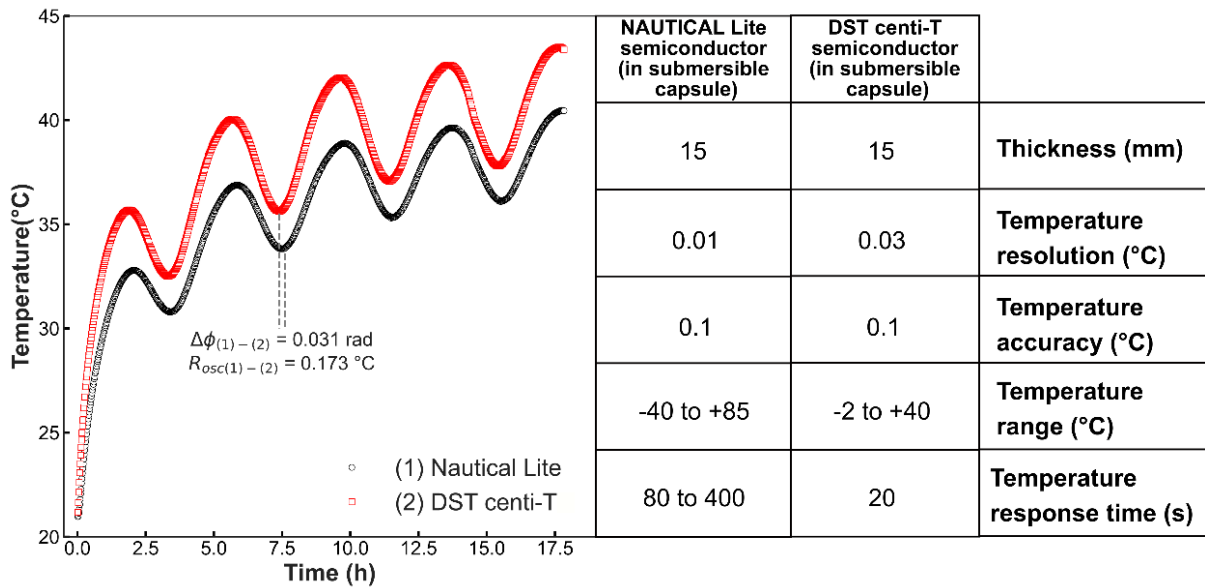


**Fig.1.4 :** Specifications of DST centi-T (Star Oddi) and Nautical Lite (Alpha Mach) sensors and temperature measurements for O-TRT with period of oscillation  $t_0 = 4 \text{ h}$ , power amplitude  $Q_{\text{Amp}} \approx 4 \text{ W m}^{-1}$ , phase shift difference  $\Delta\phi_{(1)-(2)} = 0.031 \text{ rad}$ , and oscillatory thermal resistance  $R_{\text{osc}(1)-(2)} = 0.173 \text{ °C}$ .

## 1.3 Experimental

### 1.3.1 Ottawa sand C-109

150 kg of OS were placed without compaction at laboratory conditions ( $T = 20\text{--}23\text{ }^{\circ}\text{C}$ ) in a 25 cm  $\times$  25 cm  $\times$  132 cm wooden box. The heating cable was placed along the box in central position and four DST temperature sensors were fixed to the cable every 30 cm (Fig.1.5). The bulk density of the OS (sand particles density  $2.67\text{ g cm}^{-3}$ ) was measured by submerging a known mass of sand in water and measuring the volume change of water. The resulting bulk density of OS was  $1.55\text{ g cm}^{-3}$  with a  $n = 42\%$ . A DST sensor was also placed outside the box to record laboratory air temperature during the tests. The temperature in the laboratory was maintained at  $\approx 21\text{ }^{\circ}\text{C}$  throughout the tests performed (Fig.1.5). The initial temperature for every test was considered at equilibrium conditions since DST sensors reached the same temperature recorded by the sensor installed outside the box. Three different  $t_0$  of 4, 6 and 12 h, along with three different power amplitudes ( $Q_{\text{Amp}}$ ) averaging 2.7, 4.0 and  $5.4\text{ W m}^{-1}$  and three  $\bar{Q}$  of 10.6, 11.8 and  $12.8\text{ W m}^{-1}$  were tested. Therefore, a total of nine O-TRTs were performed, with temperature values ranging from 20 to  $45\text{ }^{\circ}\text{C}$  for sensors D1 to D4 (Fig.1.5).

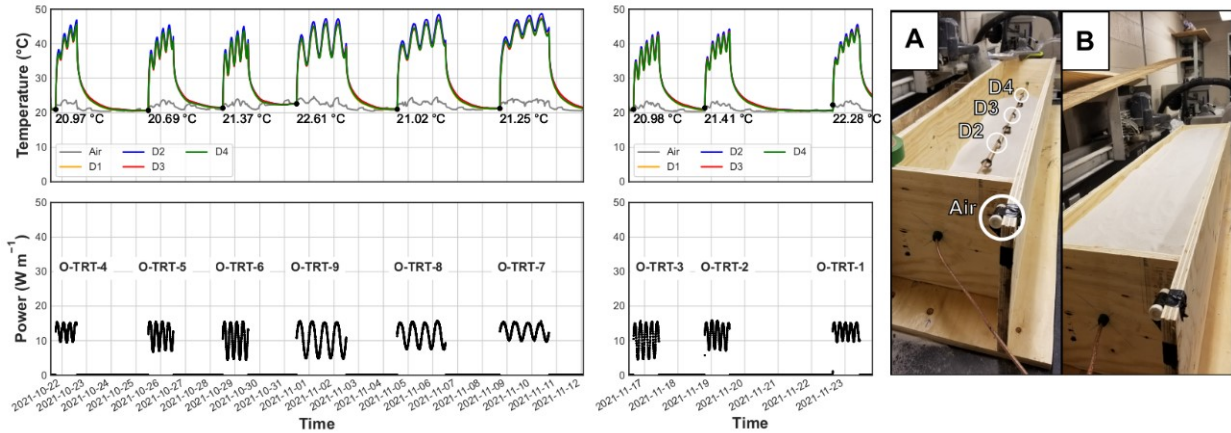


**Fig.1.5:** Temperature and power data recovered from the O-TRTs performed in the OS at laboratory conditions and view of the wooden box (A) half filled with the OS with temperature sensors attached to the heating cable and; (B) fully filled with the OS.

### 1.3.2 Whapmagoostui-Kuujjuarapik sand

Off-grid northern communities in Canada heavily rely on fossil fuels for both electricity and space heating production (Hydro-Québec, 2021). Sustainable and renewable energies such as geothermal are considered to reduce greenhouse gas emissions and provide energy independence for Inuit and First Nation communities (Belzile et al. 2017; Giordano and Raymond, 2019; Comeau, Giordano and Raymond, 2020). As part of a field campaign aiming to assess the potential of underground thermal energy storage systems

in sub-arctic climate, five O-TRTs were carried out in a sandy subsurface at the Centre d'études nordique (CEN) in Whapmagoostui-Kuujjuarapik (WK), Nunavik, Québec, Canada (Longitude -77.7470°, Latitude 55.2765°, Elevation 19 m). Data were collected from 11<sup>th</sup> to 20<sup>th</sup> of July, 2021.

The top of the trench was composed of an organic soil layer (0.00-0.05 m below ground level (b.g.l.)) and the underlying deposits were homogeneous sands with medium grain size. The first 0.45 m b.g.l. are almost dry while the deeper part of the trench appears to have a water content < 30%.

The heating cable was placed at the bottom of a trench excavated with a depth of 1.3 m and a length of 3.7 m. Three DST sensors were fixed to the cable every 40 cm (Fig.1.6). Another sensor was placed at 2 cm b.g.l. to record ground surface temperature during the tests. Excavated material was used to backfill the trench with care in reproducing the original stratigraphy. Undisturbed temperature of the ground was ≈9.25 °C according to temperature recorded over the whole period. The time between two consecutive tests was sufficient to ensure that the ground returned to its undisturbed temperature, except for the O-TRT-10 performed from the 13<sup>th</sup> to the 14<sup>th</sup> of July. Also, daily temperature variations did not influence the execution of the tests (Fig.1.6). Three O-TRTs with  $t_0 = 2$  h were performed with different  $Q_{Amp}$  of 2.5, 3.8 and 5.4 W m<sup>-1</sup> and three different  $\bar{Q}$  of 11.0, 12.1 and 12.9 W m<sup>-1</sup>. Two O-TRTs were performed with  $t_0$  of 4 and 6 h,  $Q_{Amp}$  of 2.3 and 2.4 W m<sup>-1</sup> and  $\bar{Q}$  of 13.1 and 13.1 W m<sup>-1</sup>, respectively. Throughout all these tests, the power injection was less stable than in lab tests due to local power grid fluctuations. Temperature measurements of sensors D2 to D4 are shown in Fig.1.6.

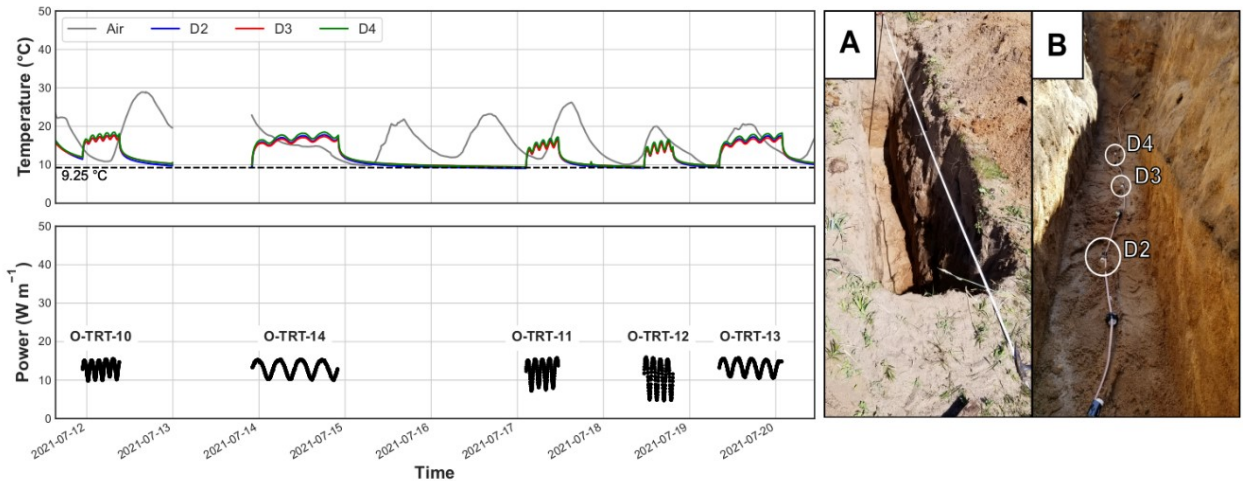


**Fig.1.6:** Temperature and power data obtained from the O-TRTs performed at the study site in Whapmagoostui-Kuujjuarapik and (A) general view of the trench and excavated material at the study site in Whapmagoostui-Kuujjuarapik and; (B) close-up of the heating cable and temperature sensors installed at the bottom of the trench.

### 1.3.3 Analytical approach correction

OS values reported by Tarnawski (2009) and Ukrainczyk (2008) were determined at  $n = 40\%$ :  $\alpha = 0.232 \text{ mm}^2 \text{ s}^{-1}$  at  $22.5^\circ\text{C}$ ,  $\lambda = 0.250 \text{ W m}^{-1} \text{ K}^{-1}$  at  $25.0^\circ\text{C}$ ,  $\lambda = 0.260 \text{ W m}^{-1} \text{ K}^{-1}$  at  $40.0^\circ\text{C}$ . In this study,  $\lambda_{\text{theoretical}}$  was set to  $0.255 \text{ W m}^{-1} \text{ K}^{-1}$ , which is the averaged from  $\lambda$  values at  $25$  and  $40^\circ\text{C}$ , while  $\alpha_{\text{theoretical}} = 0.232 \text{ mm}^2 \text{ s}^{-1}$ . The OS results of this study  $\lambda_{\text{measured}}$  and  $\alpha_{\text{measured}}$  obtained from the analytical approach described before were used to calculate correction factors  $F_\lambda$  and  $F_\alpha$  as follows:

$$F_\lambda = \frac{\lambda_{\text{theoretical}}}{\lambda_{\text{measured}}} \text{ and } F_\alpha = \frac{\alpha_{\text{theoretical}}}{\alpha_{\text{measured}}} \quad (1.8)$$

Correction factors are of paramount importance to correct uncertainties related to  $r_{\text{eq}}$  and the heat storage of the heat source and  $T$  sensor used.  $r_{\text{eq}}$  is one of the most sensitive parameters in Eqs. (1.6)-(1.8) and the calibration factors help decrease uncertainty in the final estimation of  $\lambda$  and  $\alpha$  in real-case applications. As mentioned in the ASTM D5334 standard (ASTM, 2008), correction factors should be determined for each type of apparatus and  $T$  sensor intended for field test.  $F_\lambda$  and  $F_\alpha$  values were calculated for each sensor and O-TRT. We assumed that once the correction factor is known, the testing unit can be used in any geological material having thermal properties within the same order of magnitude as the reference material. These correction factors are not needed for the numerical approach described below but only for analysis with Eskilson's (1987) solutions.

### 1.3.4 Numerical approach validation

The main heat transfer mechanism associated with performed O-TRTs was diffusion. The numerical domain to simulate an O-TRT requires three dimensions due to asymmetric conditions (temperature sensor on one side of the cable) and heat storage complexity around the heating cable. Numerical models solved the conduction equation below to simulate a temperature profile at any time.

$$\frac{\partial(\rho C_{\text{eff}} \Delta T)}{\partial t} + \nabla \cdot (\lambda_{\text{eff}} \cdot \nabla T) + A_{\text{eff}} = \text{Overall heat source/sink} [\text{W m}^{-3}] \quad (1.9)$$

The commercial finite-element software Feflow (Diersch, 2014) was used to perform 3D numerical simulations in this study. A homogeneous and isotropic material without groundwater flow was assumed and internal heat generation was assigned to the elements of the heating cable to represent the heat injection. This internal heat generation value is equivalent to the measured power varying with time divided by the estimated length and cross-sectional area of the cable. Internal heat generation was preferred to common boundary conditions (BC) in Feflow due to the following reasons: temperature inside the heating cable would have needed to be known for 1<sup>st</sup> and 3<sup>rd</sup> kind BC while temperature was recorded by sensors outside the heating cable; 2<sup>nd</sup> kind BC defines an inflow/outflow of energy per area and time at a relative temperature. This means that 2<sup>nd</sup> kind BC applied around the heating cable inside a 3D model transfers

energy from an element (e.g., inside the cable) to its adjacent element (e.g., outside the cable), and thus causing energy instabilities within the simulated heating cable; 4<sup>th</sup> kind BC can only be applied to nodes, while internal heat generation is applied to elements, therefore spacing between nodes in 3D would need to be smaller to provide a comparable uniform heat flux.

Python scripts were developed to perform simulations and analyze an O-TRT according to its physical and thermal properties. An initial uniform temperature for the whole domain was assigned at the beginning of each simulation. The time step was chosen to reproduce the sinusoidal power signal (Fig.1.2e) and since minimal simulated  $t_0$  was 2 h, it is required to have a time step below 6 min to have at least 6 points around the inflection temperature point. It was also considered reasonable to have a constant time step of 1 minute for the simulations to simplify RMSE calculation and match temperature data that were collected every minute. Simulated temperature at an optimized distance from the heating cable, which has been determined from a calibration process explained in the Appendix I, was calculated from all sensors positions, and spatially averaged for each time step to calculate the difference with the recorded temperature during the heating period. It is worth mentioning that there is no relation between  $r_{eq}$  and the optimized distance from the heating cable in Appendix I. Both approaches are standalone and independent, and the numerical approach was only used to assess the validity of the analytical approach. Simulated and observed temperature squared differences for all sensors were summed to calculate RMSE for the last three quarters of the heating period, considered to be the temperature response of the ground without the thermal disturbance effects. Performed tests in OS and WK sands are characterized by different conditions. Each case has its own discretized mesh, BC, and thermal properties, which are described in the following sections.

#### 1.3.4.1 Ottawa sand C-109

A 2D mesh centered on the heating cable position was generated in the  $x$ - $z$  plan with a minimal distance of 0.5 mm between nodes (Fig.1.7), and this mesh was then extruded in the  $y$  dimension. The mesh is refined around the heating cable because solved temperature has to accurately represents temperature measurements recorded at the scale of the DST sensor (15 mm). The sensors are not discretized or represented as a subdomain in the model since their thermal properties are unknown and due to difficulty to mesh their complex geometry. There is additionally no need to represent the sensors since the observed temperature response is mostly affected by the thermal properties of the sand. For simplicity, the  $\lambda$  and  $\rho C$  values of the cable and sensors were equal to the thermal properties of the sand. The mesh is coarser towards the extents of the  $x$ - $z$  plan where BCs define the border of the wooden box. Eleven 2D slices with 4,409 nodes and 8,732 triangular elements were then stacked horizontally and separated by  $\approx 0.1$  m (Fig.1.7) to simulate the box in 3D with a total of 87,320 elements. Six meshes ranging from 19,840 to 1,397,120 elements were considered to insure mesh independency. A minimum number of elements of 80,000 was

shown to ensure mesh independence. The total length of the heating cable is 1.318 m, and its cross-section has an area of  $3.12 \times 10^{-5}$  m<sup>2</sup> (Fig.1.7).

Cauchy BC was imposed all around the numerical model to represent a transfer rate boundary between air and the wooden box. A heat transfer coefficient  $l$  has to be set to peripheral elements, although this condition has a small effect on the solved temperature at sensors positions because the box volume is significant.  $l_{gr}$  of 10 W m<sup>-2</sup> K<sup>-1</sup> was considered as a reasonable value according to the temperature data recorded for the OS case. The numerical model is extruded for the entire box scale and a symmetrical boundary cannot be used to simplify the model since Cauchy BC can influence more temperature at the ends of the cable rather than the center.

First, eight different simulations were performed with python scripts to calculate their respective RMSE where  $\lambda$  ranging from 0.180 to 0.320 W m<sup>-1</sup> K<sup>-1</sup> was varied with constant steps of 0.020 W m<sup>-1</sup> K<sup>-1</sup> and  $\alpha$  was arbitrarily set to 0.230 mm<sup>2</sup> s<sup>-1</sup>. Thermal conductivity values were then interpolated with a cubic spline to determine the minimized RMSE giving an optimized  $\lambda$  value. In the second step of the analysis, the optimized  $\lambda$  value was set constant while 11 different  $\alpha$  values ranging from 0.100 to 0.350 mm<sup>2</sup> s<sup>-1</sup> were varied with constant steps of 0.025 mm<sup>2</sup> s<sup>-1</sup> through 11 simulations. The optimized  $\alpha$  value was then determined based on the minimized interpolated RMSE within its variability range. Based on simulations, it is determined that performing a third step to calculate the new optimal  $\lambda$  in the optimization process is not required since changes of the optimal  $\lambda$  value was always negligible.

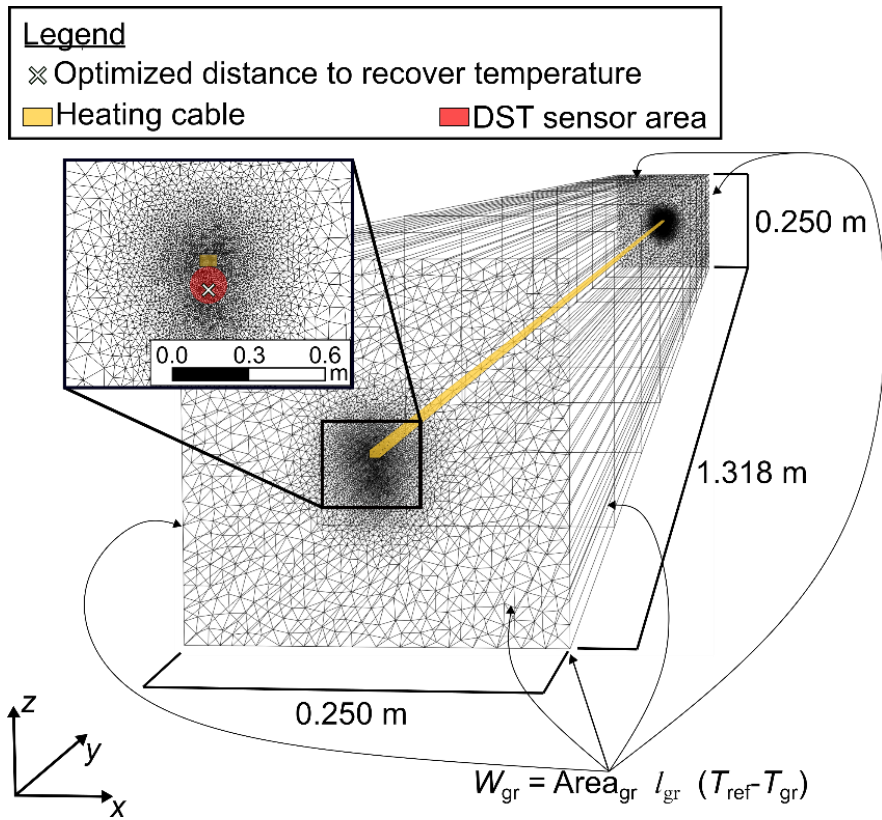


**Fig.1.7:** Three-dimensional mesh and boundary conditions for the numerical model developed for the OS case.

#### 1.3.4.2 Whapmagoostui-Kuujjuarapik sand

As for the OS numerical model, a 2D mesh centered on the heating cable position was discretized in the  $x$ - $z$  plan with a minimal distance of 0.5 mm between nodes (Fig.1.8). The mesh is refined around the heating cable and less refined towards the extents of the  $x$ - $z$  plan such as the OS model. Extents of the WK numerical model were determined at the ground surface limit and lateral boundaries placed such that the presence of lateral boundaries would not interfere with the O-TRT. Fifteen two-dimensional slices of the mesh with 4,776 nodes and 9,425 triangular elements were then stacked and separated by 0.5 m to simulate the O-TRT in 3D with a total of 113,100 elements. Six meshes ranging from 25,908 to 1,803,552 elements were simulated to ensure mesh independence that was reached with 45,000 elements. The total length of the heating cable is 3 m, and its cross-section has an area of  $3.12 \times 10^{-5} \text{ m}^2$  (Fig.1.8). The numerical model is extruded 1.5 m on both ends past the heating cable to model a finite heat source in the WK model since induced edge temperature effect at the ends of the cable are significant on solved temperature.

A Cauchy-type BC was set at the top of the model to apply a heat transfer BC and a  $l_{\text{gr}}$  of  $20 \text{ W m}^{-2} \text{ K}^{-1}$  was considered as a reasonable value according to the temperature data recorded for the WK case. Dirichlet BC is imposed to represent the surrounding steady-state ground temperature of  $9.25^\circ\text{C}$  at

the bottom of the numerical model. Lateral boundaries represent adiabatic conditions ( $0 \text{ W m}^{-2}$ ) to prevent thermal energy inflow/outflow (Fig.1.8).

The thermal property optimization process with the python scripts was similar to the OS case, but its  $\lambda$  and  $\alpha$  simulated range of values were different from the OS case. The first step simulated  $\lambda$  ranging from  $0.40$  to  $1.40 \text{ W m}^{-1} \text{ K}^{-1}$  with  $10$  uniform steps of  $0.10 \text{ W m}^{-1} \text{ K}^{-1}$ , with  $\rho C$  set arbitrarily at  $1.80 \text{ MJ m}^{-3} \text{ K}^{-1}$ . After the optimized  $\lambda$  is defined,  $\rho C$  was varied from  $1.00$  to  $2.20 \text{ MJ m}^{-3} \text{ K}^{-1}$  with  $12$  uniform steps of  $0.10 \text{ MJ m}^{-3} \text{ K}^{-1}$  to estimate the optimized  $\rho C$  (therefore  $\alpha$ ) minimizing the calculated RMSE.

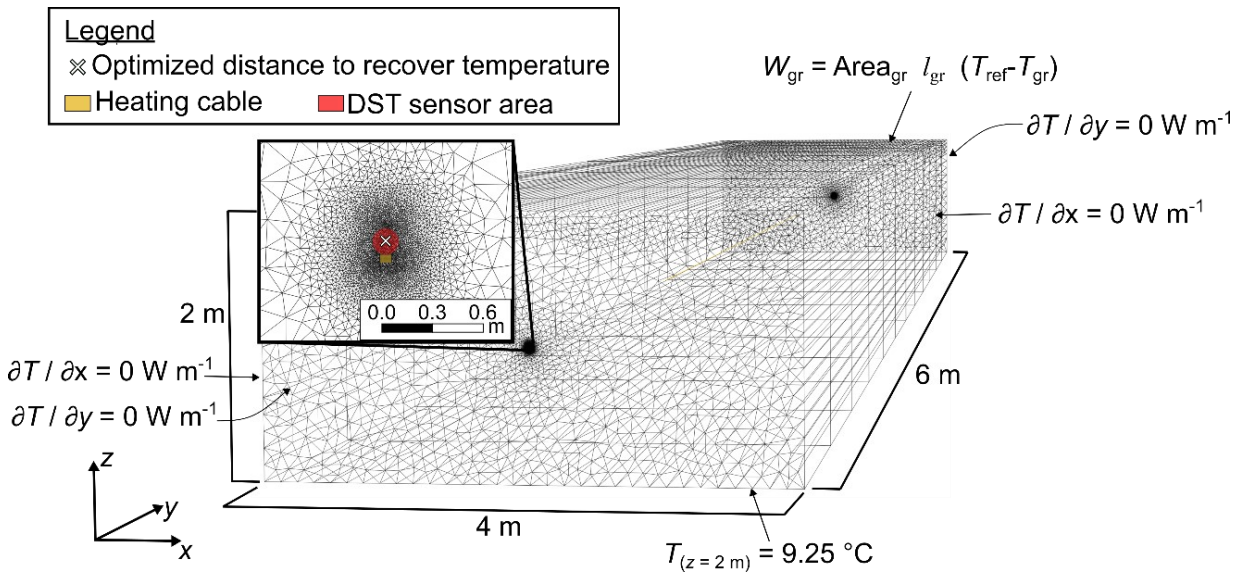


**Fig.1.8:** Three-dimensional mesh and boundary conditions for the numerical model of the WK case.

## 1.4. Results

### 1.4.1 Ottawa sand C-109

Analytically calculated  $\lambda$ ,  $\alpha$  and  $\rho C$  values of D1 to D4 sensors range from  $0.208$  to  $0.260 \text{ W m}^{-1} \text{ K}^{-1}$ ,  $0.177$  to  $0.274 \text{ mm}^2 \text{ s}^{-1}$ , and  $0.862$  to  $1.340 \text{ MJ m}^{-3} \text{ K}^{-1}$ , respectively. Calculated error values remain around 1-2% for  $\delta\lambda$ , and 5-6% for  $\delta\alpha$  and  $\delta\rho C$ .  $\phi$  values and their variability for each test decreases with increasing  $t_0$ .  $\lambda$  values have higher variability for O-TRTs with  $t_0 = 12 \text{ h}$  (O-TRT-7 to O-TRT-9) while  $\alpha$  has consistent values for O-TRTs with  $t_0 \geq 6 \text{ h}$  (O-TRT-5 to O-TRT-9) except for the O-TRT-4, which has a low  $Q_{\text{Amp}} = 2.8 \text{ W m}^{-1}$ .  $r_p$  is smaller than  $0.1$  for O-TRTs with  $t_0 = 12 \text{ h}$ , but the threshold is exceeded for the other O-TRTs.

Calculated  $F_\lambda$  and  $F_\alpha$  values of D1 to D4 sensors range from  $0.981$  to  $1.226$  and from  $0.847$  to  $1.310$ , respectively. O-TRT-8 and O-TRT-9 show highest  $F_\lambda$  variabilities while O-TRT-1 to O-TRT-6 ( $t_0 \leq 6 \text{ h}$ )

show similar values. O-TRT-5 to O-TRT-9 have similar  $F_a$  values, with O-TRT-7 to O-TRT-9 ( $t_0 = 12$  h) being the only tests having  $rp < 0.1$ .

Numerically calculated  $\lambda$ ,  $\alpha$ , and  $\rho C$  values have smaller variability than with the analytical approach within the OS sand. The averaged thermal properties are  $\lambda = 0.259 \text{ W m}^{-1} \text{ K}^{-1}$  ( $\sigma_\lambda = 0.001 \text{ W m}^{-1} \text{ K}^{-1}$ ),  $\alpha = 0.236 \text{ mm}^2 \text{ s}^{-1}$  ( $\sigma_\alpha = 0.004 \text{ mm}^2 \text{ s}^{-1}$ ),  $\rho C = 1.098 \text{ MJ m}^{-3} \text{ K}^{-1}$  ( $\sigma_{\rho C} = 0.021 \text{ MJ m}^{-3} \text{ K}^{-1}$ ). An example showing the optimization process of the O-TRT-1 is reported in Fig.1.9.

Averaged analytically solved uncorrected values, correction factors and numerically solved thermal properties values of O-TRTs in the OS sand are summarized in Table.1.1. D1 to D4 sensors for each O-TRT was averaged and their standard deviation was also calculated to simplify Table.1.1 presentation.

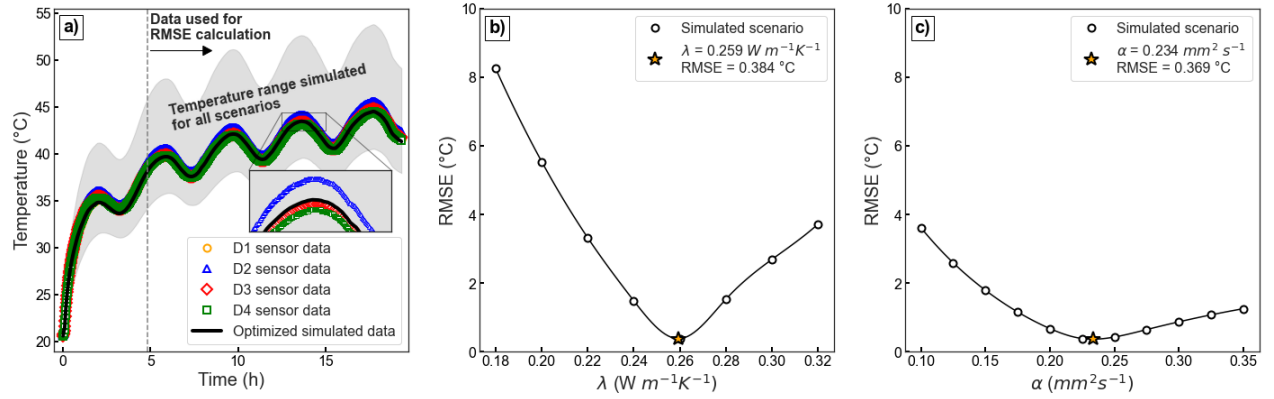


**Fig.1.9:** a) Simulated temperature (black line) representative of the optimized thermal properties (orange star in subfigures b and c) obtained by minimizing the RMSE calculated with temperature data of sensors D1 (orange circle), D2 (blue triangle), D3 (red diamond) and D4 (green square) for the O-TRT-1. RMSE interpolation trend function of b)  $\lambda$ , and c)  $\alpha$  according to the simulated scenarios for the O-TRT-1.

**Table 1.1 :** Analytically and numerically solved thermal properties values and calculated correction factors of O-TRTs for the OS sand.

O-TRT	$Q_{Amp}$ (W m <sup>-1</sup> )	$t_0$ (h)	Uncorrected analytical values						Correction factors		Numerical values		
			$\lambda \pm \sigma$ (W m <sup>-1</sup> K <sup>-1</sup> )	$\alpha \pm \sigma$ (mm <sup>2</sup> s <sup>-1</sup> )	$\rho C \pm \sigma$ (MJ m <sup>-3</sup> K <sup>-1</sup> )	$\phi \pm \sigma$ (rad)	$rp \pm \sigma$ (-)	$F_\lambda \pm \sigma$ (-)	$F_\alpha \pm \sigma$ (-)	$\lambda \pm \sigma$ (W m <sup>-1</sup> K <sup>-1</sup> )	$\alpha \pm \sigma$ (mm <sup>2</sup> s <sup>-1</sup> )	$\rho C \pm \sigma$ (MJ m <sup>-3</sup> K <sup>-1</sup> )	
1	2.6	4	0.244 ± 0.008	± 0.242 ± 0.013	± 0.993 ± 0.043	0.111 ± 0.002	0.121 ± 0.003	1.046 ± 0.032	0.962 ± 0.052	0.259 ± 0.000	0.234 ± 0.000	1.115 ± 0.000	
2	4.0	4	0.242 ± 0.005	± 0.227 ± 0.014	± 1.069 ± 0.060	0.114 ± 0.013	0.125 ± 0.003	1.053 ± 0.022	1.024 ± 0.061	0.259 ± 0.000	0.232 ± 0.000	1.106 ± 0.000	
3	5.3	4	0.235 ± 0.005	± 0.257 ± 0.014	± 0.917 ± 0.039	0.109 ± 0.002	0.118 ± 0.003	1.086 ± 0.025	0.905 ± 0.049	0.259 ± 0.000	0.241 ± 0.000	1.077 ± 0.000	
4	2.8	6	0.239 ± 0.011	± 0.191 ± 0.011	± 1.256 ± 0.094	0.104 ± 0.002	0.111 ± 0.004	1.069 ± 0.050	1.220 ± 0.073	0.258 ± 0.000	0.231 ± 0.000	1.127 ± 0.000	

5	4.2	6	0.241 0.010	$\pm$ 0.218 0.012	$\pm$ 1.105 $\pm$ 0.037	0.100 $\pm$ 0.002	0.104 $\pm$ 0.003	1.061 $\pm$ 0.045	1.066 $\pm$ 0.059	0.258 $\pm$ 0.000	0.239 $\pm$ 0.000	1.071 $\pm$ 0.000
6	5.5	6	0.246 0.012	$\pm$ 0.217 0.010	$\pm$ 1.135 $\pm$ 0.041	0.100 $\pm$ 0.002	0.105 $\pm$ 0.002	1.041 $\pm$ 0.049	1.074 $\pm$ 0.052	0.256 $\pm$ 0.000	0.236 $\pm$ 0.000	1.084 $\pm$ 0.000
7	2.6	12	0.216 0.008	$\pm$ 0.222 0.012	$\pm$ 0.973 $\pm$ 0.062	0.079 $\pm$ 0.001	0.073 $\pm$ 0.002	1.183 $\pm$ 0.043	1.046 $\pm$ 0.054	0.260 $\pm$ 0.000	0.232 $\pm$ 0.000	1.124 $\pm$ 0.000
8	3.9	12	0.235 0.024	$\pm$ 0.226 0.017	$\pm$ 1.046 $\pm$ 0.171	0.079 $\pm$ 0.001	0.073 $\pm$ 0.003	1.096 $\pm$ 0.109	1.030 $\pm$ 0.074	0.261 $\pm$ 0.000	0.236 $\pm$ 0.000	1.102 $\pm$ 0.000
9	5.4	12	0.229 0.023	$\pm$ 0.225 0.011	$\pm$ 1.020 $\pm$ 0.134	0.079 $\pm$ 0.001	0.073 $\pm$ 0.002	1.124 $\pm$ 0.110	1.034 $\pm$ 0.051	0.258 $\pm$ 0.000	0.239 $\pm$ 0.000	1.078 $\pm$ 0.000

#### 1.4.2 Whapmagoostui-Kuujjuarapik sand

Analytically calculated  $\lambda$ ,  $\alpha$ , and  $\rho C$  values of D2 to D4 sensors range from 0.735 to 0.914 W m<sup>-1</sup> K<sup>-1</sup>, 0.385 to 0.578 mm<sup>2</sup> s<sup>-1</sup>, and 1.419 to 2.322 MJ m<sup>-3</sup> K<sup>-1</sup>, respectively. Calculated error values remain around 1-2% for  $\delta\lambda$ , and 5-6% for  $\delta\alpha$  and  $\delta\rho C$ .  $\lambda$  values for O-TRTs tested in WK sand are similar, except for O-TRT-10, which has lower estimated  $\lambda$  values.  $\alpha$  show consistent values for O-TRTs except for the O-TRT-12, which has higher estimated  $\alpha$  values.  $rp$  criterion is respected for O-TRTs having  $t_0$  higher than 4 h, but the 0.1 threshold is exceeded for the O-TRT-10 to O-TRT-12 with  $t_0 = 2$  h. The majority of estimated  $\lambda$  values from D3 sensor data are higher than D2 and D4, while lower  $\alpha$  values were estimated with data measured from D3 sensor.

Numerically calculated  $\lambda$ ,  $\alpha$ , and  $\rho C$  values range from 0.895 to 1.137 W m<sup>-1</sup> K<sup>-1</sup>, 0.500 to 0.635 mm<sup>2</sup> s<sup>-1</sup>, and 1.721 to 1.834 MJ m<sup>-3</sup> K<sup>-1</sup>, respectively.  $\lambda$  and  $\alpha$  values for O-TRT-10 were overestimated compared to O-TRT-11 to O-TRT-14, while  $\rho C$  values are similar for all O-TRTs. An example showing the optimization process for O-TRT-14 is presented in Fig.1.10. It should be noted that  $\rho C$  variation has a small influence on RMSE (Fig.1.10c) compared to  $\lambda$  (Fig.1.10b) since  $\rho C$  affects thermal retardation translating to a displacement of the black line along the  $x$  axis in Fig.1.10a, while  $\lambda$  affects the material ability to conduct heat and result in a displacement of the black line along the  $y$  axis (Fig.1.10a). Moreover,  $\rho C$  variation (0.10 MJ m<sup>-3</sup> K<sup>-1</sup>) for the WK sand has less impact on RMSE values than  $\alpha$  variation (0.025 mm<sup>2</sup> s<sup>-1</sup>) for the OS sand numerical model (Fig.1.9c) as it represents only 6% of the fixed  $\rho C$  value (1.80 MJ m<sup>-3</sup> K<sup>-1</sup>) for the WK case, while it represents 11% of the fixed  $\rho C$  value (0.23 mm<sup>2</sup> s<sup>-1</sup>) for the OS case. The sensitivity of  $t_0$  from 2 h to 6 h was assessed, and varying  $t_0$  gives similar insensitive RMSE vs.  $\rho C$  variations.

Averaged analytically solved uncorrected values, correction factors and numerically solved thermal properties values of O-TRTs in the WK sand are summarized in Table 1.2. D2 to D4 sensors for each O-TRT was averaged and their standard deviation was also calculated to simplify Table 1.2 presentation.

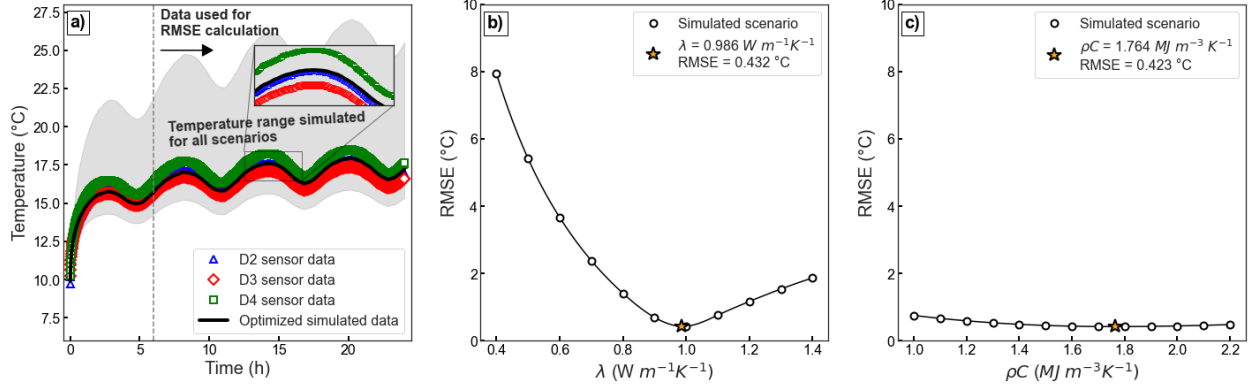


**Fig.1.10:** a) Simulated temperature (black line) representative of the optimized thermal properties (orange star in subfigures b and c) obtained by minimizing the RMSE calculated with temperature data of sensors D2 (blue triangle), D3 (red diamond) and D4 (green square) for the O-TRT-14. RMSE interpolation trend function of b)  $\lambda$ , and c)  $\rho C$  according to the simulated scenarios for the O-TRT-14.

**Table 1.2:** Analytically and numerically solved thermal properties values of O-TRTs for the WK sand.

O-TRT	$Q_{\text{Amp}}$ (W m⁻¹)	$t_0$ (h)	Uncorrected analytical values						Numerical values			
			$\lambda \pm \sigma$ (W m⁻¹ K⁻¹)	$\alpha \pm \sigma$ (mm² s⁻¹)	$\rho C \pm \sigma$ (MJ m⁻³ K⁻¹)	$\phi \pm \sigma$	(rad)	$rp \pm \sigma$	(-)	$\lambda \pm \sigma$ (W m⁻¹ K⁻¹)	$\alpha \pm \sigma$ (mm² s⁻¹)	$\rho C \pm \sigma$ (MJ m⁻³ K⁻¹)
10	2.5	2	$0.770 \pm 0.054$	$0.496 \pm 0.038$	$1.563 \pm 0.235$	$0.110 \pm 0.003$	$0.120 \pm 0.005$		$1.137 \pm 0.000$	$0.635 \pm 0.000$	$1.792 \pm 0.000$	
11	3.8	2	$0.832 \pm 0.057$	$0.467 \pm 0.033$	$1.794 \pm 0.263$	$0.113 \pm 0.003$	$0.124 \pm 0.005$		$0.895 \pm 0.000$	$0.515 \pm 0.000$	$1.735 \pm 0.000$	
12	5.4	2	$0.859 \pm 0.048$	$0.578 \pm 0.000$	$1.485 \pm 0.083$	$0.104 \pm 0.000$	$0.111 \pm 0.000$		$0.895 \pm 0.000$	$0.521 \pm 0.000$	$1.721 \pm 0.000$	
13	2.3	4	$0.848 \pm 0.039$	$0.453 \pm 0.064$	$1.907 \pm 0.373$	$0.089 \pm 0.004$	$0.089 \pm 0.007$		$0.986 \pm 0.000$	$0.557 \pm 0.000$	$1.764 \pm 0.000$	
14	2.4	6	$0.885 \pm 0.030$	$0.488 \pm 0.035$	$1.806 \pm 0.155$	$0.077 \pm 0.002$	$0.070 \pm 0.003$		$0.915 \pm 0.000$	$0.500 \pm 0.000$	$1.834 \pm 0.000$	

## 1.5 Discussion

In the WK case, the pronounced decreasing temperature trend before the heating period of O-TRT-10 suggests that the estimated initial ground temperature  $T_0$  was not at equilibrium, but rather on a transient state. This affected the assessment of  $\lambda$  for the analytical and numerical approaches used to reproduce observed temperature.  $\lambda$  was underestimated by the analytical approach since the slope determined during the thermal recovery period was affected by the return to the initial ground temperature that was not in total equilibrium. Thus, the ILS approximation only considered the thermal recovery and therefore higher  $m$  values were calculated.  $\lambda$  was overestimated for the numerical approach because the initial temperature of

the whole numerical model equaled to  $T_0$ , which corresponds to the temperature observed immediately before the heat injection. This caused an overestimation of the energy stored in the numerical model and therefore  $\lambda$  and  $\alpha$  are overestimated to fit temperature observations. This shows the importance of waiting for the ground to reach thermal equilibrium after the backfilling. However, the analytical approach found  $\alpha$  independently from  $\lambda$  with similar accuracy compared to other tests and  $T_0$  does not affect the estimation of  $\alpha$ , which can be useful for some situations where only  $\alpha$  needs to be assessed. Also, results from D3 show a different thermal response compared to D2 and D4. It is possible that the subsurface volume surrounding the cable had local heterogeneities that resulted in different thermal properties.

In the OS case, analytically solved  $\lambda$  values from O-TRT-7 to O-TRT-9 underestimated and exhibited a high variability compared to the other tests. The high variability within the estimated range of values is mainly caused by the small volume of the box. Thermal recovery data from these tests were highly affected by boundary effects because of stretched thermal injection periods compared to the other tests of shorter duration. After  $\approx 22$  h of heat injection, there was no relative temperature rise in subsequent  $t_0$  and heat was assumed to be lost through the box boundaries. Heat was injected for 48 h for O-TRTs using  $t_0 = 12$  h and the temperature response was significantly affected compared to the other tests, which heat injection that lasted for  $< 24$  h. The steady-state portion of the thermal recovery was thus difficult to interpret because the slope  $m$  is a highly sensitive parameter. The volume of the box would have to be increase in order to avoid boundary effects and significant OS temperature increase through extended heat injection. O-TRT-7 to O-TRT-9 could not be used to estimate the general  $F_\lambda$  related to the  $\lambda$  analysis because these boundary effects are not involved at the field-scale of an O-TRT, such as the WK case. However,  $F_\lambda$  values from O-TRT-1 to O-TRT-6 can be averaged ( $F_\lambda = 1.062$ ) as they were not affected by the boundary effects of the wooden box.

The numerical approach provides a more consistent assessment method because it aims to fit temperature for each time step in order to calculate thermal properties by optimization. This approach avoids ambiguous interpretations made by the analyst in an O-TRT or C-TRT and can help to assess thermal properties more accurately if the assumptions made for the conceptual model are reasonable. The  $\phi$  discrepancy between the analytical and numerical solutions was reduced when  $rp$  decreased ( $t_0$  increasing) as also highlighted by Oberdorfer (2014) (Fig.1.11). Analytically solved  $\alpha$  values show more consistent results when  $t_0$  is high for both the OS ( $\phi \approx 0.079$  for O-TRT-7 to O-TRT-9) and WK sands ( $\phi \approx 0.077$  for O-TRT-14). Higher  $t_0$  values would decrease even more the discrepancy between analytical and numerical values, but a small discrepancy of 0.002 rad was observed and thus, it would not significantly enhance analytically solved  $\alpha$  values. The required  $t_0$  value to test materials with  $\alpha \leq 0.23 \text{ mm}^2 \text{ s}^{-1}$ , such as the OS sand, is  $t_0 \geq 12$  h, while materials with  $\alpha \geq 0.50 \text{ mm}^2 \text{ s}^{-1}$ , such as the WK sand, required  $t_0 \geq 6$  h when using

the analytical approach. A sufficient number of  $t_0$  periods is required to have good data representation and valid  $\lambda$  and  $\alpha$  estimations. The analytical approach assumes a linear time invariant system and therefore, heat injection data between periods have to be similar. It is recommended to inject heat for at least three  $t_0$  for a single O-TRT and materials such as the OS sand need  $>36$  h of heat injection while materials such as the WK sand need  $>18$  h of heat injection. It was determined that  $F_\alpha$  values can only be averaged for  $rp < 0.1$  to correct  $\alpha$  values analytically solved in other materials such as the WK sand in order to comply with the  $rp$  criteria and ensure valid results. O-TRT-7 to O-TRT-9 can be averaged to represent the correction factor  $F_\alpha = 1.037$ , which is assumed to correct estimations related to the  $\alpha$  analysis and apparatus specifications.

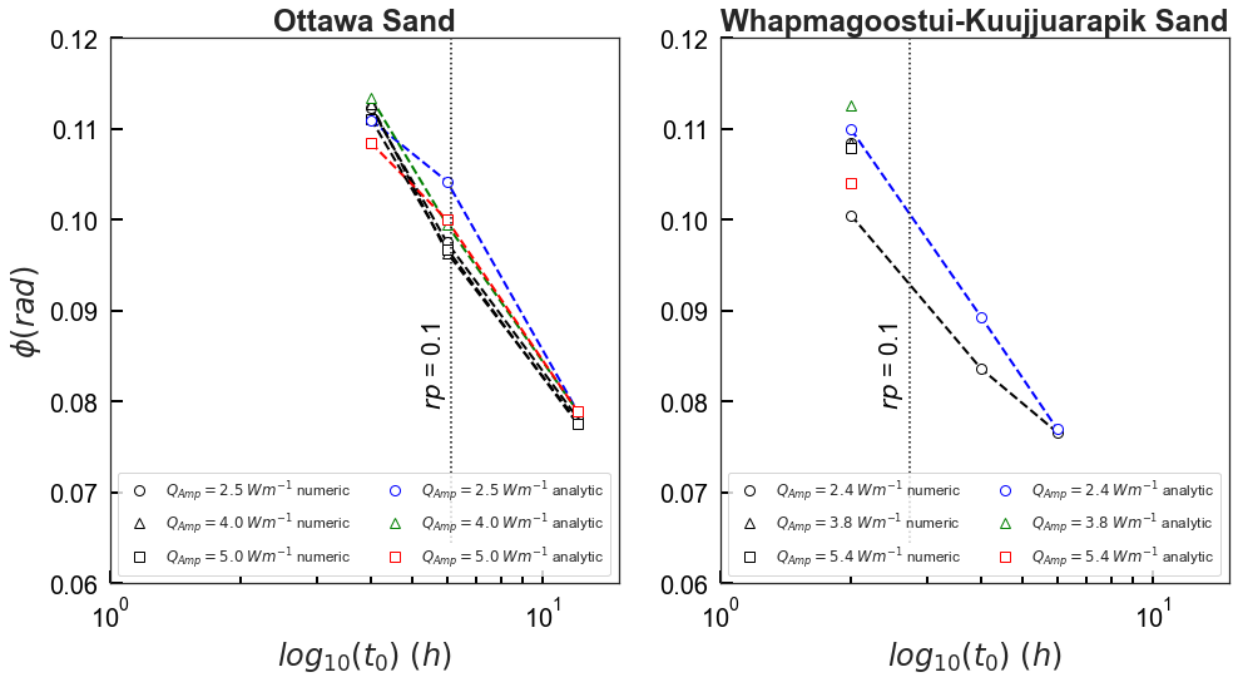


**Fig.1.11:** Comparison between analytical and numerical solutions of the phase shift parameter averaged for each O-TRTs in OS (left figure) and WK (right figure)

The averaged WK sand thermal properties from uncorrected analytically solved O-TRT-14 are  $\lambda = 0.878$  W m<sup>-1</sup> K<sup>-1</sup>,  $\alpha = 0.488$  mm<sup>2</sup> s<sup>-1</sup> and  $\rho C = 1.746$  MJ m<sup>-3</sup> K<sup>-1</sup>. Analytically solved  $\lambda$  and  $\alpha$  values can be multiplied by the calculated  $F_\lambda = 1.062$  and  $F_\alpha = 1.037$  to obtain final corrected values of  $\lambda = 0.932$  W m<sup>-1</sup> K<sup>-1</sup>,  $\alpha = 0.506$  mm<sup>2</sup> s<sup>-1</sup>, and  $\rho C = 1.849$  MJ m<sup>-3</sup> K<sup>-1</sup>. In comparison, numerically solved  $\lambda$ ,  $\alpha$ , and  $\rho C$  values for O-TRT-14 are 0.915 W m<sup>-1</sup> K<sup>-1</sup>, 0.500 mm<sup>2</sup> s<sup>-1</sup> and 1.834 MJ m<sup>-3</sup> K<sup>-1</sup>, respectively. Both  $F_\lambda$  and  $F_\alpha$  improved analytically solved values obtained from the O-TRT-14. The difference between numerical and analytical values without and with application of the correction factor changes from -4.0%, -2.4% and -4.8% for  $\lambda$ ,  $\alpha$ , and  $\rho C$ , respectively, to 1.9%, 1.2% and 0.8% when corrected. Margins of error related to  $\delta\lambda$  ( $\approx 2\%$ ) and  $\delta\alpha$

( $\approx 6\%$ ) have to be considered for the correction procedure applied on the estimated analytical values. The  $F_\lambda = 1.062$  corresponds to 6.2% of the uncorrected  $\lambda$  value and exceed  $\delta\lambda$  uncertainty. On the other hand,  $F_\alpha = 1.037$  corresponds to 3.7% of the uncorrected  $\alpha$  value and do not exceed  $\delta\alpha$  uncertainty. The correction procedure applied to  $\lambda$  values is significant since uncertainty related to  $\delta\lambda$  have less impact, while correction procedure applied to  $\alpha$  values is less relevant due to higher  $\delta\alpha$  values than the estimated  $F_\alpha$ . However, estimated correction factors can be enhanced under different conditions. The main measurement error related to  $\delta\alpha$  is the radius of the heating cable ( $\approx 5\%$ ) and increasing its accuracy could decrease the  $\delta\alpha$  and have less impact on  $\alpha$  than the  $F_\alpha$ . Also, as suggested in ASTM D5334 (ASTM, 2008) and described in Hanson (2004),  $F$  can vary when O-TRTs are performed in materials with different thermal properties due to heat storage of the heat source and sensors. Unfortunately, this study did not investigate the O-TRT method in material with a wide range of thermal properties and  $F$  dependency according to thermal properties was not estimated.  $F_\lambda$  and  $F_\alpha$  would have to be further investigated to determine if correction factors vary with various reference materials having different thermal properties. If performing the O-TRT method in materials of different thermal properties have a negligible influence on  $F_\lambda$  and  $F_\alpha$ , this would mean that the correction factors are mainly related to the non-negligible heat storage and transmission of the temperature sensors and heating cable used for the O-TRT apparatus. Correction factors are necessary for the O-TRT analytical approach to ensure the repeatability and accuracy of thermal properties estimations since it uses a new apparatus inducing uncommon heat storage and heat transmission (compared to conventional needle probes or boreholes).

The  $r_{adj}$  used to calculate  $\alpha$  with the analytical equation was arbitrarily determined to compensate the fact that sensors measured temperature just outside the heat source, but its value does not affect the validity of the  $\alpha$  calculation thanks to the correction factor. A different  $r_{adj}$  value would indeed change the estimated  $\alpha$  value, but the  $F_\alpha$  would balance this variation as it accounts differences in  $\alpha$  estimation according to the apparatus, including temperature sensors. However, its value may change for other temperature sensors having different characteristics, and therefore numerical models are necessary to compare the results. The position and large diameter of the temperature sensors is a limitation of this study, but the analytical and numerical approaches used allowed to address the issue. Future work could encompass the same analysis with sensors having smaller dimensions than the cable diameter, such as thermistor cable of fiber optic.

The estimated  $\lambda$  and  $\alpha$  from the numerically solved values for the OS sand are  $0.259 \text{ W m}^{-1} \text{ K}^{-1}$  and  $0.236 \text{ mm}^2 \text{ s}^{-1}$ , respectively, when averaged from O-TRT-1 to O-TRT-9. The value of  $\lambda$  is overestimated by 3.6% compared to the measured value of Tarnawski (2009) for a sand tested at  $25^\circ\text{C}$  and underestimated by 0.4% for a sand tested at  $40^\circ\text{C}$ . It also overestimated by 1.4% the  $\lambda_{theoretical}$  ( $0.255 \text{ W m}^{-1} \text{ K}^{-1}$ ) used for the

correction factor of the analytical solution. The averaged numerically solved  $\alpha$  value slightly overestimated the measured value from Ukrainczyk (2009) by 1.7%. Estimated values with numerical models lie within an acceptable  $\lambda$  range from the expected values of previous studies testing the OS sand (Tarnawski et al. 2009; Ukrainczyk, 2009). The results obtained with the numerical models for both WK (O-TRT-2 to O-TRT-5) and OS (O-TRT-1 to O-TRT-9) sands show that identifying thermal properties with numerical models is an accurate method to analyse O-TRTs regardless of  $t_0$ . Nevertheless, the analytical method shows a comparable accuracy when  $t_0$  is sufficiently high, with  $rp < 0.1$ . The analytical method is simple and can be used with any tests under the above-mentioned conditions while the numerical approach can be used with wider conditions but can be more complex to implement although both are independent.

This work suggests that O-TRT apparatus used to estimate thermal properties with the analytical method should ideally be corrected with referenced material and optionally be compared with numerical analysis before performing tests in materials with unknown thermal properties. It is also suggested to use stable power sources, such as a battery, to minimize assessment errors and increase accuracy.  $Q_{Amp}$ , opposed to  $t_0$ , does not significantly influence  $\alpha$  calculations. However, smaller  $T_{Amp}$  was observed for WK ( $T_{Amp} = 0.7 \text{ }^{\circ}\text{C}$ ) compared to OS ( $T_{Amp} = 1.7 \text{ }^{\circ}\text{C}$ ) performed under equivalent  $Q_{Amp}$  ( $2.6 \text{ W m}^{-1}$ ).  $Q_{Amp}$  has mostly an influence on the sinusoidal fit to the oscillatory temperature response because  $T_{Amp}$  is dependant on both  $\lambda$  and  $\alpha$  (Eqs. 1.8-1.9), ), as shown in both OS and WK cases. This can alter  $\alpha$  calculations if the temperature sensor does not have a valid accuracy. Alternatively, it is recommended to increase  $Q_{Amp}$  and use higher injection rates. Finally, analysts should also have in mind the depth of investigation of the O-TRT for the interpretation of their results. The radius of the thermal perturbation around the heat source, which can be expressed as  $\sqrt{\alpha \cdot t_0 / \pi}$  (Eskilson, 1987), is directly related to  $t_0$  and calculated  $\alpha$  values only pertain to a limited material volume when  $t_0$  is low. With  $t_0 = 2 \text{ h}$ , the penetration depth of the heat diffusion is 3.5 and 2.3 cm for materials with WK and OS properties, respectively. It rises to 8.5 and 5.7 cm when  $t_0 = 12 \text{ h}$ . It appears necessary to use a  $t_0$  inducing a radius of the thermal perturbation at least three times the diameter of the temperature sensor in order to minimize their thermal storage effect, although using  $t_0 = 6 \text{ h}$  for the WK sand and  $t_0 = 12 \text{ h}$  for the OS sand fulfilled this criterion. Also, analysis should consider that the ground contains heterogeneities and the excavated material has a different compaction than the undisturbed surrounding ground. Also,  $t_0$  should be maximized in order to increase the radius of thermal perturbation and thus, minimize non-representative thermal properties values due to ground local heterogeneities. Other apparatus configurations are currently investigated to minimize these uncertainties.

## 1.6 Conclusions

A novel experimental technique with heating cables and an analytical procedure to accurately determine  $\lambda$  and  $\alpha$  of shallow granular deposits were presented for the purpose of in situ TRT and GCHP

design. The Ottawa graded sand C-109 was used as a reference material to estimate correction factors and correct analytically solved  $\lambda$  and  $\alpha$  values from shallow unconsolidated deposits in WK. The analytical approach was then verified against a numerical approach for both materials. The difference between analytically and numerically solved values of  $\lambda$  and  $\alpha$  was 1.4% and 1.7%, respectively, for the OS sand while it was 1.9% and 1.2% for the WK sand. The analytical and numerical approaches proved to be effective when used to analyze the oscillating thermal response of a reference material (OS sand) and of a material with unknown thermal properties (sand tested in WK). However, the analytical approach for O-TRT with sufficient  $t_0$  better match thermal properties estimations of the numerical approach.

The higher the value of  $t_0$ , the better is the  $\alpha$  accuracy obtained from the analytical approach. The experimental setup and analytical approach remain a low-cost in situ TRT thanks to its easy implementation and quick analysis procedure. Accurate estimation of in situ thermal properties can be used to optimize the design of ground heat exchangers in shallow deposits and to solve complex heat transfer problems. Future work needs to be done with smaller temperature sensors to neglect thermal storage effects. This work can significantly contribute to in situ evaluation of  $\lambda$  and  $\alpha$  needed in various fields of geosciences.

# **Chapitre 2**

## **Design considerations for thermal energy storage systems in subarctic climate**

### **Titre traduit**

Considérations sur le dimensionnement de systèmes d'emmagasinement thermique souterrain en climat subarctique

### **Auteurs**

Hubert Langevin<sup>1</sup>, Nicolò Giordano<sup>1</sup>, Jasmin Raymond<sup>1</sup>, Louis Gosselin<sup>2</sup>, Martin Bourbonnais<sup>3</sup>

<sup>1</sup>Institut national de la recherche scientifique centre Eau-Terre-Environnement (INRS-ETE), Québec, Canada

<sup>2</sup>Université Laval, Québec, Canada

<sup>3</sup>Cégep de Jonquière, Jonquière, Canada

### **Publié**

Conférence 2<sup>nd</sup> Canadian Geothermal Students' Days (Winnipeg, 2020)

### **Mots-clés**

stockage thermique souterrain; énergie géothermique; analyse de sensibilité; conception; climat froid

### **Keywords**

thermal energy storage system; geothermal energy; sensitivity analysis; design; cold climate

## Résumé

Les systèmes de stockage thermique souterrain représentent une technologie mature pouvant satisfaire à la demande en chauffage de bâtiments. L'exploitation de ces systèmes peut ainsi contribuer à une transition vers des énergies vertes durables dans le nord du Canada. Leur efficacité dépend fortement du dimensionnement et des conditions du sol dans lequel il est mis en œuvre. Cette étude présente une analyse de sensibilité des principaux paramètres influençant le stockage thermique souterrain effectué dans un sous-sol ayant une température initiale près du point de congélation. Des modèles numériques ont été simulés dans le logiciel Feflow pour estimer le coefficient de performance moyen de la pompe à chaleur pour 68 scénarios différents d'un système de stockage thermique souterrain avec 25 échangeurs de chaleur géothermique. Un scénario initial a été construit et le coefficient de performance a été moyenné pendant les périodes d'extraction de chaleur. Ensuite, 17 paramètres ont été variés à 10% et 30% de leur valeur initiale et leur coefficient de performance moyen calculé a été comparé au scénario de base. Les résultats mettent en évidence les paramètres devant être optimisés et estimés avec exactitude afin de maximiser l'efficacité des systèmes de stockage thermique souterrain. L'extraction et l'injection de chaleur, le ratio surface/volume, l'espace entre les échangeurs de chaleur, la disposition des échangeurs de chaleur en fonction de l'écoulement de l'eau souterraine et les propriétés thermiques du sol sont les paramètres ayant la plus grande influence sur la température de fonctionnement du système. Le scénario initial affiche un COP moyen de 2.92 sur 4 ans de fonctionnement. Le scénario pessimiste montre un COP moyen de 2.74, tandis que le scénario optimiste donne un COP moyen de 3.05. Cela conduit à une différence de gain d'énergie de 13 GJ (+5.3%) entre le pire et le meilleur scénario sur environ 5.6 ans d'extraction de chaleur.

## Abstract

Borehole thermal energy storage system (BTES) is a mature technology to provide heating needs of buildings. It can thus contribute to the transition to sustainable green energies in northern Canada. Its efficiency strongly depends on the design and the subsurface conditions in which it is implemented. This study presents a sensitivity analysis of the main parameters influencing BTES operating in the subsurface near freezing conditions. Numerical simulations were performed in FEFLOW to estimate the average heat pump coefficient of performance (COP) of 68 different scenarios of a BTES with 25 borehole heat exchangers (BHE). An initial scenario was constructed and the COP was averaged during heat extraction periods. Then, 17 parameters were varied at constant steps (10% and 30% of their initial value) and their averaged COP was compared to the base case scenario. Results highlight parameters that need to be accurately estimated and optimized in order to maximize BTES efficiency. Thermal power injection/extraction, surface/volume ratio, BHE spacing, BTES layout compared to local groundwater

direction and subsurface thermal properties are the parameters with the highest influence on the operating temperature. BTES initial scenario averages a COP of 2.92 over 4 years of operation. Worst-case scenario shows a mean COP of 2.74, whereas best-case scenario averages a COP of 3.05. This leads to a 13 GJ (+5.3%) energy gain difference between the worst and the best-case scenario over ~5.6 years of operation of heat extraction.

## 2.1 Introduction

Northern communities in Canada rely on fossil fuel to supply heating loads of their buildings. Ground-source heat pumps (GSHP) seem to be an interesting solution (Gunawan et al., 2020; Belzile et al., 2017). They can supply base-load heating needs and reduce fuel oil consumption which is the principal energy source of those communities. However, GSHP range of operation is commonly limited by the temperature of the heat carrier fluid such as -6.7 °C (Belzile et al., 2017). An alternative to prevent low temperature operation is BTES, a technology combining low-enthalpy geothermal technology to other green renewable energies such as solar energy. Solar radiation is converted into heat and transferred to the ground. Heat is stored in the ground throughout summer (maximum solar radiation), and then extracted during winter (maximum building's heating load) to ensure operation of the heat pump within a reasonable temperature range. The study site is located near the *Centre d'Études Nordiques* (CEN) research station at Whapmagoostui-Kuujjuarapik in northern Quebec. The accessibility of the facilities and heating load data of the building was a major reason to choose this site. The regional geology is composed of a low-permeable granitic bedrock, partially covered by unconsolidated sediments, where fractures govern groundwater flow within either a confined or an unconfined aquifer (Fortier et al., 2011). Designing a BTES can be laborious since there are numerous parameters affecting its performance. This study aims to assess the main parameters and their impact on a BTES's performance in a subarctic climate. Numerical simulations are used to calculate the COP of different scenarios.

## 2.2 Methods

Numerical modelling is an efficient calculation method to solve coupled heat transfer problems such as BTES operation under groundwater flow influence. Numerical models were thus developed in Feflow (Diersch, 2014) to simulate groundwater flow and heat transfer mechanisms (advection, dispersion and phase change) of the studied granitic media near the CEN. The developed model distinguishes five input parameter categories: thermal and hydrogeological properties, boundary conditions (BC), BHE configuration, and heating power demand.

For this study, we considered a simplified conceptual model only made of granitic bedrock, the principal geological formation in the area. Eleven granitic outcrops were sampled near the CEN and

analyzed for thermal property assessment at the *Laboratoire Ouvert de Géothermie* (LOG) at INRS-ETE. Hydrogeological data from previous groundwater research studies in Whapmagoostui-Kuujjuarapik were inventoried (GPR International inc., 2002). These data were used to simulate and calibrate a regional 3D groundwater flow numerical model in order to estimate the bedrock's hydraulic conductivity and the hydraulic gradient at the CEN. This numerical model was also used to define hydrogeological BC to the BTES numerical model. Heat transfer BC were determined according to data collected from previous field campaigns. Ground temperature data were recorded at 1 and 2 m depth below ground level over the 2018-2019 period in unconsolidated sediments near the CEN. Air temperature data recorded at the CEN's meteorological station (CEN, 2017) were also collected. These temperature data were used to define the surface temperature BC at the top of the model from 152 to 304 days. Ground temperature shows the insulating effect of the snow cover. A -1 °C surface temperature was therefore assigned from 0 to 152 days and from 304 to 365 days in order to represent this effect (Fig.2.1a). Temperature profiles recorded in observation wells (< 120 m depth) in the vicinity of the CEN were used to define a constant temperature boundary at the bottom of the model. The BTES is composed of 25 BHE spaced by 3 m forming a cubic storage volume of 1728 m<sup>3</sup> (12 m × 12 m × 12 m), with 864 m<sup>2</sup> (12 m × 12 m × 6 sides) of exposed surfaces with a minimal surface/volume ratio (0.5 m<sup>-1</sup>; Skarphagen et al., 2019). The initial BTES configuration was determined to obtain a reasonable thermal storage volume that keeps the heat carrier fluid temperature operating range above -6.7 °C to respect a lower operating threshold temperature typically available in commercial heat pumps. Extracted energy yearly profile (Fig.2.1b) of a yearlong inhabited residential building at the CEN in Whapmagoostui-Kuujjuarapik was estimated by the mechanical engineering team of Université Laval involved in this research project. Heating load was estimated with simulations in TRNSYS according to building plans and occupation, and then calibrated with the 2018-2019 diesel energy bills. Injected energy yearly profile was calculated according to the following elements: the recorded solar radiation data at the CEN's meteorological station from 2005 to 2016 (CEN, 2017); the maximum number of photovoltaic solar panels to be installed on the CEN's roofs (162 solar panels of 2 m<sup>2</sup>); a solar panel efficiency of 14% (standard crystalline silicon panel); a power loss of 5% due to dip and orientation of solar panels ([https://re.jrc.ec.europa.eu/pvg\\_tools/fr/](https://re.jrc.ec.europa.eu/pvg_tools/fr/)); a hypothetical 10% heat loss due to tank storage/heat circulation. The numerical model mesh of the initial scenario has 34,400 nodes, 63,745 prismatic triangular elements, 20 layers, 25 interconnected BHEs within 2 arrays (Fig.2.1a). The total borehole length was always equal to 300 m (12 m depth) even when the BHE spacing (parameter 1, Tab.2.1) and the surface/volume ratio (parameter 5, Tab.2.1) were varied (e.g. surface/volume ratio +10% = prismatic rectangle with edges of 6.99 m × 20.61 m and a depth of 12 m). Nodal distance of 0.47 m around BHE was defined according to Diersch (2011), and the mesh was refined around the BTES. Time steps of 0.1 days were used for ~5.6 years (1955 days). In the predefined energy yearly profile (Fig.2.1b), there is heat

injection from 120 to 274 days and no heat extraction the rest of the year. We assume isotropic and homogeneous material, transient fluid flow/heat transfer and groundwater flow in a fully confined aquifer for simplicity.

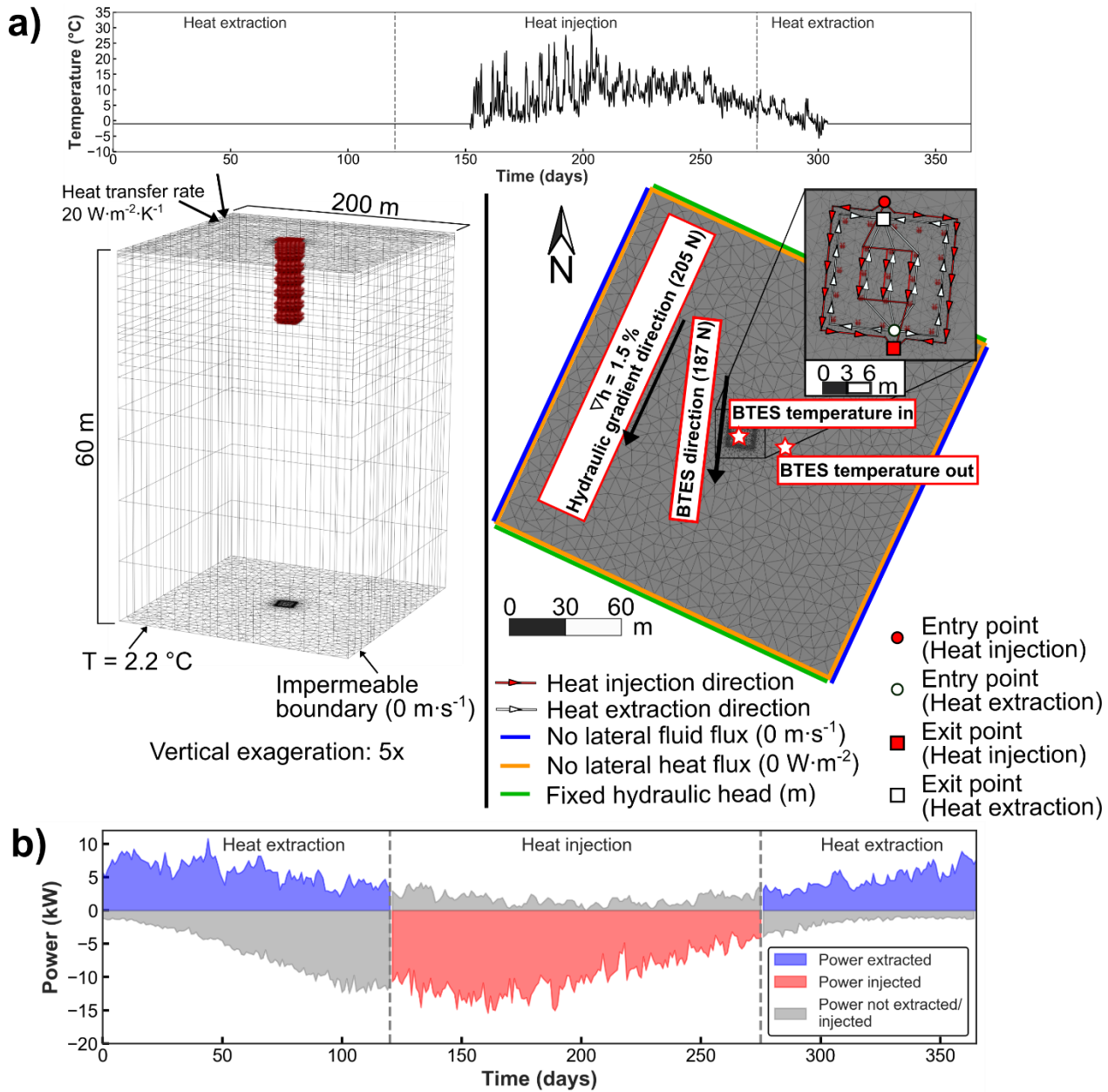


**Fig.2.1 :** a) Mesh construction and BC applied to BTES numerical model; b) energy yearly profile of the BTES where power extracted from the ground is the blue area, power injected into the ground is the red area and power from the heat load or the heat injection profiles not involved into BTES models is the grey area.

Python scripts were also developed to process and simulate a heat pump when there is heat extraction from the BTES. The outlet temperature fluid of the arrays is retrieved at each time step and the COP is calculated according to technical details of an ecoGEO 1-9 kW heat pump (EcoForest, 2020). Inlet temperature of the arrays at the next time step is then calculated according to the COP. The entry point in the BTES is considered as the heat pump's outlet while the exit point is considered as the heat pump's inlet. The entry point during heat injection periods is at the BTES' upstream while heat extraction starts from the BTES's downstream (Fig.2.1a). Two main parallel flow loops split between the BTES's core (9 BHE) and the BTES's periphery (16 BHE) are used for the heat injection and extraction operation modes (Fig.2.1a). Temperature at 6 m depth in the center of the BTES and 27 m out of the BTES' center is retrieved for each simulation (Fig.2.1a).

Parameters were varied one at a time by  $\pm 10\%$  and  $\pm 30\%$  of their initial scenario value to perform a sensitivity analysis. Each time a parameter was varied, the average COP of the four years of energy extraction simulation was estimated and then compared to the initial scenario. Table 2.1 presents all parameters considered for the sensitivity analysis where 68 different scenarios were run. Worst and best-case scenarios were then simulated according to the values producing the lowest COP loss (worst-case scenario) or the greatest COP gain (best-case scenario) from the base case scenario. These two scenarios use the power extraction and injection values of the base case scenario in order to compare energy savings on the same basis. The selected value of each parameter for the worst/best-case is the same as its base case scenario value if there is no difference or no positive COP difference. Finally, the base case scenario was also simulated without heat injection to compare the effect of thermal energy storage on the COP.

**Table 2.1:** Parameters values to perform the sensitivity analysis.

Category	Parameter	Base case scenario	Difference from initial scenario	
			$\pm 10\%$	$\pm 30\%$
(A) BTESS configuration	(1) Distance between BHE (m)	3.00	$\pm 0.30$	$\pm 0.90$
	(2) Borehole diameter (mm)	152.40	$\pm 15.24$	$\pm 45.72$
	(3) Difference between BTess and hydraulic gradient direction ( $^{\circ}$ )	0.00	$\pm 18.00$	$\pm 54.00$
	(4) BTES flow rate ( $m^3 \cdot s^{-1}$ )	$8.00 \cdot 10^{-4}$	$\pm 0.80 \cdot 10^{-4}$	$\pm 2.40 \cdot 10^{-4}$
	(5) Ratio surface/volume	0.50	0.05	0.15
		864.00	86.40	259.20
(B) Thermal property	(6) Borehole thermal resistance ( $m \cdot K \cdot W^{-1}$ )	$8.00 \cdot 10^{-2}$	$\pm 0.80 \cdot 10^{-2}$	$\pm 2.40 \cdot 10^{-2}$
	(7) $\rho C_p$ fluid ( $MJ \cdot m^{-3} \cdot K^{-1}$ )	3.80	$\pm 0.38$	$\pm 1.14$
	(8) $\lambda_{rock}$ ( $W \cdot m^{-1} \cdot K^{-1}$ )	2.88	$\pm 0.29$	$\pm 0.86$
	(9) $\rho C_p$ rock ( $MJ \cdot m^{-3} \cdot K^{-1}$ )	2.30	$\pm 0.23$	$\pm 0.69$

(C) Hydrogeological property	(10) $K$ ( $\text{m}\cdot\text{s}^{-1}$ )	$5.80\cdot10^{-7}$	$\pm0.60\cdot10^{-7}$	$\pm1.80\cdot10^{-7}$
	(11) $\Theta$ (-)	0.02	$\pm0.02\cdot10^{-1}$	$\pm0.06\cdot10^{-1}$
(D) Boundary condition	(12) $\nabla h$	$1.50\cdot10^{-2}$	$\pm1.50\cdot10^{-3}$	$\pm0.45\cdot10^{-3}$
	(13) Heat transfer rate BC ( $\text{W}\cdot\text{m}^{-2}\cdot\text{K}^{-1}$ )	20.00	$\pm2.00$	$\pm6.00$
(E) Heat power	(14) Average power extraction (kW)	5.42	$\pm0.54$	$\pm1.63$
	(15) Average power injection (kW)	-9.63	$\pm0.96$	$\pm2.89$

## 2.3 Results

Results for the initial scenario averaged a COP of 2.92 throughout 4 years, a maximum and minimum simulated heat carrier fluid temperature at the inlet heat pump of 18.16 °C and -2.52 °C, respectively. A maximum and minimum simulated temperature of 16.42 °C and -0.92 °C were recorded in the middle of the BTES at 6 m depth, respectively. A maximum and minimum simulated temperature of 4.18 °C and 1.72 °C, respectively, were recorded outside the BTES at 6 m depth (Fig.2.2).

The results of the sensitivity analysis and the averaged COP for the worst/best-case scenarios are shown in Table 2.2. The most influential parameters inducing a relative COP gain/loss > 1% in the 30% scenarios are parameters 1, 2, 5, 9, 10, 16 and 17 (Tab.2.2). The least influential parameters inducing a relative COP gain/loss < 0.1% in the 30% scenarios are parameters 7, 8, 11, 12, 13, 14 and 15 (Tab.2.2). It is worth to mention that the least and the most influential parameters in the 10% scenarios are the same, but the COP gain/loss is smaller. The worst-case scenario averaged a COP of 2.74 while the best-case scenario averaged a COP of 3.05.

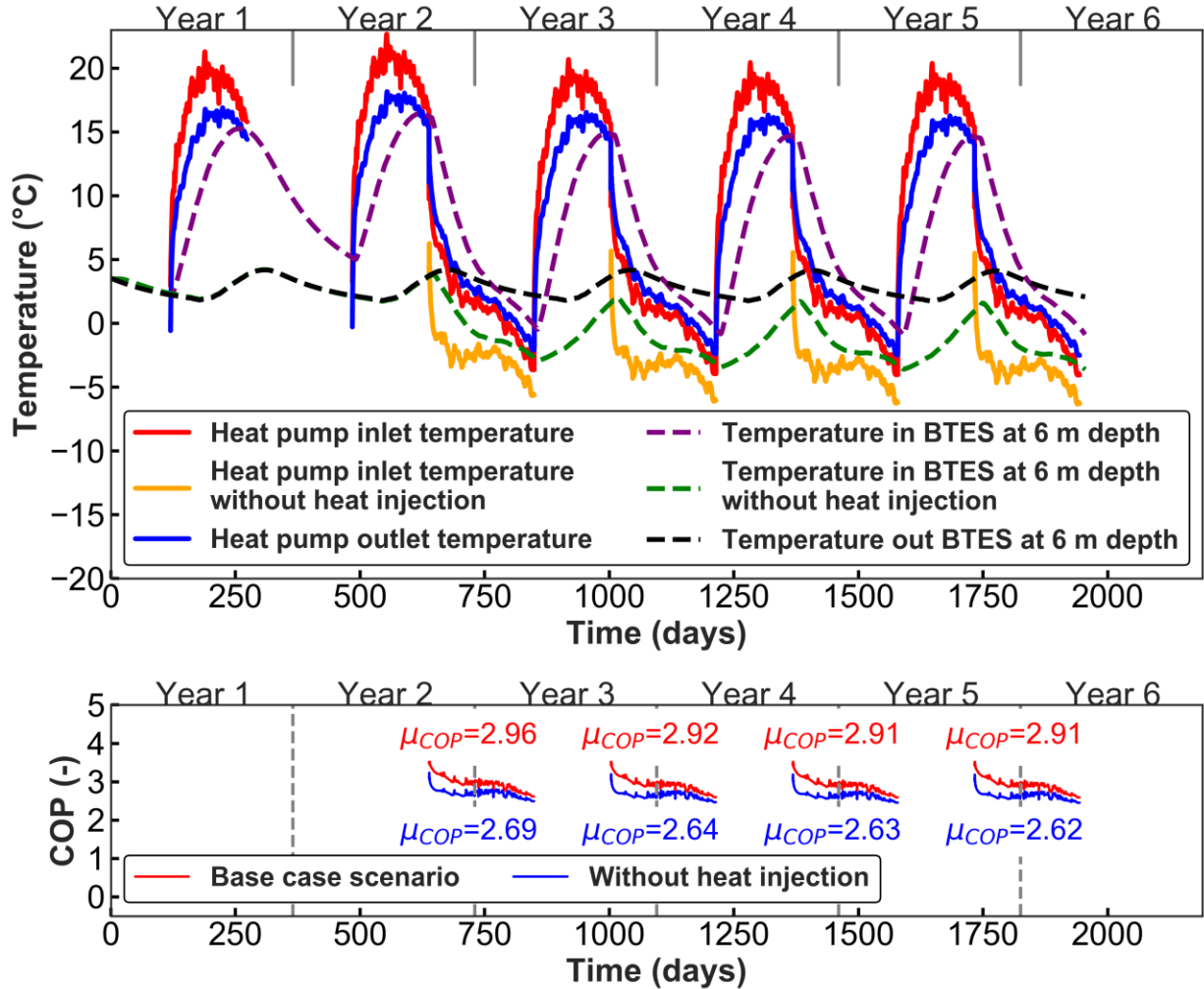


**Fig.2.2:** Base case scenario's simulated temperature and COP.

**Table 2.2:** Sensitivity of input parameters on averaged COP. The parameters used in the best case scenario are highlighted in green or stay unchanged from the base case scenario if a variation of the parameter's value does not induce a COP gain. Parameters used in the worst case scenario are highlighted in red.

		Average COP (-)			
Base case scenario		2.92			
Worst case scenario		2.74			
Best case scenario		3.05			
Category	Parameter	COP difference from initial scenario (%)			
		-30% scenario	-10% scenario	+10% scenario	+30% scenario
(A)	(1)	- 0.68	- 0.64	- 1.45	- 1.88
	(2)	-1.05	- 0.84	- 0.66	- 0.53
	(3)	- 1.06	- 0.87	- 0.81	- 0.78

	(4)	+ 0.28	+ 0.06	- 0.03	- 0.06
	(5)	-	-	- 2.27	- 4.87
(B)	(6)	+ 0.48	+ 0.16	- 0.15	- 0.46
	(7)	+ 0.27	+ 0.06	- 0.03	- 0.06
	(8)	+ 2.80	+ 0.78	- 0.66	- 1.72
	(9)	- 1.42	- 0.37	+ 0.30	+ 0.74
	(10)	+ 0.05	+ 0.01	- 0.02	- 0.05
(C)	(11)	- 0.05	- 0.02	+ 0.02	+ 0.05
	(12)	+ 0.05	+ 0.02	- 0.01	- 0.05
(D)	(13)	+ 0.06	+ 0.02	- 0.01	- 0.03
	(14)	+ 4.67	+ 1.51	- 1.57	- 4.46
(E)	(15)	- 4.64	- 1.55	+ 1.56	+ 4.68

## 2.4 Discussion

Simulated temperature and calculated COP (Fig.2.2) show that there is no cumulative thermal energy gain or loss within 6 years. The simulated temperature inside the BTES at 6 m depth increase during summer even in the scenario without heat injection suggesting that the BTES internal temperature is affected by seasonal surface temperature fluctuations due to the low depth of the BTES (12 m). However, the BTES cannot only rely on the seasonal temperature recharge during summer since the heat pump inlet fluid reaches a minimum temperature of -6.3 °C which is too close to the heat pump lower operating temperature threshold of -6.7 °C (Fig.2.2). The sensitivity analysis shows that the BTES performance can be significantly improved or decreased according to uncertainties of the input parameters. For example, the best-case scenario, which averaged a COP of 3.05 (Tab.2.2), can provide 265 GJ in energy savings with respect to the no-BTES case over 4 years of production, compared to 252 GJ for the worst-case scenario (COP of 2.74) and 245 GJ for the no-heat injection scenario (COP of 2.65; Fig.2.2). This difference, mainly due to various BTES configurations and geological properties (Tab.2.2), is expected to rise with increasing BTES volume.

Due to the short BHE length, the internal temperature of the BTES is affected by surface temperature variations and could potentially decrease if there is no snow cover insulating during the winter. Therefore, BHE layout is an important consideration to ensure the performance of this small-scale BTES. Thermal conductivity of the heat carrier fluid does not affect the BTES because its effects are included into the borehole thermal resistance calculation in Feflow to simplify the analysis. Simulated scenarios did not include parameter interdependency and may sometimes be unrepresentative. Parameters interdependency should be considered in a BTES design when materials and configurations are chosen based on thermal and hydrogeological in situ conditions of the studied site. For example, a permeable aquifer with significant

hydraulic conductivity can have a greater effect on the BTES's performance assessment. Indeed, the base case scenario with a greater hydraulic conductivity value would increase COP variations for the sensitivity analysis. Technical details of the ecoGEO 1-9 kW heat pump did not consider a propylene glycol-water mixture to calculate the COP. In fact, this mixture would induce a lower heat pump's COP. However, current results provide an initial assessment of the parameters influencing the BTES' performance with respect to the specific small scale BTES studied in Whapmagoostui-Kuujjuarapik.

## 2.5 Conclusions

This study presented a sensitivity analysis of the main parameters affecting the operation of a BTES for a small residential building in Whapmagoostui-Kuujjuarapik, northern Quebec. BTES configuration, subsurface thermal properties and heat injection/extraction rate are the most influential parameters to consider for BTES design. The sensitivity analysis provided a better understanding of the parameters involved in the design of a BTES operated in a subarctic climate in order to help the implementation of sustainable green energies in this northern community. Future activities will simulate technical details of a heat pump considering a propylene glycol-water mixture to calculate the COP, an artificial insulation at the top of the BTES to analyze heat transfer effects and an in-depth analysis of the energy yearly profile. Methods and tools developed in the present study will also be useful to anticipate BTES efficiency and optimize the design at any latitude worldwide.

# Chapitre 3

## **Solar assisted geothermal to reduce diesel consumption in off-grid subarctic communities: comparison between borehole thermal energy storage and borehole heat exchanger systems in Nunavik, Canada**

### **Titre traduit**

Systèmes géothermiques assistés par énergie solaire pour réduire la consommation de diesel des communautés éloignées en climat subarctique: comparaison de systèmes de stockage thermique souterrain et d'échangeur de chaleur à boucle fermée verticale en climat subarctique (Nunavik, Canada)

### **Auteurs**

Hubert Langevin<sup>1,2</sup>, Nicolò Giordano<sup>2</sup>, Jasmin Raymond<sup>1</sup>, Louis Gosselin<sup>3</sup>, Martin Bourbonnais<sup>4</sup>

<sup>1</sup>Institut national de la recherche scientifique, Centre Eau-Terre-Environnement, 490 rue de la Couronne, Quebec City, QC, G1K9A9, Canada

<sup>2</sup>Géotherma solutions Inc., 490 rue de la Couronne, Office 4332, Quebec City, QC, G1K9A9, Canada

<sup>3</sup>Université Laval, Mechanical Engineering Department, 1065 avenue de la Médecine, Québec, QC, G1V0A6, Canada

<sup>4</sup>Centre des technologies des énergies renouvelables et du rendement énergétique, Cégep de Jonquière, 2505 rue Saint-Hubert, Jonquière, QC, G7X7W2, Canada

### **Article prêt à soumettre**

### **Mots-clés**

Géothermie, stockage thermique, communautés éloignées, climat subarctique, coûts énergétiques

### **Keywords**

geothermal, thermal energy storage, remote communities, subarctic climate, energy costs

## Résumé

L'émission élevée de gaz à effet de serre et la forte dépendance aux énergies fossiles afin de produire de la chaleur et de l'électricité sont des enjeux de taille pour les communautés nordiques du Canada. Par conséquent, une transition énergétique vers des énergies renouvelables est nécessaire pour diminuer leurs coûts énergétiques élevés et leur exposition au marché imprévisible des énergies fossiles. Les panneaux solaires sont opérés sur une base intermittente en été ne peuvent pas être utilisés comme source d'énergie principale pour chauffer des bâtiments en hiver. De leur côté, les systèmes géothermiques peuvent être utilisés sur une base constante pour fournir du chauffage. Le couplage des deux énergies peut aider à améliorer l'efficacité d'un système géothermique de chauffage en convertissant l'énergie solaire en chaleur et en augmentant la température du sol en contact avec les échangeurs de chaleur. L'énergie solaire peut aussi être utilisée comme source d'énergie afin de fournir les besoins en électricité d'un système de chauffage. Ceci est intéressant pour réduire l'utilisation de l'électricité du réseau local produite avec de faibles rendements dans les communautés nordiques éloignées. Cette étude vise à mieux évaluer l'efficacité, les coûts énergétiques et la pertinence de différents systèmes de chauffage assistés par énergie solaire et opérés dans un climat subarctique caractéristique du sud du Nunavik en fonction d'une analyse approfondie des conditions caractéristiques du sol. En se basant sur des données de bâtiments et de la sous-surface obtenues à Whapmagoostui-Kuujjuarapik (Nunavik, Canada), les pompes à chaleur à compression et à absorption couplées à un système d'échangeur de chaleur en forage utilisant ou non un système de stockage thermique souterrain ont été comparées à l'aide de modèles numériques tridimensionnels. Les résultats montrent que les pompes à chaleur à absorption couplées à un système d'échangeur de chaleur en forage réduisent de 27% les émissions en CO<sub>2</sub> et les coûts énergétiques comparativement à des fournaises au mazout lorsque les besoins en électricité sont seulement fournis par le réseau local électrique. Les pompes à chaleur à compression offrent de meilleures économies d'émissions de CO<sub>2</sub> allant jusqu'à 61%, des coûts énergétiques sociaux jusqu'à 56% plus bas et des coûts énergétiques payés par un consommateur jusqu'à 60% plus bas lorsque 50 à 60% des besoins électriques sont couverts par l'énergie solaire. Un système considérant le stockage thermique en forage permet de balancer annuellement les charges imposées au sous-sol afin de faire face à la demande en chauffage des bâtiments nordiques qui est déséquilibrée. Ce travail donne un aperçu des approches à considérer pour adapter les systèmes géothermiques pour qu'ils fonctionnent dans un climat subarctique où la température du sol est juste au-dessus du point de congélation de l'eau et les charges du bâtiment sont déséquilibrées.

## Abstract

High greenhouse gas emissions and a strong reliance on fossil fuel to provide heating and electricity are major issues for remote northern communities of Canada. Therefore, a transition to renewable energies becomes increasingly needed to lower high energy costs and exposure to the unpredictable diesel market. Solar energy systems operate on an intermittent basis during summer and cannot be used as a primary source to heat buildings in winter. On the other hand, geothermal systems can be used on a constant basis to provide heating. Coupling the two can help to enhance the performance of a geothermal heating system by converting solar energy into heat and increase ground temperature surrounding the ground heat exchangers. Solar energy can also be used as a power source to provide electricity needs of a heating system, which is interesting to reduce the use of the local grid's electricity produced with low-efficiency generators in remote northern communities. This study aimed to better evaluate the efficiency, heating costs and the relevance of different types of solar-assisted geothermal systems operated in a subarctic climate characteristic of southern Nunavik based on a thorough analysis of typical ground conditions. Based on building and subsurface data obtained from Whapmagoostui-Kuujjuarapik (Nunavik, Canada), compression and absorption heat pumps coupled to borehole heat exchanger using borehole thermal energy storage systems or not were compared using three-dimensional numerical models. Results show that absorption heat pumps coupled to a borehole heat exchanger system reduce by 27% CO<sub>2</sub> emissions and energy costs compared to diesel furnaces when electricity needs are only provided by the local grid. Compression heat pumps significantly enhance savings of CO<sub>2</sub> emissions up to 61%, societal energy costs up to 56% and paid energy costs by the customer up to 60% when 50 to 60% of their electrical needs are covered by solar panels. A borehole thermal energy storage operating scheme with heat injection allows to annually balance the ground loads to supply the unbalanced heating demand of northern buildings. This work gives insights on how to adapt geothermal systems to be operated in a subarctic climate where the ground temperature is just above the freezing point and the building loads are unbalanced.

### 3.1. Introduction

Northern remote communities of Nunavik (North-of-Québec, Canada) mainly use diesel to supply electricity and heat to buildings because they are disconnected from the Quebec's provincial hydroelectric grid. Such communities are located in a subarctic to arctic climate where buildings need to be heated almost all year long with more than 8,000 heating degree days under 18 °C (HDD<sub>18</sub>; *Atlas climatique du Canada*, 2019). Heating consumes three times more fossil fuel than electricity production in northern communities of Canada, illustrating the clear need to reduce fossil fuel consumption related to space and water heating (Senate of Canada, 2014). Nunavik has valuable potential for electricity production with photovoltaic (PV) solar panels as there is an extended daylight period in the spring and summer. Wind also has interesting potential to produce electricity with wind turbines but on an intermittent basis (Deslauriers, 2008). Winter is the most energy-intensive period although buildings require to be continuously heated all year long. Thus, solar or wind power cannot provide continuous heating because they both strongly depend on the location and meteorological conditions.

A local alternative to supply heating is ground-coupled heat pump (GCHP) that has potential to reduce diesel consumption in subarctic communities (Giordano and Raymond, 2019; Kanzari, 2019; Gunawan et al., 2020). In fact, this system has the potential to provide continuous heating to a building because it can be exploited all year long and involves low-cost technology maintenance. GCHP using different ground heat exchanger (GHE) configurations can be considered since their potential varies with the geological setting. The most common GHE are open loops directly using groundwater as well as horizontal and vertical closed loops with antifreeze mixtures (Kavanaugh and Rafferty, 2014). Since ground temperature remains near 0 °C all year long in southern Nunavik, an open-loop GHE is not recommended for subarctic regions. The system would rely on groundwater near freezing conditions in regions where permafrost dynamics (Fortier et al., 2011) can involve complex GCHP operation. Alternatively, horizontal closed loops GHE (Belzile et al., 2017; Garber-Slaght and Peterson, 2017), borehole heat exchanger systems (BHE; Kanzari, 2019; Gunawan et al., 2020) and borehole thermal energy storage systems (BTES; Giordano and Raymond, 2019) can provide heating for a building in subarctic climate since antifreeze such as propylene glycol can be mixed with water and used as the heat carrier fluid (HCF) to prevent breakdowns or internal damage.

Compression heat pumps (COMP) are commonly used because of their high coefficient of performance (COP). Garber-Slaght and Peterson (2017) studied a horizontal GHE length of 1,463 m coupled to a COMP installed in Fairbanks (Alaska) to provide a building's heat load of 17.5 kW and calculated a COP of 3.7 in the 1<sup>st</sup> year. However, electricity in northern communities is commonly produced by diesel power plants having an efficiency ranging from 31 to 35% (Deslauriers, 2008), leading to high electricity production costs (Karanasios and Parker, 2016). Consequently, heat is produced with residential

fuel oil furnaces having an efficiency of about 80% (Natural Resources Canada, 2012), avoiding the use of electricity and high societal energy costs related to the operation of heating systems ( $Cost_{HSYS\ societal}$ ). Hydro-Québec (the local electricity provider in Nunavik) charges high electricity rate if the customer spends more than 40 kWh day<sup>-1</sup> (Hydro Québec, 2021) and thus, it would be profitable for customers to use other energy sources, such as PV energy, to provide COMP electrical needs (Gunawan et al. 2020). However,  $Cost_{HSYS\ societal}$  and energy costs for the customer ( $Cost_{HSYS\ customer}$ ) for a given heating system are different and it appears necessary to assess both energy costs along with greenhouse gases (GHG) emissions to compare different heating alternatives. It is necessary to compare COMP to other types of heat pumps not using electricity as a primary power source since COMP energy costs strongly depends on the amount of electricity supplied by PV panels (Gunawan et al. 2020). Absorption heat pumps (ABS) use a thermal compressor commonly powered by fossil fuel but it can also be powered by heated water. Event though they have a low COP, they can still achieve energy savings compared to conventional diesel furnaces. Belzile (2017) simulated a “Slinky” horizontal GHE to heat a residential building in Kangiqsualujjuaq (Québec) and have found that global energy savings are higher with a customized ABS ( $COP \approx 1.2$ ) than a COMP in the absence of PV panels to power the heat pump. They also recommended to use ABS since the HCF temperature at the heat pump inlet  $T_{inlet}$  decreased as low as -10 °C in their simulations, while conventional heat pump stops operating at  $T_{inlet} < -6.7$  °C to prevent internal damage (Geosmart Energy, 2013; Robur, 2014). However, Gunawan (2020) compared solar assisted COMP to ABS both coupled to BHE and found that COMP would provide more energy and financial savings than ABS when sufficient electricity was provided by PV panels.

BTES also uses borehole heat exchangers but operates differently. Their GHE allows storing thermal energy into the underground by circulating HCF in GHE and then later recover thermal energy according to the heating demand of the end user. This can facilitate seasonal thermal energy storage with the energy produced from PV panels in summer and recover heat in winter to heat a building, and thus, maximizing solar energy potential (Hellström, 1991). In Whapmagoostui-Kuujjuarapik, which is located above the 55<sup>th</sup> parallel, the sun is visible over 17 h a day during the summer solstice while during the winter solstice, the sun exposure is under 8 h a day. This highlights the importance of seasonal storage when considering solar energy in this region. Giordano (2019) presented numerical simulations made over 5-year operation for a large-scale BTES heated with solar thermal panels to evaluate diesel savings in the northern community of Kuujjuaq (Québec) facing a subarctic climate. They calculated that the system could achieve by the 3<sup>rd</sup> year of operation annual savings of 7,000 L of diesel related to low-temperature heating of drinking water at a pumping station.

Depending on the hydrogeological context and the type of GHE, groundwater flow can provide or dissipate thermal energy and affect the performance of the geothermal system (Gehlin, 2002; Catolico et

al., 2015). Uncertainties related to the thermogeological context also have a significant influence on the geothermal system efficiency and it is recommended to evaluate in situ ground properties (Casasso and Sethi, 2014). In a subarctic climate, the ground is near freezing conditions and buildings heating loads are more significant than in moderate climate due to the extreme weather conditions. Building loads are highly unbalanced towards heating and excessive heat extraction from the ground can induce water freezing (Dalla Santa et al., 2019). Garber-Slaght (2017) estimated that, in only three years, the COP of their pilot system had decreased by 14% because of ice formation around the GHE. They also suggested that active thermal recharge below 1 m, such as a BTES, is required to respond to the unbalanced building loads. In such settings, numerical modeling can be used to simulate both the effect of sensible and latent heat (Kane et al., 2001; McKenzie, Voss and Siegel, 2007; Anbergen et al., 2015). To this day, there is few field-based studies assessing the technical viability of geothermal systems in remote northern regions (Belzile et al., 2017; Garber-Slaght and Peterson, 2017; Kanzari, 2019; Giordano and Raymond, 2019; Gunawan et al., 2020). These studies have focused on the technical viability from the building's perspective as they used laboratory literature or laboratory measurements and made significant subsurface simplifications to simulate the geothermal system operation. Only Giordano (2019) included groundwater flow effects on the heating system and none of them compared groundwater flow effects on BHE and BTES. Also, they did not compare energy consumption and efficiency of different types of heat pump coupled to BHE and BTES at the same studied site as they were focusing on a single technology at a specific study site. Data and methods from their study can be improved with in situ assessment and advanced numerical modelling based on thorough analysis of ground conditions to properly compare geothermal systems. Comparing different types of GHE operation at the same site offers a better idea of their effectiveness and their limitations.

The objective of this work was to compare the viability of different solar assisted geothermal systems operating in a subarctic climate from a subsurface perspective where the ground is just above freezing conditions, building loads are unbalanced and energy costs are high. This work focused on BHE and BTES, which are closed loop systems potentially deployable on the whole Nunavik territory while other GHE are unfavorable in northern climate or restricted to specific geological conditions. BHE and BTES efficiency,  $Cost_{HSYS\ customer}$  and  $Cost_{HSYS\ societal}$  were compared to find their most appropriate use for northern communities according to the field site at the *Centre d'Études Nordiques* (CEN) research station in Whapmagoostui-Kuujjuarapik (WK), a community of 1,400 inhabitants in southern Nunavik. The facility is opened year-round since 1971 and there are many data available to justify an in-depth study comparing different type of geothermal systems. Three-dimensional transient conductive and convective heat transfer numerical simulations involving BHE and BTES operations and considering latent heat effects were conducted based on high-quality subsurface data. The simulations conducted also integrated Python scripts to simulate heat pumps affected by subsurface conditions. These numerical models and Python scripts

simulated the HCF temperature at the outlet/inlet of the heat pump through 20 years of operation. Modeling results were then used to compare efficiency, energy consumption, energy costs and CO<sub>2</sub> emissions for each GHE design. Different PV area scenarios were investigated to assess the energy costs and CO<sub>2</sub> emissions of the BHE and BTES heating systems.

### **3.2. Geographical, hydro-, and thermo-geological setting**

The CEN research station in WK (Longitude -77.7470°, Latitude 55.2765°, Elevation 19 m) is located in the southern part of the Nunavik territory. This village is characterized by a subarctic climate with discontinuous permafrost and 7,700 HDD<sub>18</sub>.

The adjacent Whapmagoostui (Cree First Nation) and Kuujjuarapik (Inuit) communities are bordered to the West by the Hudson Bay whereas the Great Whale River flows to the South, which is one of the most important rivers in northern Quebec with a 700 m<sup>3</sup> s<sup>-1</sup> average annual flow rate (Grainger, 1988). The regional bedrock is characterized by gneisses and granites of the Archean Bienville subprovince (Ciesielski, 1991) underlying unconsolidated sedimentary deposits. This sedimentary sequence is described from top to bottom as a succession of eolian or littoral sediments, deep water sediments and a discontinuous till veneer. The thickness of the unconsolidated deposits appears to be thicker towards the western part of the village while the presence of sediments is sporadic towards the east where there are predominantly outcropping bedrock hills. The CEN research station is located in the southern-eastern part of the community close to the river (Fig.3.1). The stratigraphy at the CEN is characterized by a silty sand overlying the homogeneous granitic bedrock. A georadar survey was conducted onsite in 2019 estimating a 15 to 20 m silty sand layer overlaying the bedrock (Appendix III).

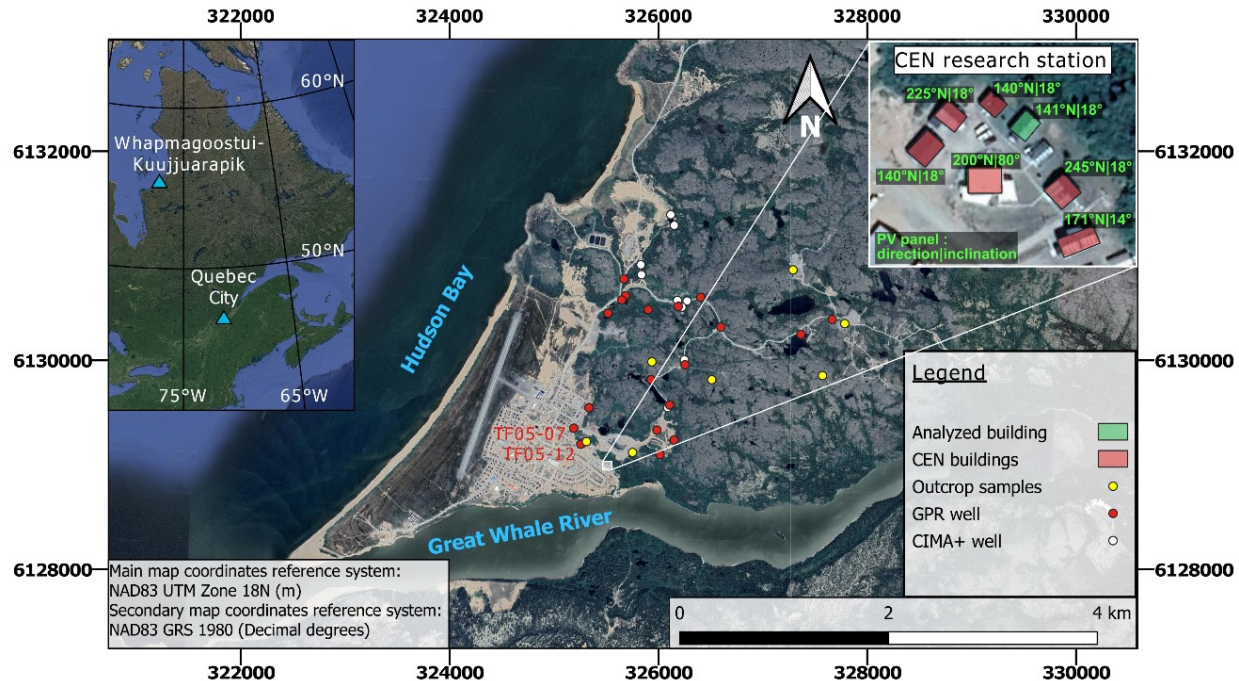


**Fig.3.1:** Location of data and infrastructures in Whapmagoostui-Kuujjuarapik and at the CEN research station.

Hydrogeological data from a pumping test (CIMA+, 2014) were used to calibrate a three-dimensional regional groundwater flow numerical model (Appendix IV) in order to estimate effective hydraulic properties of the regional unconsolidated sediments and bedrock. A hydraulic head difference of 3.5 m over 200 m ( $0.0175 \text{ m m}^{-1}$  horizontal hydraulic gradient) was calculated at the study site. This numerical model gave a steady-state solution while infiltration rate and water content in the aquifer vary through a year. Water is flowing through sand to reach the water table, which mainly sits below the top of the bedrock (CIMA+, 2014). Thus, water saturation and groundwater flow in the silty sand vary significantly through time while it can be considered constant in bedrock. Main groundwater recharge periods were correlated to hydraulic head monitoring from CIMA+ (2014), high rain precipitations levels (fall) and snow melting periods (spring) recorded by Environment Canada (2021; Fig.3.2). Details of the regional groundwater flow model including results at the CEN research station are described in Appendix IV.

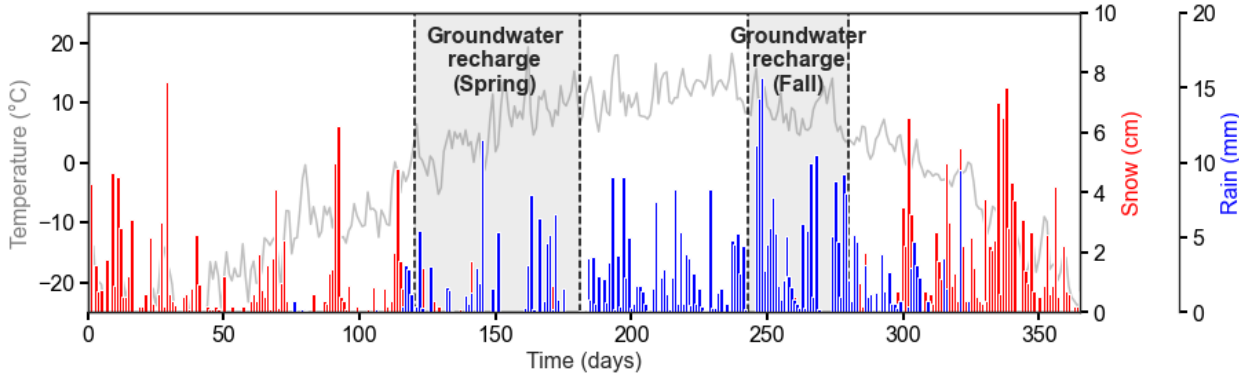


**Fig.3.2:** Yearly averaged temperature, rain, or snow precipitations from 2012 and 2013 measured by the Kuujjuarapik no. 7103536 meteorological station of Environment Canada (2021).

A complete thermogeological characterization was conducted from 2018 to 2021 by the *Institut national de la recherche scientifique*. As part of this work, several tests were performed:

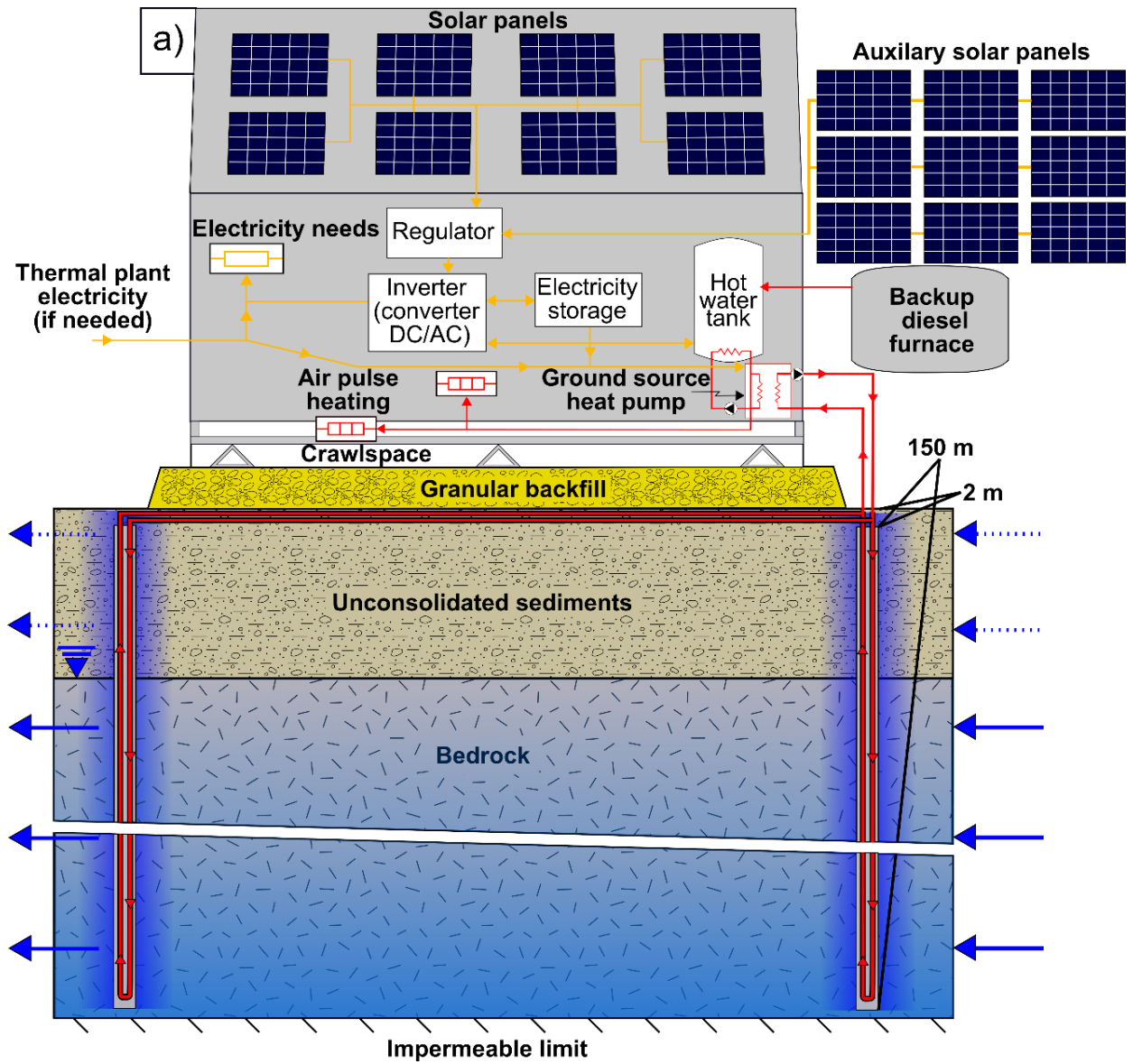
- Ground temperature at 0.5, 0.7, 1.0 and 2.0 m depth recorded from 2018 to 2020 near the CEN were measured (Appendix V);
- A thermal response test (TRT) with a constant heat injection rate was carried out in an observation well (TF05-12) near the CEN to estimate an effective in situ thermal conductivity of the bedrock, which was shown to be  $2.68 \text{ W m}^{-1} \text{ K}^{-1}$  (Appendix VI);
- Outcrop samples were collected to estimate an averaged bedrock volumetric heat capacity of  $2.29 \text{ MJ m}^{-3} \text{ K}^{-1}$  in laboratory condition;
- Horizontal shallow TRTs were performed with oscillatory heat injections to assess the in situ thermal conductivity and thermal diffusivity of the silty sandy deposits over which the CEN buildings lie. Thermal conductivity of the sandy deposits is  $0.92 \text{ W m}^{-1} \text{ K}^{-1}$  and volumetric heat capacity is  $1.76 \text{ MJ m}^{-3} \text{ K}^{-1}$  at 30% water content (Langevin et al., 2022);
- A temperature profile was recorded in the TF05-07 observation well where recorded values ranged from 0.5 to 3.0 °C.

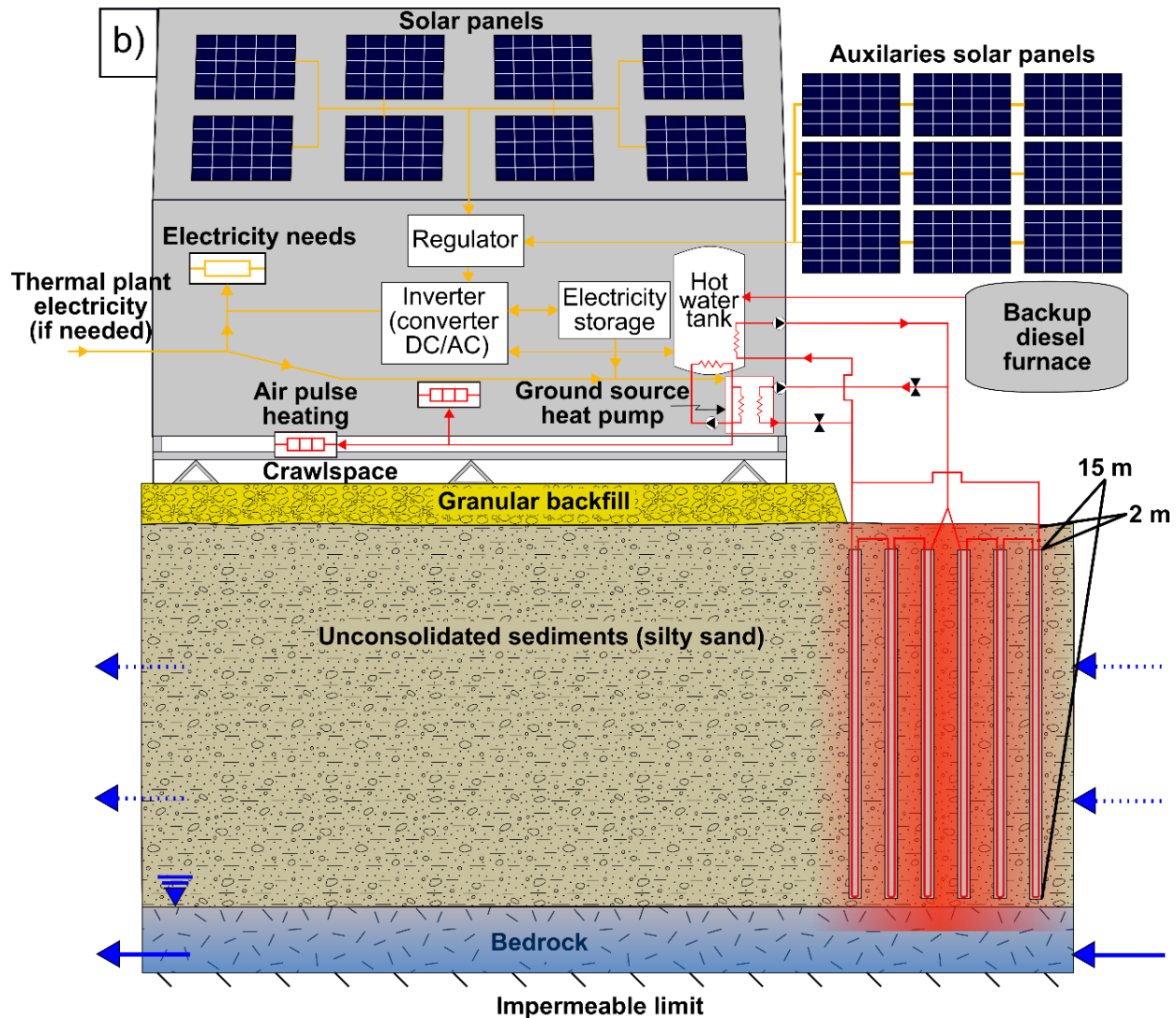
### 3.3. Method

#### 3.3.1 Conceptual Models

Conceptual models (BHE and BTES<sub>sand</sub>) were developed considering two distinct subsurface layers; a top layer representing silty sand material from 0 to 20 m depth and a bottom layer representing the granitic bedrock from 20 m to the bottom of each model (Fig.3.3a and Fig.3.3b). A BTES conceptual model

(Fig.3.3c) was also developed without a silty sand layer ( $\text{BTES}_{\text{bedrock}}$ ) to compare its efficiency to the other models since northern community buildings can be constructed directly on bedrock due to unconsolidated sediments scarcity. The BHE model without a silty sand layer was not developed since this material represents a small proportion of the total BHE length. GHE are designed to provide sufficient thermal energy to a building based on ground thermal properties and the heating demand. A heat extraction rate per GHE unit length  $P_{\text{GHE}}$  of 30 to 50  $\text{W m}^{-1}$  is commonly targeted in locations where undisturbed ground temperature  $T_0$  ranges from 7 to 12 °C (Kavanaugh and Rafferty, 2014). As demonstrated by Garber-Slaght (2017;  $P_{\text{GHE}} \approx 8 \text{ W m}^{-1}$ ) and Gunawan (2020;  $P_{\text{GHE}} \approx 17 \text{ W m}^{-1}$ ),  $P_{\text{GHE}}$  in a climate similar to WK must be reduced around 10 to 20  $\text{W m}^{-1}$  in order to avoid low HCF temperature and system breakdown since ground  $T_0$  range from 1 to 3 °C. As a first estimate, the required GHE total length for BHE and BTES models (Fig.3.3) was set to 300 m according to the results assessed via an analytical method by Gunawan (2020). Therefore, all numerical models developed below have the same total GHE length and internal configuration (Fig.3.4a) for the purpose of providing a proper comparison.





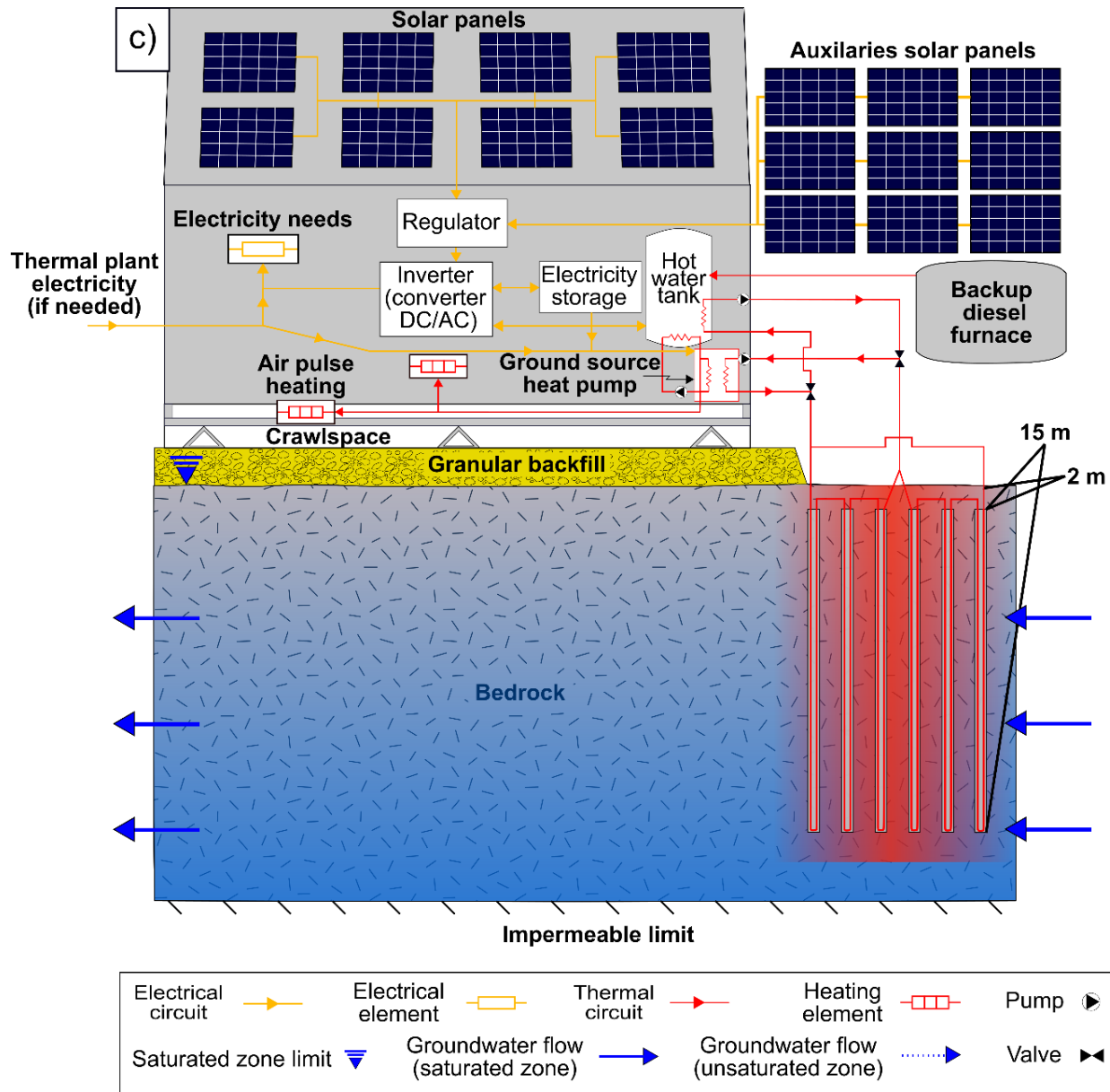


**Fig.3.3:** Simplified conceptual model of a typical building with a heat pump coupled to a) a BHE b) a BTES<sub>sand</sub> c) and BTES<sub>bedrock</sub>. Conceptual models represented are not to scale.

BHE and BTES have alternative ways to heat a building. BHE coupled to a heat pump are disposed to extract heat from the ground and optimally distanced to minimize thermal perturbation by other GHE. Gunawan (2020) simulated a single GHE to a depth of 300 m despite drilling rigs available in Nunavik commonly provide a maximum depth of investigation of  $\approx 200$  m. Giving this limitation, the model developed for the BHE system encloses two GHE of 150 m separated by 10 m, which are interconnected in parallel (Fig.3.4b). The BHE only extracts heat from the ground, while electricity is supplied from PV with

the maximal area possible if they were installed on the seven buildings at the CEN station (162 solar panels of  $2 \text{ m}^2$ ; Fig.3.1). The PV area total nominal power is 28 kW and the electricity produced by the area of PV panels can be stored in batteries  $P_{\text{EPV}}$ , which can be converted in alternative current by an inverter to power COMP or ABS and other electric devices. Power from the thermal power plant  $P_{\text{TP}}$  is used if there is not enough  $P_{\text{EPV}}$  to supply the heating system hourly. On the other hand, BTES coupled to a heat pump includes BHE disposed to store and retrieve thermal energy.  $P_{\text{EPV}}$  and  $P_{\text{TP}}$  can also be used to power COMP or ABS and other electric devices. Operating conventional thermal solar panels systems in a northern context has many technical or efficiency constraints. Moreover, thermal solar panels have a return on investment period three times greater than PV panels using direct connection (Le Roux et al., 2019). For these reasons, this study considered that excess electricity produced by PV panels is directly used and converted to heat  $P_{\text{HPV}}$  and stored in a hot water tank. Therefore, heat is injected in the ground when solar radiation is at its peak and PV electricity generated in excess is not used. The entry point of the injected heat is at the upstream BTES while heat extraction starts from the downstream BTES (Fig.3.4c). BHE in BTES models were distributed evenly in a ground cylinder diameter of 25 m with 20 GHE of 15 m length which correspond to a  $\sim 7,360 \text{ m}^3$  ground volume (Fig.3.4c). This configuration diminishes heat losses due to the cylinder shape minimizing the surface-volume ratio (Skarpagen et al., 2019; Langevin et al., 2021). The top of BHE and BTES were placed at a 2 m depth below the surface to minimize the impact of seasonal ground surface temperature variations (Fig.3.3).

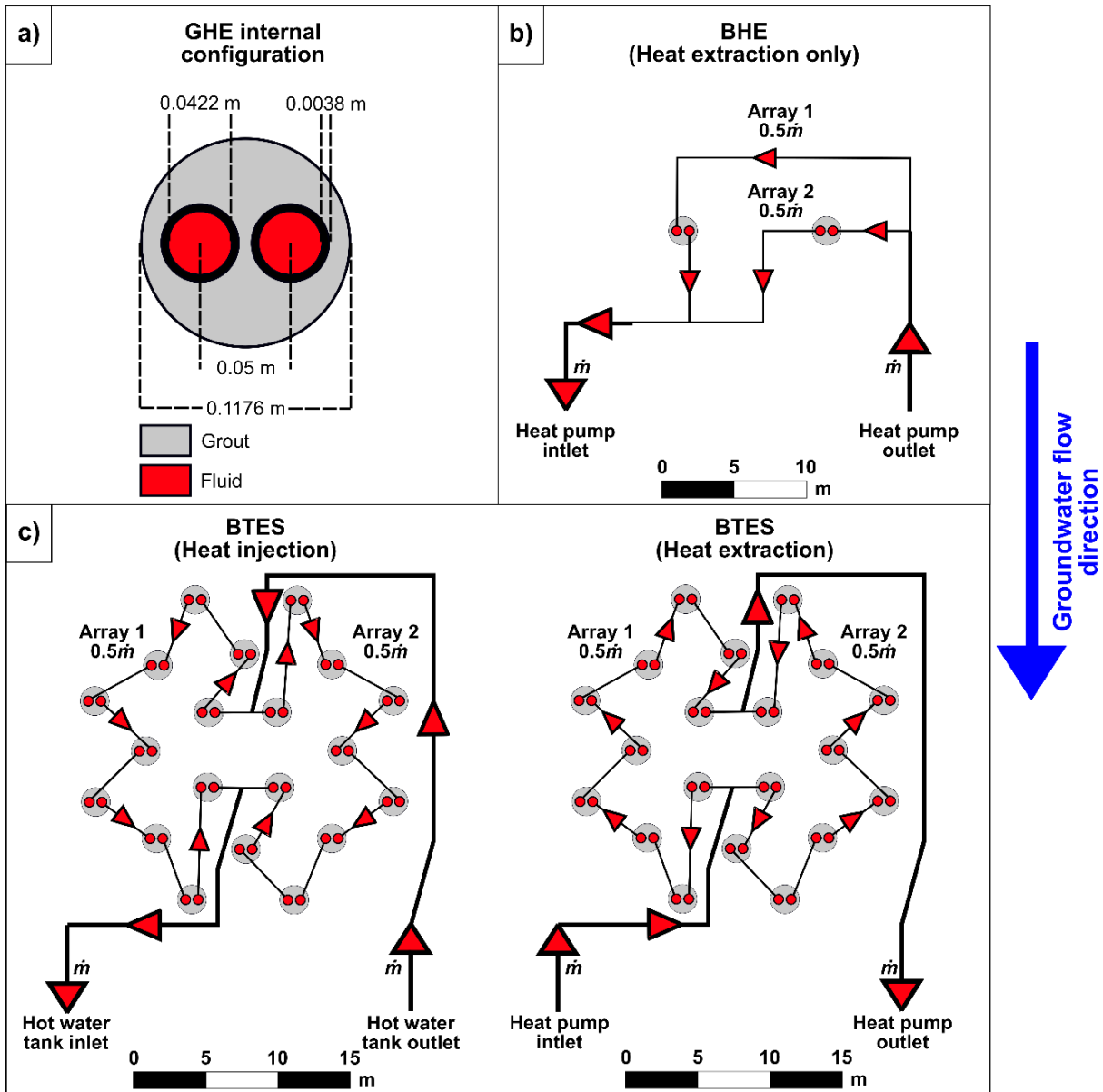


**Fig.3.4:** GHE a) internal configuration, and interconnections for b) a BHE split in two parallel arrays and c) a BTES during heat injection/extraction split in two parallel arrays. GHE proportions are exaggerated in b and c.

Operation of shallow geothermal systems in northern environment involves different heat transfer mechanisms. Conduction, advection, and water phase changes occur and needs to be integrated into numerical model calculations. The Feflow software was used to develop the numerical models from a subsurface perspective, since it combines required heat transfer mechanisms and GHE simulations (Diersch, 2014; Anbergen et al., 2015). However, heat pump operation and building energy requirements cannot be simulated directly in the software. Therfore, complementary Python scripts were developed to calculate the difference between the  $T_{HCF}$  of the hot water tank outlet and the hot water tank inlet according to the heat

load of the analyzed building (Fig.3.1) that was determined with TRNSYS simulations based on plans and occupation, a variable COP and the volumetric heat capacity of the fluid that are a function of  $T_{\text{inlet}}$ .

### 3.3.2 Fluid flow mechanisms

Groundwater flow in a 3D confined aquifer was simulated under saturated conditions. A confined aquifer was chosen for simplicity purposes and to reduce the calculation time. The general transient groundwater flow was solved numerically according to:

$$\nabla \cdot (K \nabla h) = S \frac{\partial h}{\partial t} \quad (3.1)$$

$$q = -K \nabla h \quad (3.2)$$

$$q = v\theta \quad (3.3)$$

A plug-in simulating water phase change was also used to change local ground hydraulic conductivity to consider ice formation according to the solved ground temperature (Anbergen et al., 2015).

### 3.3.3 Heat transfer mechanisms

Groundwater flow was coupled to transient heat transfer with a general 3D equation including internal heat generation  $A$ , mechanical dispersion  $\kappa$ , heat conduction and advection numerically solved according to:

$$\frac{\partial(\rho C_{\text{eff}} \Delta T)}{\partial t} + \nabla \cdot (\rho C_f \Delta T q) - \nabla \cdot ((\lambda_{\text{eff}} + \rho C_f \kappa) \cdot \nabla T) + A_{\text{eff}} = \text{Overall heat source/sink [W m}^{-3}\text{]} \quad (3.4)$$

$$\text{where } \rho C_{\text{eff}} = \rho C_s(1 - \theta) + \rho C_f \theta$$

$$\lambda_{\text{eff}} = \lambda_s(1 - \theta) + \lambda_f \theta$$

$$A_{\text{eff}} = A_s(1 - \theta) + A_f \theta$$

Internal heat transfers related to GHE were computed along liner nodes (1D) with the quasi-stationary analytical approach of Claesson (1988) implemented in Feflow and assuming a local thermal equilibrium between all specified nodes of the BHE (Diersch, 2014). Heat transfer calculations were also made with the Anbergen (2015) plug-in changing local ground thermal properties based on solved temperature to simulate the effect of water phase change.

Heat pump operation was simulated for BHE and BTES systems according to the  $T_{\text{inlet}}$  solved in Feflow.  $T_{\text{inlet}}$  is recovered before each timestep and the COP and  $\rho C_{\text{HCF}}$  are then calculated.  $T_{\text{outlet}}$  is calculated according to the HCF flowrate  $m_{\text{HCF}}$  and the heating demand  $P_{\text{HD}}$  through time:

$$T_{\text{outlet}} = T_{\text{inlet}} - \left( \frac{P_{\text{HD}}[1 \text{ kW}/1,000 \text{ W}]}{\rho C_{\text{HCF}} m_{\text{HCF}}} \right) \left( \frac{COP-1}{COP} \right) \quad (3.5)$$

BTES systems can be used to injected thermal energy in the ground. To do so,  $T_{\text{outlet}}$  is calculated as in Eq.3.5, but  $\left( \frac{COP-1}{COP} \right) = 1$  since it was considered as a direct heating system using a hot water tank and a circulating pump, and thus minimizing energy consumption without a heat pump to inject the  $P_{\text{HPV}}$ :

$$T_{\text{outlet}} = T_{\text{inlet}} - \left( \frac{P_{\text{HPV}}[1 \text{ kW}/1,000 \text{ W}]}{\rho C_{\text{HCF}} m_{\text{HCF}}} \right) \quad (3.6)$$

### 3.3.4 Domain discretization

Meshes for BHE and BTES models are refined around each GHE with six nodes according to the methodology described by Diersch (2011) having a minimal 0.1 m distance and thus ensuring numerical stability according to the GHE specifications described in Fig.3.4a. Lateral boundaries were placed such that their presence would not interfere with the thermal plume development. Vertical slices were positioned at a distance ranging from 1-2 m between two silty sand slices (high  $v$  values expected), while distance range from 1-10 m between two bedrock slices (low  $v$  values expected). Meshes were controlled and numerical errors were avoided by complying with the Peclet ( $Pe$ ) and Courant ( $Co$ ) criteria given by:

$$Pe = \frac{v\partial X}{\alpha} \leq 2 \quad (3.7)$$

$$Co = \frac{v\partial t}{\partial X} \leq \frac{Pe}{2} \quad (3.8)$$

Model dimensions of the BHE numerical model are 200 m  $\times$  200 m  $\times$  190 m in the  $x$ ,  $y$  and  $z$  directions, respectively. The mesh involved 273,999 nodes with 525,888 lateral prismatic triangular elements ranging from a maximum of 6.3 m (edge of the numerical model) to a minimum of 0.1 m (around each GHE). Vertical element dimensions are distributed within 33 slices ranging from 1 m to 10 m (Fig.3.5a). Model dimensions for both BTES numerical models have a dimension of 200 m  $\times$  200 m  $\times$  60 m in the  $x$ ,  $y$  and  $z$  directions, respectively. The mesh has 76,320 nodes with 144,210 lateral prismatic triangular elements ranging from a maximum of 12.5 m to a minimum of 0.1 m (around each GHE). Vertical element dimensions are distributed within 24 slices ranging from 1 m to 10 m (Fig.3.5b).

### 3.3.5 Input parameters

Homogeneous and isotropic hydraulic and thermal properties were considered for the silty sand and bedrock materials in numerical models. Hydraulic properties assigned in the models (Tab.3.1) were determined from the calibrated regional groundwater flow model shown in Appendix IV and from data and interpretations in CIMA+ (2014). Thermal properties assigned in the models (Tab.3.1) were determined from field and laboratory characterization shown in Appendices V and VI.

**Table 3.1 :** Hydraulic and thermal properties assigned to the numerical models.

Parameter	Value	Reference
<b>Silty Sand</b>		
Hydraulic conductivity $K$	$2.89 \cdot 10^{-4} \text{ m s}^{-1}$	Appendix IV, Géophysique GPR International inc. (2002), CIMA+ (2014)
Longitudinal dispersivity $\kappa_{\text{LO}}$	4 m	Xu and Eckstein (1995)
Transverse dispersivity $\kappa_{\text{TR}}$	0 m	-
Specific storage $S$	$9.82 \cdot 10^{-4} \text{ m}^{-1}$	Appendix IV
Porosity $\theta$	0.20	Appendix IV
Thermal conductance $l$	$20 \text{ W m}^{-2} \text{ K}^{-1}$	Appendix V
Solid thermal conductivity $\lambda_s$	$1.11 \text{ W m}^{-1} \text{ K}^{-1}$	Langevin (2022)
Fluid thermal conductivity $\lambda_f$	Time dependant	Fig.3.5
Solid volumetric heat capacity $\rho C_s$	$1.72 \text{ MJ m}^{-3} \text{ K}^{-1}$	Langevin (2022)
Fluid volumetric heat capacity $\rho C_f$	Time dependant	Fig.3.5
Solid internal heat generation $A_s$	$0 \text{ J m}^{-3} \text{ d}^{-1}$	-
Fluid internal heat generation $A_f$	Time dependant	Eqs.3.9 and 3.10, Fig.3.5
<b>Bedrock</b>		
Hydraulic conductivity $K$	$5.79 \cdot 10^{-7} \text{ m s}^{-1}$	Géophysique GPR International inc. (2002), CIMA+ (2014)
Specific storage $S$	$4.59 \cdot 10^{-5} \text{ m}^{-1}$	Appendix IV
Porosity $\theta$	0.02	Appendix IV
Longitudinal dispersivity $\alpha_{\text{LO}}$	0 m	-
Transverse dispersivity $\alpha_{\text{TR}}$	0 m	-
Thermal conductance $l$	$20 \text{ W m}^{-2} \text{ K}^{-1}$	Appendix V
Thermal conductivity $\lambda_s$	$2.67 \text{ W m}^{-1} \text{ K}^{-1}$	Appendix VI
Fluid thermal conductivity $\lambda_f$	$0.56 \text{ W m}^{-1} \text{ K}^{-1}$	-
Volumetric heat capacity $\rho C_s$	$2.29 \text{ MJ m}^{-3} \text{ K}^{-1}$	Comeau (2020)
Fluid volumetric heat capacity $\rho C_f$	$4.18 \text{ MJ m}^{-3} \text{ K}^{-1}$	-
Solid internal heat generation $A_s$	$0 \text{ J m}^{-3} \text{ d}^{-1}$	-

Fluid internal heat generation $A_f$	$0 \text{ J m}^{-3} \text{ d}^{-1}$	-
<b>GHE</b>		
Grout thermal conductivity $\lambda$	$1.50 \text{ W m}^{-1} \text{ K}^{-1}$	-
Heat carrier fluid density $\rho_{HCF}$	Temperature dependant [ $\text{kg m}^{-3}$ ]	Eq.3.11, Dowfrost (2008)
Heat carrier fluid dynamic viscosity $\mu_{HCF}$	$0.007 \text{ kg m}^{-3} \text{ s}^{-1}$	-
Heat carrier fluid flowrate at the heat pump $\dot{m}_{HCF}$	$5.0 \cdot 10^{-4} \text{ m}^{-3} \text{ s}^{-1}$	-
Heat carrier fluid thermal conductivity $\lambda_{HCF}$	$0.42 \text{ W m}^{-1} \text{ K}^{-1}$	-
Heat carrier fluid volumetric heat capacity $\rho C_{HCF}$	Temperature dependant [ $\text{MJ m}^{-3} \text{ K}^{-1}$ ]	Eq.3.12, Dowfrost (2008)
Pipe thermal conductivity $\lambda$	$0.70 \text{ W m}^{-1} \text{ K}^{-1}$	-

The  $\kappa_{LO}$  value in the silty sand was estimated from the Xu and Eckstein (1995) equation since there is no data available for unconsolidated sediments in Whapmagoostui-Kuujjuarapik. The  $\kappa_{TR}$  value used in the simulations was an order of magnitude less than  $\kappa_L$ . No mechanical dispersivities ( $\kappa_{LO}$  and  $\kappa_{TR}$ ) were considered for the bedrock material because its primary and secondary porosity are small, and fractures are assumed poorly connected. It should be noted that for these relatively small-scale simulations, the process of mechanical dispersion is less important compared to thermal diffusion, so the heat transport process is only weakly affected by the choice of the above values. However, hydrodynamic dispersion may become more important at larger scales.

The effect of groundwater recharge periods on thermal properties was considered by varying  $\lambda_f$  and  $\rho C_f$  through time with the plug-in described in Anbergen (2015). The thermal properties values of the ground fluid were determined with an arithmetic mean between air ( $\lambda_f = 0.02 \text{ W m}^{-1} \text{ K}^{-1}$ ,  $\rho C_f = 1.20 \text{ kJ m}^{-3} \text{ K}^{-1}$ ) and water ( $\lambda_f = 0.56 \text{ W m}^{-1} \text{ K}^{-1}$ ,  $\rho C_f = 4.18 \text{ MJ m}^{-3} \text{ K}^{-1}$ ).  $\lambda_f$  ( $0.56 \text{ W m}^{-1} \text{ K}^{-1}$ ) and  $\rho C_f$  ( $4.18 \text{ MJ m}^{-3} \text{ K}^{-1}$ ) at 100% water content was considered for groundwater recharge periods, while  $\lambda_f$  ( $0.18 \text{ W m}^{-1} \text{ K}^{-1}$ ) and  $\rho C_f$  ( $1.25 \text{ MJ m}^{-3} \text{ K}^{-1}$ ) at 30% water content were considered for the rest of the year (Fig.3.5).  $\rho C_f$  values were promptly shifted and substantial thermal energy gain or loss were consequently introduced since the internal energy in the domain is proportional to its heat capacity. To address this issue, an internal heat generation  $A$  ( $\text{J m}^{-3} \text{ d}^{-1}$ ) was applied to the ground fluid during one timestep (0.1 d) in silty sand elements according to Eqs.3.9 and 3.10, while  $A$  was set to  $0 \text{ J m}^{-3} \text{ d}^{-1}$  otherwise.

$$A_{f_1} = (\rho C_{f_2} - \rho C_{f_1})\partial t = 293,000 \text{ J m}^{-3}\text{d}^{-1} \quad (3.9)$$

$$A_{f_2} = (\rho C_{f_1} - \rho C_{f_2})\partial t = -293,000 \text{ J m}^{-3}\text{d}^{-1} \quad (3.10)$$

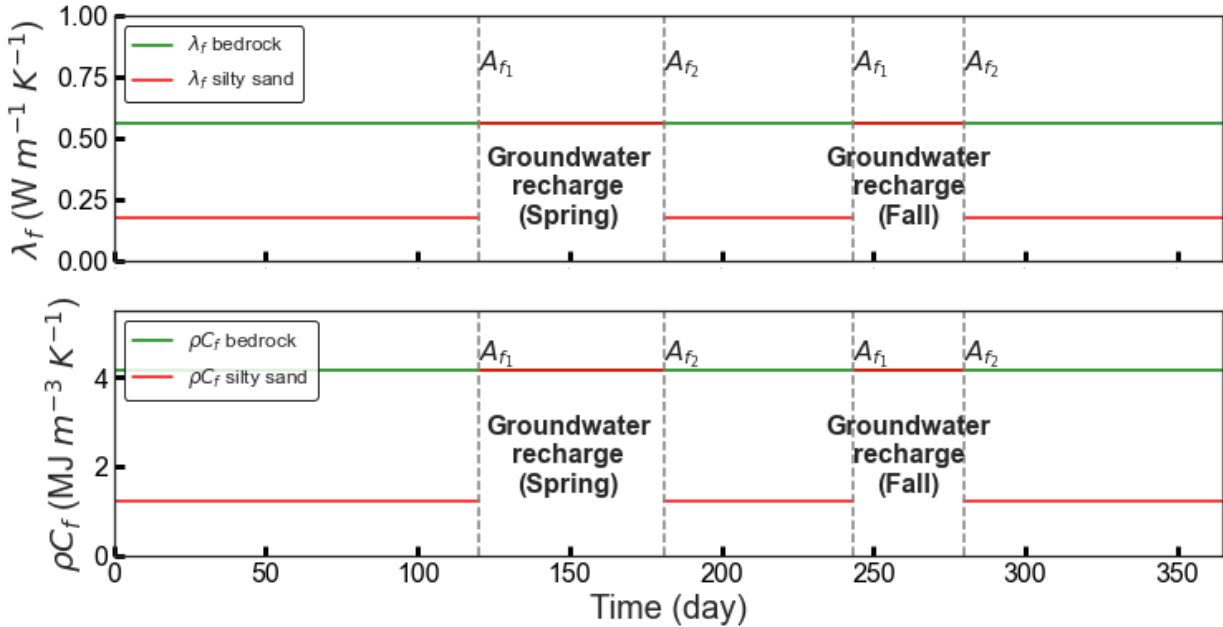


**Fig.3.5:** Thermal properties variations used during a year to represent groundwater recharge periods in numerical models for the silty sand material.

Density and volumetric heat capacity for a 30% concentration of propylene glycol water mixture (Dowfrost, 2008) were interpolated and are presented in Eqs.3.11 and 3.12, respectively. These properties were used for the heat pump heat transfer calculation (Eqs.3.5 and 3.6) and for the GHE thermal resistance calculation, which was solved with the Eskilson and Claesson quasi-stationary analytical approach integrated in Feflow (Diersch, 2014). Specifications from a COMP and an ABS were integrated into Python scripts to determine temperature dependant COP equations that were used to estimate  $T_{\text{outlet}}$  (Eq.3.6). The 038 model from Geosmart Energy (Geosmart, 2013) was considered to simulate COMP (Eq.3.13), while the LB model from Robur (fuelled by natural gas) was considered for the ABS (Robur, 2014; Eq.3.14) assuming that a heat pump supplied by diesel would have a similar performance curve and its specifications are the same as described in the technical document. The  $\dot{m}_{\text{HCF}}$  at the heat pump was maintained constant at  $5.0 \times 10^{-4} \text{ m}^3 \text{s}^{-1}$  (Tab.3.1) based on the recommendations of the manufacturer minimal operational  $\dot{m}_{\text{HCF}}$  of  $5.0 \times 10^{-4} \text{ m}^3 \text{s}^{-1}$  when the  $T_{\text{inlet}}$  is as low as  $-6.7^\circ\text{C}$ . Thus, the flowrate calculated in each parallel GHE array for BHE and BTES is  $2.5 \times 10^{-4} \text{ m}^3 \text{s}^{-1}$ .

$$\rho_{\text{HCF}} = 1047.49 - 0.35T - 0.23 \times 10^{-2}T^2 - 0.33 \times 10^{-5}T^3 \quad (3.11)$$

$$\rho C_{\text{HCF}} = 3.97 + 0.16 \times 10^{-2}T - 0.11 \times 10^{-4}T^2 + 0.12 \times 10^{-7}T^3 \quad (3.12)$$

$$COP_{COMP} = 2.648 + 8.419 \times 10^{-2}T + 1.257 \times 10^{-3}T^2 - 1.060 \times 10^{-4}T^3 + 1.725 \times 10^{-6}T^4 \quad (3.13)$$

$$COP_{ABS} = 1.202 + 9.045 \times 10^{-3}T - 3.671 \times 10^{-4}T^2 + 5.333 \times 10^{-6}T^3 \quad (3.14)$$

where  $T$  is in °C

Hourly building load profile of a house at the CEN station in Whapmagoostui-Kuujjuarapik was estimated with simulations in TRNSYS (Maranghi et al., 2022). The simulations were performed according to building plans and occupation, and then calibrated with 2018-2019 fuel oil and electricity bills. However, these simulations did not include domestic hot water production. This 8.5 m × 11.1 m single-floor building has a crawlspace, seven standard double-glazed windows, two doors, standard light bulb lighting, occupancy of one individual and air pulse heating with a fuel oil furnace. The annual heating consumption intensity is 360 kWh m<sup>-2</sup> yr<sup>-1</sup>,  $P_{HD}$  range from 0.0 to 10.8 kW and an annual average heating demand of 4.5 kW was estimated based on TRNSYS simulations (Fig.3.6). Technical reports of the selected COMP specified a maximal heating capacity of ≈9 kW and thus, it cannot cover the whole heating demand. A fuel oil furnace (commonly used in these communities) covered arbitrarily 20% of the peak  $P_{HD}$  value in order to partly provide the heating load uncovered by the heat pump. This study considered that the geothermal system covered 80% ( $P_{HDI}$ ) of the  $P_{HD}$  and a diesel furnace covered 20% ( $P_{HDI2}$ ) of  $P_{HD}$ .  $P_{HDI}$  was used in Eq.3.6 to estimate  $T_{outlet}$  and selected to extract thermal energy from the BHE numerical model through discretized GHE (Fig.3.6). BTES models used the same thermal energy profile, but thermal energy from numerical models was only extracted from 0 to 120 days and from 244 to 365 days (Fig.3.6b) to allow heat injection when the solar radiation is at its peak. No thermal energy is extracted from the ground from 120 to 244 days and the fuel oil furnace covers the total heating demand since the BTES is used to inject heat in the ground (Fig.3.6b).

The electricity production of the PV solar panels was calculated with PVGIS (2022) based on a nominal solar panel electricity production efficiency of 14% (standard crystalline silicon panel) and a power loss of 5% due to the angle of incidence of solar radiation related to dip and orientation of the solar panels at the CEN station. This estimation was used to calculate the potential electricity power at each time step according to the daily solar radiation data recorded at the CEN's meteorological station from 2005 to 2016 (CEN, 2017).

This potential electricity energy was either electrically stored in batteries or thermally stored in a hot water tank. A representative -40% power losses related to electricity storage was selected based on a maximum power point tracking (MPPT) regulator (-10%) and an inverter (-5%), lead acid batteries efficiency of 85% (-15%) and a capacity loss of batteries due to low temperature operation (-10%). These energy losses were subtracted to this potential electricity power to calculate the  $P_{EPV}$ . The  $P_{EPV}$  was used to

partly provide electricity to COMP or ABS, the diesel furnace electronics and other electrical appurtenances for BHE and BTES models.  $P_{TP}$  covers remaining electricity needs if  $P_{EPV}$  have insufficient capacity to provide the devices.

Fuel oil furnaces and ABS usually satisfy a heating demand and consume few electricity, but the maximal calculated  $P_{EPV}$  with the PV panels available ( $336 \text{ m}^2$ ) produce more electricity than necessary for these devices. The electricity production in the communities of Nunavik is a critical issue and the comparison of the  $P_{EPV}$  under different PV area is needed to properly compare the performance of the diesel furnaces, COMP and ABS.  $P_{EPV}$  was calculated for eight different PV areas ranging from 0 to  $336 \text{ m}^2$  with constant steps of  $48 \text{ m}^2$  (PV area available per building) to supply electricity needs of BHE (Fig.3.6a). The direction of the PV panels ranges from  $140$  to  $245^\circ\text{N}$  while their inclination is mainly at  $18^\circ$  (Fig.3.1).

BTES requires a large PV area to inject sufficient energy and increase the ground temperature in winter to enhance heat pump efficiency. According to a simplified transient equation characterizing thermal energy balance of a ground thermal storage (Eq.3.15), using a small area of PV (e.g.,  $48 \text{ m}^2$ ) would induce a very small increase of  $\Delta T$  which would not be sufficient to enhance significantly the heat pump efficiency. However, the maximal area of solar panels ( $336 \text{ m}^2$ ) has the potential to increase by seven times  $\Delta T$  and inject more thermal energy to the ground. In the rest of this work, the  $P_{HPV}$  yearly profile describing the heat rate to inject into the ground for BTES numerical models was only estimated with a  $336 \text{ m}^2$  PV area as fewer PV area would not be reasonable for BTES purposes.

$$\Delta T [\text{ }^\circ\text{C}] = \frac{-P_{HPV} t}{Volume_{storage} \rho C_{storage}} \quad (3.15)$$

The potential electricity power produced with  $336 \text{ m}^2$  of solar panels was assumed to be converted into heat from 120 to 244 days using direct heating with a 100% efficiency in a hot water tank for the BTES scenarios. A representative 20% heat loss due to tank storage and HCF circulation to the BTES and electricity consumption related to diesel furnace electronics and pump circulation was subtracted from the potential electricity power to determine the resulting  $P_{HPV}$  used in Eq.3.6.  $P_{HPV}$  provided thermal energy to the BTES numerical models through discretized GHE from 120 to 244 days (red line in Fig.3.6b). For the rest of the year, all the remaining of the potential electricity power of the eight different PV areas investigated is stored in batteries only ( $P_{EPV}$ ) and electricity available is used to supply electricity needs of BTES (Fig.3.6b). A diagram showing the extraction and injection of thermal and electrical energy in the operation of BHE and BTES models is summarized in Fig.3.6. Energy profiles shown in Fig.3.6 were interpolated based on daily values. This induced a smoothing of heating or solar radiation high or low peaks encountered at different time of the day.

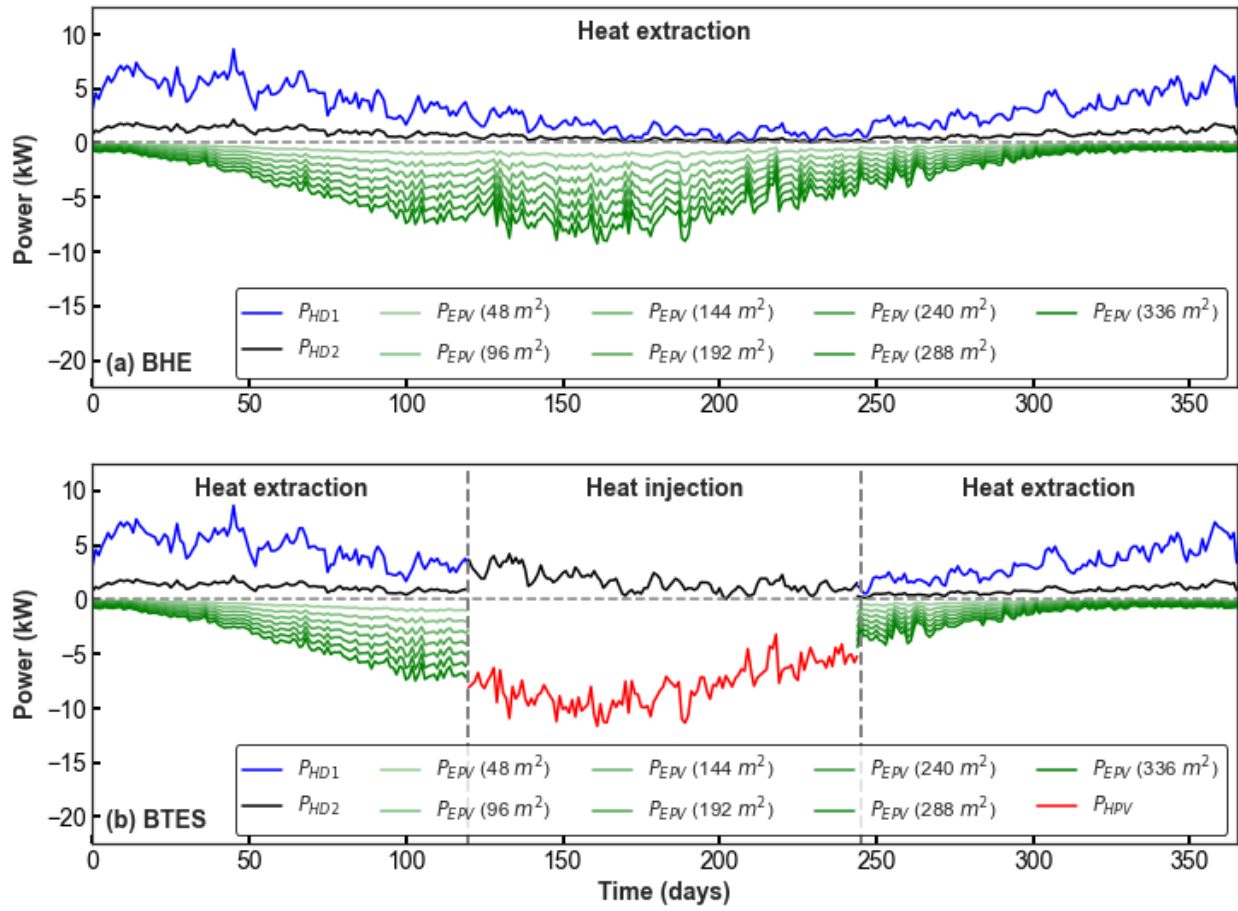
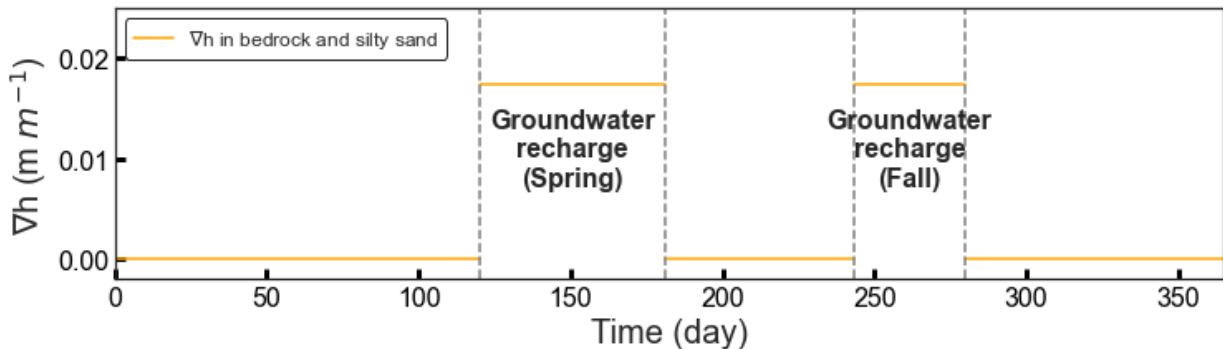


**Fig.3.6:** Yearly energy profile of heat extraction/injection scenarios for a) BHE and b) BTES models providing heat to one building where  $P_{HD1}$  (blue line) represents 80% of the total heating demand provided by a heat pump,  $P_{HD2}$  (blue line) represents 20% of the total heating demand provided by a backup diesel furnace,  $P_{EPV}$  (green lines) represents the PV electricity production available according to different solar panels area and  $P_{HPV}$  (red line) represents the thermal energy injected to the ground for BTES numerical models. By convention, energy models' inflows are considered negative.

### 3.3.6 Models boundary conditions

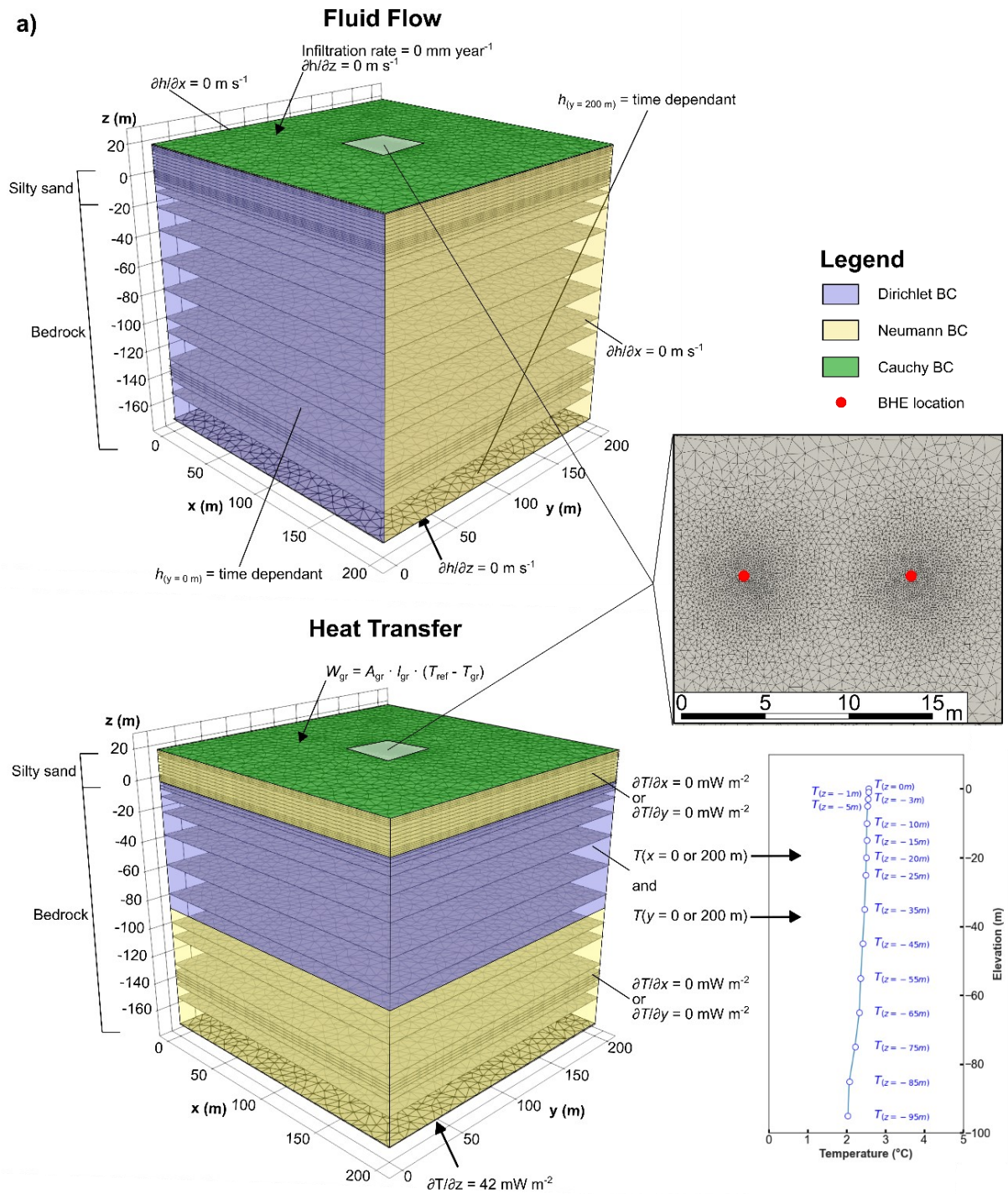
Dirichlet fluid flow boundary condition (BC) was varied through time at  $y = 0$  and 200 m in order to induce a representative groundwater flow at the CEN building location during recharge periods for BHE and BTES models (Fig.3.7). No infiltration rate was applied at the top of the models. Impermeable Neumann BC ( $0 \text{ m s}^{-1}$ ) were imposed at  $z = -170 \text{ m}$  for the BHE model and at  $z = -40 \text{ m}$  for BTES models. Symmetric Neumann BC ( $0 \text{ m s}^{-1}$ ) were set at  $x = 0$  and 200 m for all numerical models. The temperature profile of well TF05-07 recorded during the field campaign shows active groundwater flow from  $z = 0$  to -95 m. Therefore, heat transfer Dirichlet BC were set all around the BHE model from  $z = 0$  to -95 m with  $T$  values

varying with depth corresponding to this temperature profile (Fig.3.8a) to better represents the simulated temperature along the numerical model and controlled lateral groundwater flow temperature. A Neumann BC representing a regional heat flux value of  $42 \text{ mW m}^{-2}$  was considered reasonable to set at  $z = -170 \text{ m}$  in the BHE model, representing a typical regional thermal gradient. Guillou-Frottier (1995) and Comeau (2017) listed regional heat flow values of the Superior province ranging from  $20$  to  $58 \text{ mW m}^{-2}$ . This heat flux value has little influence on the results (e.g.  $0.5 \text{ }^{\circ}\text{C}$  difference at the bottom of the model with  $\pm 10 \text{ mW m}^{-2}$ ) since it characterizes only the thermal gradient at the bottom of the numerical model from  $z = -95$  to  $-170 \text{ m}$ . A Dirichlet BC in BTES models of  $T = 2.5 \text{ }^{\circ}\text{C}$  set at  $z = -40 \text{ m}$  corresponds to the TF05-07 temperature profile at  $60 \text{ m}$  depth below surface. Cauchy BC was set at the top of BHE and BTES numerical models to control inflow/outflow of heat ( $W_{\text{gr}}$ ) according to the yearly temperature profile  $T_{\text{ref}}$  described in Fig.V.1 (Appendix V). Other boundaries in the models were considered adiabatic ( $0 \text{ mW m}^{-2}$ ). GHE in the BHE model were implemented from  $z = 18$  to  $-132 \text{ m}$  at  $x_1, y_1 = (90, 100)$  and  $x_2, y_2 = (110, 100)$  (Fig.3.8a), while 20 GHE, approximately separated by  $5 \text{ m}$  in the BTES models were implemented from  $z = 18$  to  $3 \text{ m}$  (Fig.3.8b).



**Fig.3.7:** Hydraulic gradient variations used during a year to represent groundwater recharge periods in numerical models.

a)



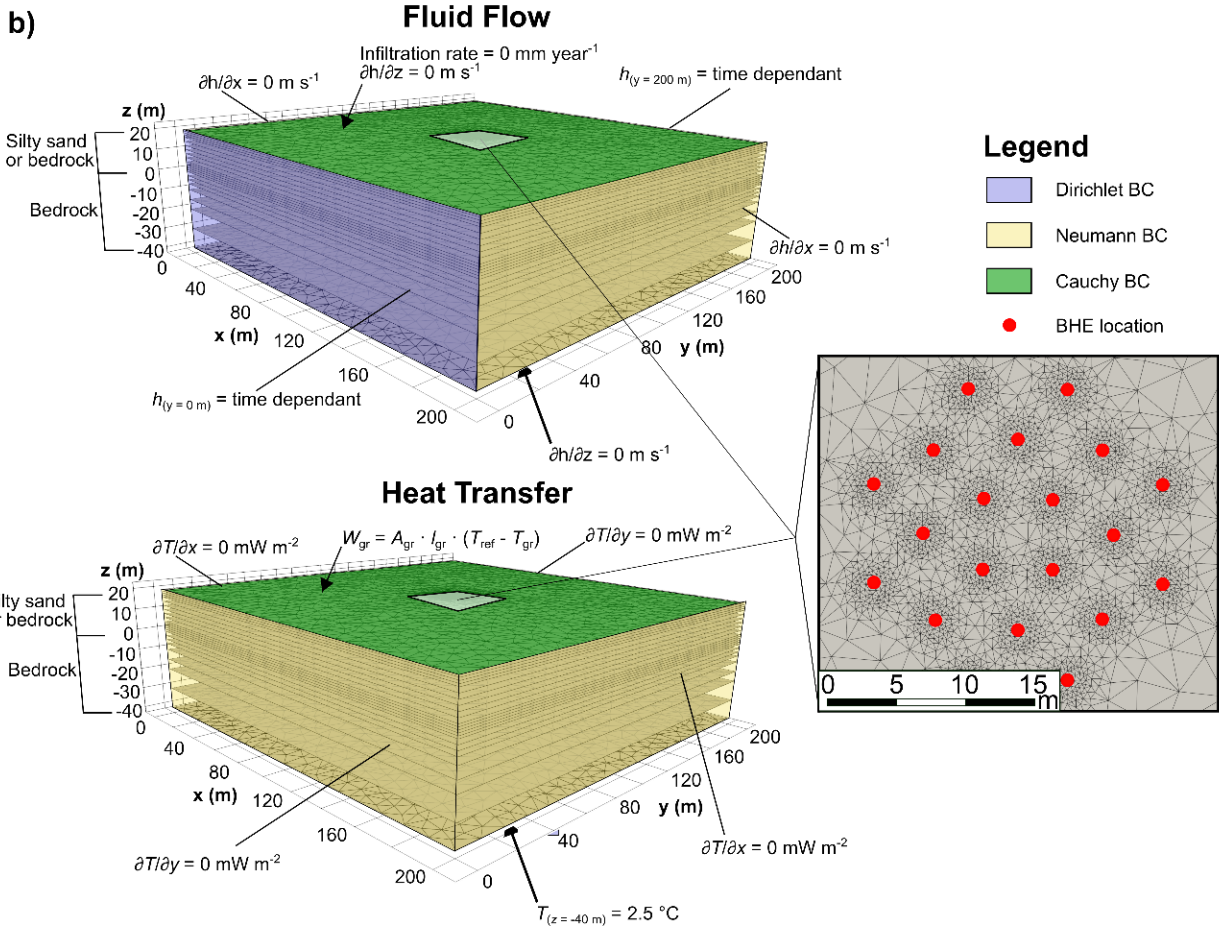


**Fig.3.8:** Discretized numerical models for the a) BHE case and b) BTES cases.

### 3.3.7 Initial conditions and simulation procedure

The initial flow and temperature conditions prior to the heat pump simulations were simulated for a two-year period without thermal extraction or injection from GHE. This procedure was used for both BHE and BTES models because seasonal temperature variations for shallow geothermal systems can have a significant thermal impact in the uppermost part of the ground, particularly for BTES systems with shallow GHE (Fig.3.9). All simulations were made for a 20-year period with a 2.4 h timestep. Numerical solution typically converged within one to three iterations depending on groundwater flow velocities.

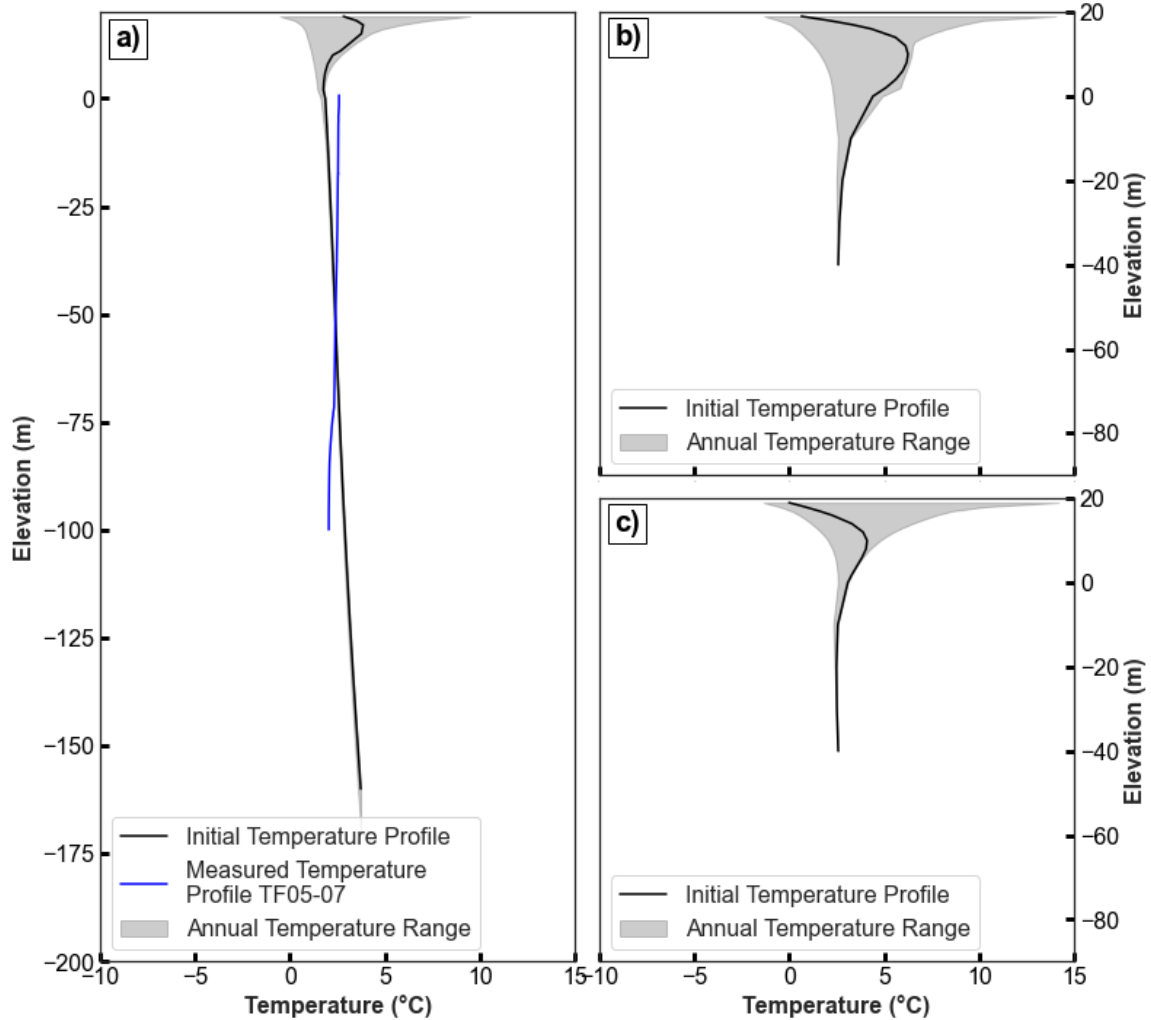


**Fig.3.9:** Initial temperature profile obtained after a two-year simulation for the a) BHE, b) BTES installed in silty sand and c) BTES installed in bedrock numerical models.

Both BHE and BTES simulations were performed to provide heat to one building with a heat pump ( $1 \times P_{HD1}$ ) and with a backup diesel furnace ( $1 \times P_{HD2}$ ). However, since BTES are commonly designed to supply a higher heat demand than that provided to a single residential building, simulations were also performed to provide heat for two buildings coupled with two heat pumps ( $2 \times P_{HD1}$ ) and two backup diesel furnaces ( $2 \times P_{HD2}$ ), while keeping the same GHE length (i.e., 300 m). Three numerical models were developed to simulate BHE and BTES geothermal systems as described in the above sections (Fig.3.3). Simulations were made for each numerical model with two different HP (COMP and ABS). In total, 12 scenarios were compared to a base case scenario where a diesel furnace provides all heating requirements for one and two buildings (Fig.3.10). The energy consumption and costs described in section 3.3.8 for each scenario was evaluated according to different  $P_{EPV}$  ranging from 0 to 336 m<sup>2</sup> with constant steps of 48 m<sup>2</sup> (room available on one building's roof).

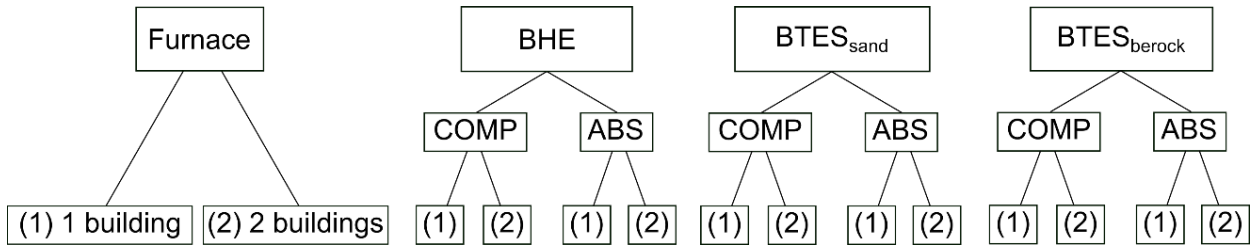


**Fig.3.10:** Simulated scenarios.

### 3.3.8 Energy consumption and costs

It is important to distinguish the energy source powering the heating equipment since there is a clear efficiency contrast between a thermal power plant (34% efficiency) and a conventional furnace (80% efficiency; Natural Resources Canada, 2012). The energy consumed by heat pumps and oil furnaces  $D_{\text{HSYS}}$  were compiled for each timestep for the simulated heating systems. The energy consumption calculations of this study consider that 1 L of diesel has a calorific value of 38.2 MJ and 1.0 kWh of electricity has 3.6 MJ (Natural Resources Canada, 2012). The ABS consumes electricity only to activate electronics and a pump (0.4 kW) to circulate the HCF. Diesel is directly consumed to power the thermal compressor of the ABS while COMP is only powered by electricity. Electricity consumption of COMP and auxiliary devices, such as furnaces (0.3 kW) and pumps (0.4 kW), were cumulated to estimate the electricity consumption of the heating systems  $P_{\text{HSYS}}$ .  $P_{\text{EPV}}$  was used to provide electricity for the  $P_{\text{HSYS}}$  and if there was not enough power from PV panels,  $P_{\text{TP}}$  was considered to cover energy needs.  $P_{\text{TP}}$  is cumulated for each day and then converted to the amount of diesel consumed by the power plant to produce this electricity ( $D_{\text{TP}}$ ; Fig.3.10).

The calculated  $D_{\text{HSYS}}$  is multiplied by a diesel price of 1.59 \$CAN L<sup>-1</sup> after subsidy (REQ, 2022) to estimate the cost of diesel paid for a heating system by a customer. The societal cost of diesel is also calculated using a 1.99 \$CAN L<sup>-1</sup> diesel price before subsidy considering a 0.40 \$CAN L<sup>-1</sup> subsidy discount (Kativik, 2022). The total diesel consumed  $D_{\text{total}}$  is calculated adding  $D_{\text{HSYS}}$  and  $D_{\text{TP}}$  and the equivalent CO<sub>2</sub> emissions is calculated according to  $D_{\text{total}}$  considering that 1 L of burned diesel produces  $2.94 \times 10^{-3}$  ton of CO<sub>2</sub> emissions (Compensation CO<sub>2</sub> Québec, 2022). The  $P_{\text{TP}}$  is also multiplied by the DN rate for domestic usage of electricity provided by Hydro-Québec north of the 53<sup>rd</sup> parallel (Hydro-Québec, 2022) to estimate electricity cost paid by a customer. Households typically use between 15 to 22 kWh d<sup>-1</sup> of electricity for daily operation (Hydro-Québec, 2022) but a total of 40 kWh d<sup>-1</sup> is available for each residential building at 0.06 \$CAN kWh<sup>-1</sup> (1<sup>st</sup> tier) and then electricity is paid at a rate of 0.43 \$CAN kWh<sup>-1</sup> (2<sup>nd</sup> tier). This study considers that 22 kWh d<sup>-1</sup> building<sup>-1</sup> is available for a heating system and paid at the 1<sup>st</sup> tier rate (i.e., 18 kWh d<sup>-1</sup> is used for end-uses other than heating by the household, leaving 40–18 kWh d<sup>-1</sup> for heating in the first tier) while the rest of  $P_{\text{TP}}$  exceeding 22 kWh d<sup>-1</sup> building<sup>-1</sup> is paid at the 2<sup>nd</sup> tier rate. The electricity cost paid by a customer is added to diesel cost paid by a customer to determine  $\text{Cost}_{\text{HSYS customer}}$ . The societal

electricity cost at WK is considered at  $0.70 \text{ $CAN kWh}^{-1}$  (Karanasios and Parker, 2016) and it is added to the societal cost of diesel to estimate  $\text{Cost}_{\text{HSYS societal}}$  (Fig.3.11).

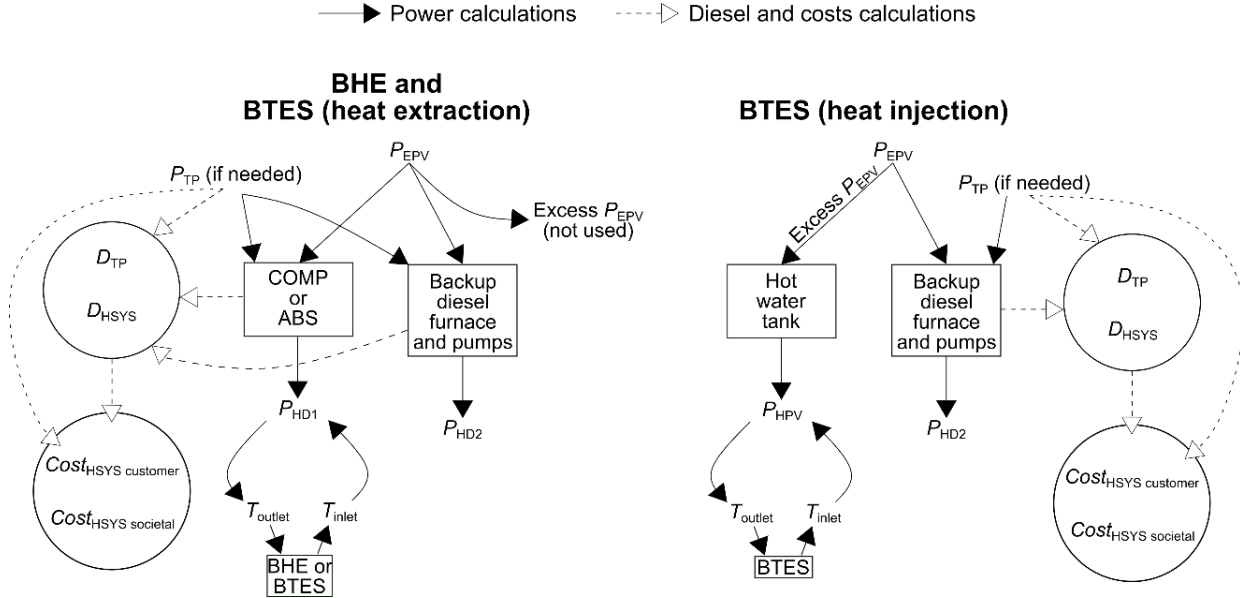


**Fig.3.11:** Scheme of the energy consumption and costs calculations for the numerical models.

## 3.4. Results

### 3.4.1 Simulated geothermal systems

Figure 3.12 shows the simulated temperature profiles along the  $z$  axis at 0 (initial condition), 6,980 (midwinter 20<sup>th</sup> year), and 7,160 days (midsummer 20<sup>th</sup> year) for BHE (Fig.3.12a and b), BTES<sub>sand</sub> (Fig.3.12c and d) and BTES<sub>bedrock</sub> (Fig.3.12e and f) scenarios. Results show that the shallower subsurface (where BTES are installed) mainly follows seasonal temperature and groundwater variations regardless of the heat extraction for BHE and BTES<sub>sand</sub> scenarios. On the other hand, ground  $T$  is increased by heat injection for scenario BTES<sub>bedrock</sub> compared to the other scenarios. In the lower part of the BHE model, where GHE extract energy from  $z = -132$  to 18 m, a lower ground  $T$  is annually observed compared to the initial temperature profile. The simulated temperature from  $z = -130$  to -10 m of the BHE<sub>COMP-2</sub> scenario at 7,160 days is also lower than at 6,980 days, which suggests that ground  $T$  between the two GHE of 150 m length decreased after 20 years of operation.

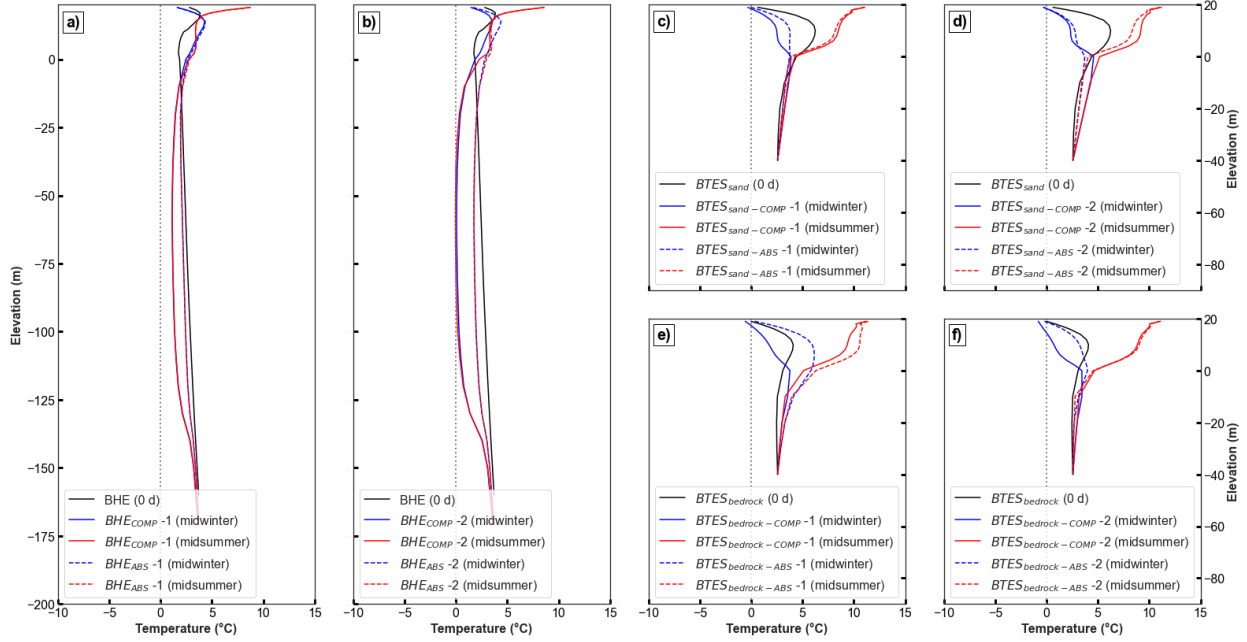
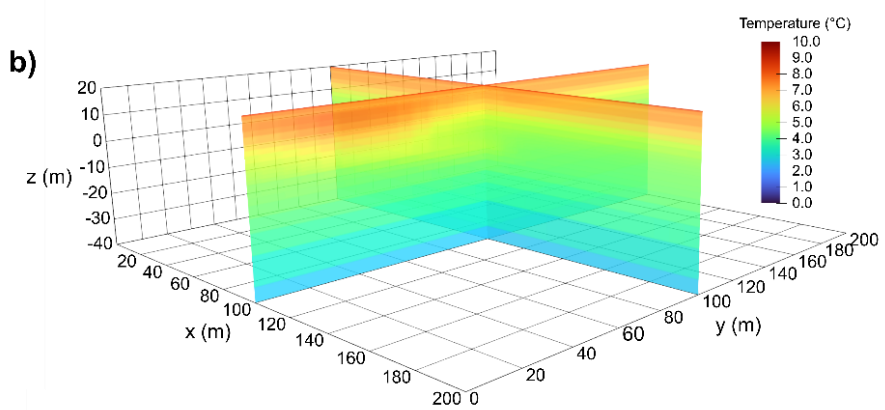
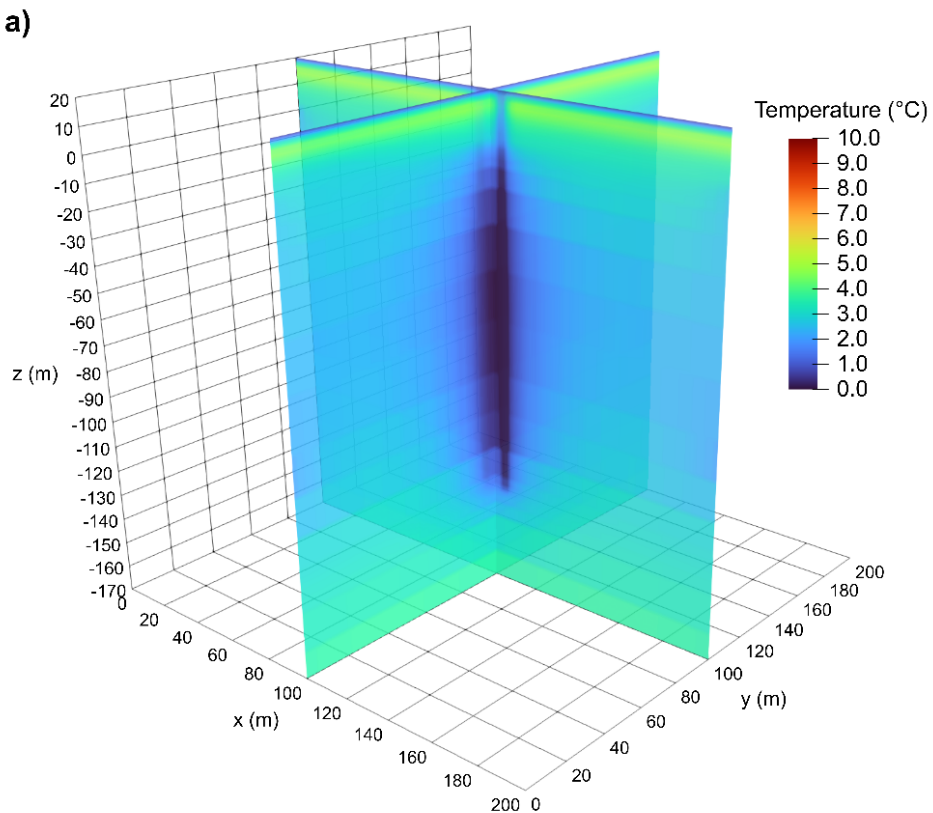


**Fig.3.12:** Temperature profiles at the center of the numerical models during midwinter after 6,980 days of operation (blue lines) and midsummer after 7,160 days of operation (red lines) for BHE (a, b), BTES<sub>sand</sub> (c, d) and BTES<sub>bedrock</sub> (e, f) scenarios.

Significant groundwater flow velocities during groundwater recharge periods also affected ground  $T$  in the silty sand material but not in the bedrock material. Heat extraction perturbations after 7,200 days (20 days under  $\nabla h = 0.0175 \text{ m m}^{-1}$ ) around the BHE's GHE were thermally washed from  $z = 0$  to 20 m while the region below that was not affected by groundwater recharge periods (Fig.3.13a). Heat injection simulated for a BTES<sub>sand</sub> is also thermally washed and the thermal plume is not recoverable by the GHE (Fig.3.13b). Ground  $T$  in the vicinity of the GHE increases during summer when the heat pump is coupled to a BTES<sub>bedrock</sub> and thermal storage is efficient even under  $\nabla h = 0.0175 \text{ m m}^{-1}$  (Fig.3.13c).

The silty sand material has a high permeability compared to the bedrock material. The main groundwater recharge periods (spring and fall) induce significant groundwater velocities in the silty sand layer. These periods are correlated to thermal perturbation washing in the vicinity of GHE. According to the operation and type of GHE, this thermal washing can either be beneficial or unfavorable: BHE continuously extract ground thermal energy to provide heat to a building. High groundwater velocities bring new thermal energy in silty sand and enhance heat pump efficiency according to the effective area of GHE exposed to the advective front. However, BHE simulations show a low influence of groundwater advection on heat pump efficiency since the silty sand material only represents 40 m (13%) on the total 300 m GHE length simulated (Fig.3.13a). Ice formation and unbalanced heat loads contribute to low ground  $T$  around the GHE in bedrock and ground  $T$  can remain below 0 °C permanently. BTES alternatively have small

thermal losses due to advective heat transfer when installed in a low permeable medium such as the bedrock, since advective heat transfer is negligible (Fig.3.13c). BTES installed in more permeable materials, such as silty sands and under a significant  $\nabla h$ , can experience significant heat losses (Fig.3.13b). Due to the groundwater recharge periods simulated in the fall, heat injection originating from PV solar panels during summer is mainly wasted. This PV electricity production is a critical issue to address in communities of Nunavik to limit the consumption of  $P_{TP}$ . To this regard, results suggest that BTES should not be installed in permeable materials such as silty sand, or materials with more permeability.



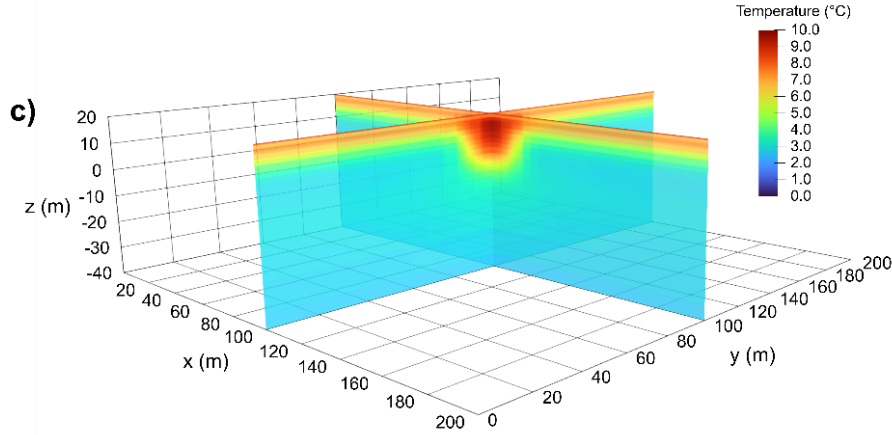


**Fig.3.13:** Ground temperature in fall after 7,200 days of operation (20 days under a groundwater recharge period with  $\nabla h = 0.0175 \text{ m m}^{-1}$ ) for the BHE (a), BTES<sub>sand</sub> (b) and BTES<sub>bedrock</sub> (c) scenarios.

### 3.4.2 Comparison between scenarios

ABS scenarios revealed a COP ranging from 1.2 to 1.3 where  $T_{\text{inlet}}$  ranged from 0.1 to 21.7 °C to provide the heating demand of a single residential building. In the case of two residential buildings, the COP ranges from 1.2 to 1.3 and  $T_{\text{inlet}}$  from -1.9 to 21.7 °C. In the single-building scenario, COMP exhibited a COP ranging from 2.3 to 3.7, where  $T_{\text{inlet}}$  ranged from -5.1 to 21.9 °C. COP and  $T_{\text{inlet}}$  range from 2.0 to 3.7 and from -11.6 to 22.4 °C, respectively, in the two-building scenario. Due to the high COP value of COMP, the heating demand is mainly provided by the ground and lower amount of energy is consumed compared to ABS. At their highest efficiency, simulations of COMP coupled with a BHE and a BTES revealed a COP  $\approx 2.8$  and 3.7, respectively. The efficiency of COMP decreases during maximal heating demand periods in winter with a COP of around 2.0 to 2.5 for both BHE and BTES scenarios (Fig.3.14b). The BHE<sub>COMP-2</sub> and BTES<sub>sand-COMP-2</sub> scenarios both simulated a  $T_{\text{inlet}} < -6.7$  °C during high heating demand periods (winter), totalizing 28% of time over the 20-year simulation where a commercial heat pump is expected to stop to prevent internal damage.

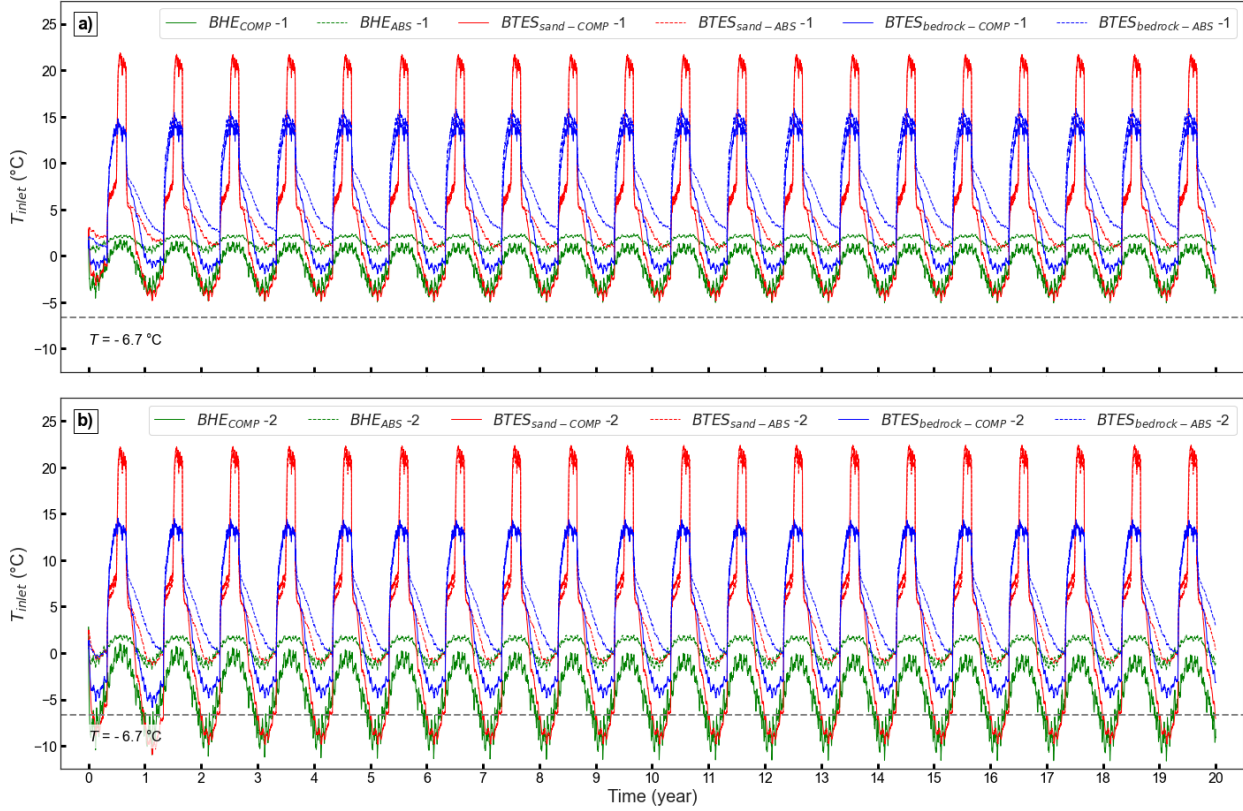


**Fig.3.14:** Simulated temperature at the ground source heat pump inlet for the scenarios providing the heating demand of a) one building and b) two buildings.

The 300 m GHE length imposed to the simulated scenarios is not ideally sized for all type of system. The 300 m GHE length is oversized for all ABS scenarios and the BTES<sub>bedrock-COMP-2</sub> since  $T_{\text{inlet}}$  did not reach the operational heat pump limit of  $-6.7^\circ\text{C}$  and can be considered to have an excessive safety factor (Fig.3.14). On the other hand, the BHE<sub>COMP-2</sub> and BTES<sub>sand-COMP-2</sub> scenarios would need  $\approx 600$  m of GHE since a  $T_{\text{inlet}} < -6.7^\circ\text{C}$  was recorded for 28% of the 20-year period and both simulated a minimal  $T_{\text{inlet}} < -11^\circ\text{C}$  (Fig.3.14b). However, the GHE length for other COMP scenarios was reasonably sized (Fig.3.14).

The  $P_{\text{TP}}$  needs for the ABS, Furnace-1 and Furnace-2 scenarios are small and it can be wholly covered using PV area  $< 48 \text{ m}^2$  (Fig.3.15a and b). COMP scenarios use more  $P_{\text{TP}}$  and the amount of electricity covered by PV increases with the number of PV panels used as expected but even the largest PV area =  $336 \text{ m}^2$  cannot cover entirely the  $P_{\text{TP}}$  needs. The  $P_{\text{TP}}$  covered by PV rate decreases by increasing the PV area (Fig.3.15a and b) since winter remains the highest  $P_{\text{TP}}$  needs period while it is the opposite for the PV production. However, increasing the PV area in the scenarios including a COMP can significantly decrease the average  $P_{\text{TP}}$  (Fig.3.15c and d), which leads to CO<sub>2</sub> emissions reduction, and  $\text{Cost}_{\text{HSYS customer}}$  and  $\text{Cost}_{\text{HSYS societal}}$  savings. It should be noted that the percentage of  $P_{\text{TP}}$  covered by PV for the BTES scenarios is  $> 0\%$  (Fig.3.15a and b). As described in the procedure to determine  $P_{\text{HPV}}$  in section 3.3.5, electricity needs

were covered during the heat injection period since PV is already used and it would not make sense to avoid using it.

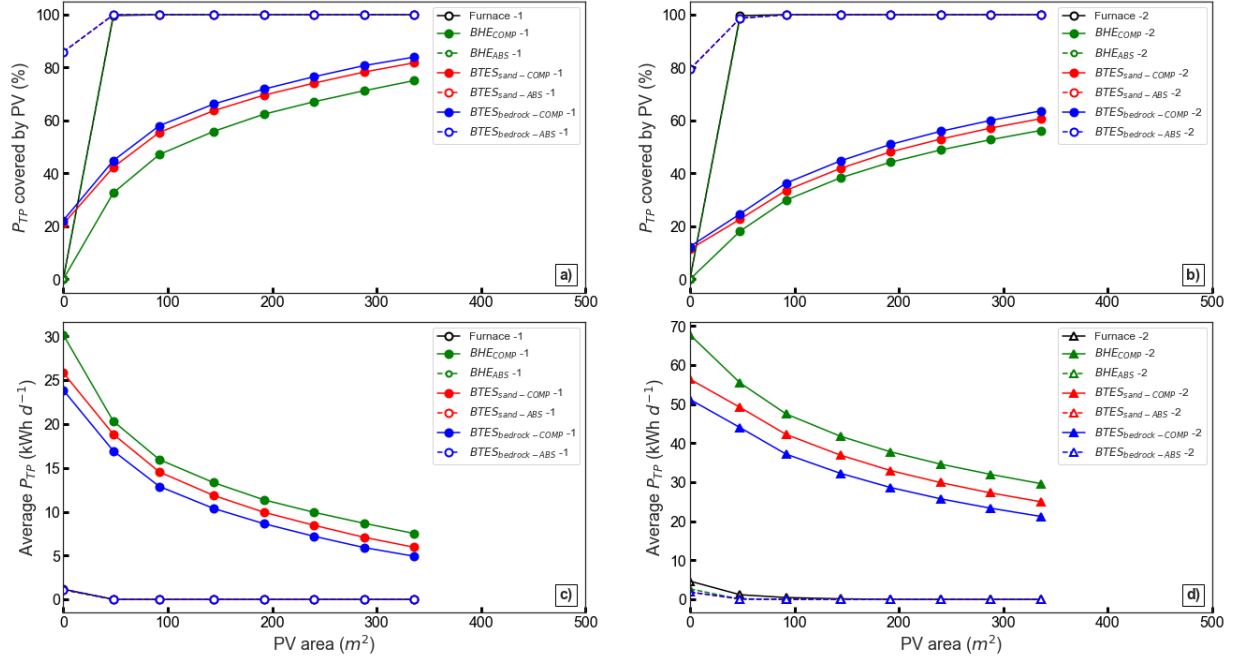


**Fig.3.15:** PV area used vs. electricity needs covered by the PV area and average  $P_{TP}$  consumed by the heating systems simulated for one (a, c) and two (b, d) buildings.

The CO<sub>2</sub> emissions of the Furnace-1 and Furnace-2 scenarios over 20 years of operation without using electricity derived from solar panels were 241.1 and 496.3 tons, respectively (Fig.3.16a and b). These scenarios show the highest  $Cost_{HSYS\ customer}$  (126,910 and 254,896 \$CAN) among scenarios due to the high fuel oil consumption by the furnaces (Fig.3.16c and d). However,  $Cost_{HSYS\ societal}$  for Furnace-1 (164,215 \$CAN) and Furnace-2 (340,409 \$CAN) scenarios is lower than when a GHE is coupled to a COMP without PV (Fig.3.16e and f).

The results from the present studies suggest that ABS coupled to BTES using thermal storage derived from PV electricity is not a viable option for the Nunavik context. The thermal energy stored in the ground mostly dissipates before it can be recovered whether there is presence of significant groundwater velocities (BTES<sub>sand</sub>-ABS-1 and BTES<sub>sand</sub>-ABS-2) or not (BTES<sub>bedrock</sub>-ABS-1 and BTES<sub>bedrock</sub>-ABS-2) due to its low COP and therefore, its low efficiency to extract ground thermal energy. However, BHE<sub>ABS</sub>-1 and BHE<sub>ABS</sub>-2 scenarios have the lowest CO<sub>2</sub> emissions,  $Cost_{HSYS\ customer}$  and  $Cost_{HSYS\ societal}$  for PV area < 48 m<sup>2</sup> compared to the other scenarios responding to the heating demand of one and two residential buildings, respectively. For comparison, those scenarios reduced by 27% CO<sub>2</sub> emissions (-64.0 tons), by 13%  $Cost_{HSYS\ customer}$  (-34,398 \$CAN) and by 13%  $Cost_{HSYS\ societal}$  (-43,341 \$CAN) compared to the Furnace-1 scenario. The

COMP scenarios with PV area  $< 48 \text{ m}^2$  have lower energy costs paid by the customer than ABS scenarios and have the highest CO<sub>2</sub> emissions and societal energy costs since the amount of electricity derived from the thermal plant is too high.

COMP scenarios using PV electricity achieve higher CO<sub>2</sub> emissions and  $\text{Cost}_{\text{HSYS societal}}$  savings that become increasingly important with more PV area (Fig.3.16). Based on the  $\text{Cost}_{\text{HSYS customer}}$  and neglecting installation costs, COMP is more interesting than ABS for customer with any PV area. However, COMP have lower  $\text{Cost}_{\text{HSYS societal}}$  than ABS for PV area  $> 96$  and  $288 \text{ m}^2$  for one and two buildings, respectively. When considering the greatest PV area ( $336 \text{ m}^2$ ), BHE<sub>COMP-1</sub> and BHE<sub>COMP-2</sub> scenarios show the lowest CO<sub>2</sub> emissions (-61 and -42%),  $\text{Cost}_{\text{HSYS customer}}$  (-72 and -60%) and  $\text{Cost}_{\text{HSYS societal}}$  (-56 and -32%) savings compared to Furnace-1 and Furnace-2 scenarios, respectively. BTES<sub>bedrock-COMP-1</sub> and BTES<sub>bedrock-COMP-2</sub> scenarios with PV area =  $336 \text{ m}^2$  have similar CO<sub>2</sub> emissions (-56 and -41%),  $\text{Cost}_{\text{HSYS customer}}$  (-64 and -56%) and  $\text{Cost}_{\text{HSYS societal}}$  (-53 and -34%) savings compared to the base case scenarios while maintaining  $T_{\text{inlet}} > -6.7 \text{ }^{\circ}\text{C}$  through their respective 20-year simulated period (Fig.3.17). It is interesting to note the trend difference between the CO<sub>2</sub> emissions vs.  $\text{Cost}_{\text{HSYS customer}}$  and CO<sub>2</sub> emissions vs.  $\text{Cost}_{\text{HSYS societal}}$  for the scenarios since  $\text{Cost}_{\text{HSYS societal}}$  is reduced at a higher rate than  $\text{Cost}_{\text{HSYS customer}}$  as the PV area increases (Fig.3.17).

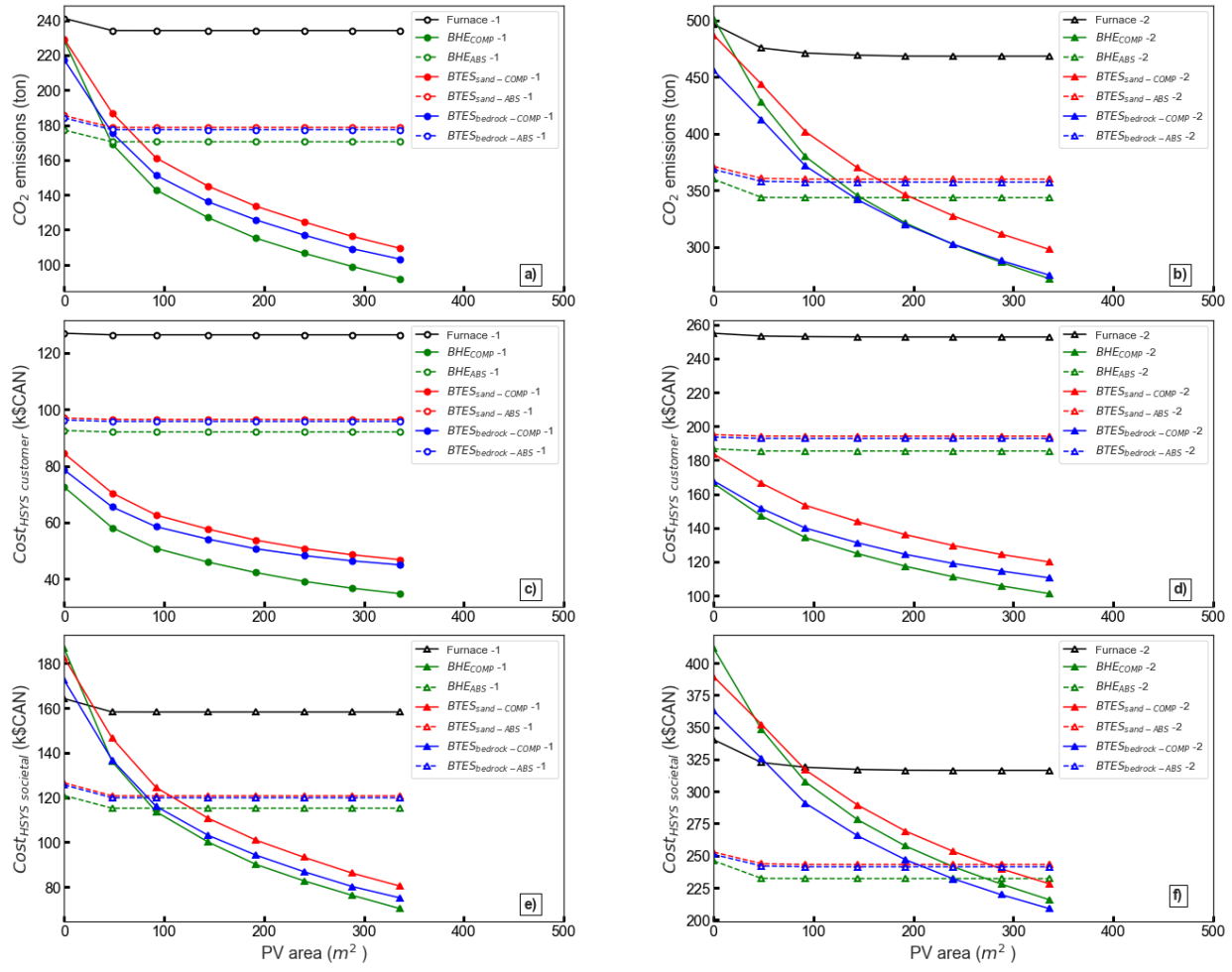


**Fig.3.16:**  $CO_2$  emissions,  $Cost_{HSYS}$  customer and  $Cost_{HSYS}$  societal of the simulated scenarios providing the heating demand of one (a,c,e) and two residential buildings (b,d,f).

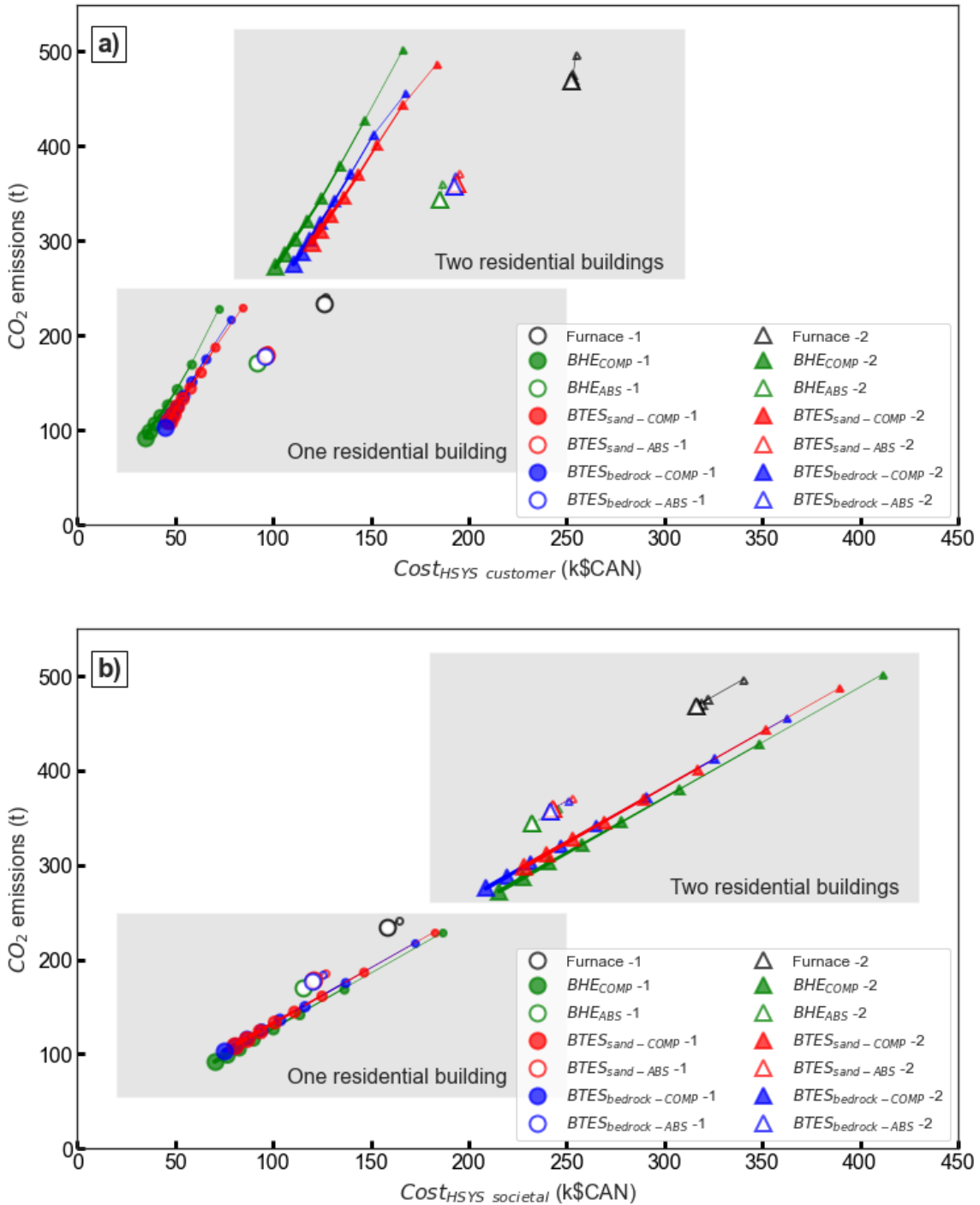


**Fig.3.17:**  $\text{Cost}_{\text{HSYS customer}}$  vs.  $\text{CO}_2$  emissions a) and  $\text{Cost}_{\text{HSYS societal}}$  vs.  $\text{CO}_2$  emissions b) of the simulated scenarios. Each scenario has eight symbols representing the electrical assistance of a PV area where a line gets thicker from the smallest area of  $0 \text{ m}^2$  (smaller symbols) towards the largest area of  $336 \text{ m}^2$  (bigger symbols) with constant steps of  $48 \text{ m}^2$ .

## 3.5. Discussion

### 3.5.1 Assumptions and uncertainty for the simulated geothermal systems

The simulations performed in this study do not aim to predict the exploitation of a specific GCHP at the CEN in WK. Instead, they provide a comparison among geothermal systems efficiency. Simulations performed took into account reasonable sizing of heating systems based on their expected efficiency, but other equipment (e.g. heat exchangers) and parameters (e.g. pressure within the circuit) were not taken into account. The estimated heating demand  $P_{HD}$  was calibrated with monthly diesel bill for three different CEN buildings including the analyzed one (Fig.3.1). Nonetheless, the estimated  $P_{HD}$  is considered as a reasonable heating demand for a building in a subarctic climate. Further monitoring will be necessary to confirm the building's heating and domestic hot water consumption to better design a proper geothermal and PV system for the building studied at the CEN. Many assumptions were also made for the  $P_{EPV}$  and electricity storage yearly profiles. For example, this study did not consider the wear of batteries since simulations were made from a subsurface perspective. Even though ABS scenarios would have required shorter GHE, all models were simulated with the same total 300 m GHE length for comparison purposes between BHE and BTES scenarios. BTES scenarios would be difficult to compare if the GHE length was shorten due to very different ground thermal storage volume and shape, heat injection dynamics and heat storage efficiency. Also, using oversized GHE for ABS scenarios slightly affect energy costs due to the steady COP  $\approx 1.2$ .

This study estimated a  $Cost_{HSYS\ customer}$  and  $Cost_{HSYS\ societal}$  to deepen comparisons between scenarios, but it does not allow to evaluate installation costs of heating systems. Previous studies already made thorough installation and energy costs evaluations and estimated that geothermal systems' profitability is feasible both for COMP and ABS (Gunawan et al., 2020). Energy costs are one of the most critical parameters that influences a heating system's economic viability (Gunawan et al., 2020). Installation costs are not the core topic of this study and therefore they were not assessed. Northern regions have many techno-economic constraints and estimating the profitability of a heating system in Nunavik is a tedious process. Therefore, it would be necessary to proceed to a detailed economic assessment and life cycle analysis of different options such as presented in Gunawan (2020) or complying to ISO 14040 et 14044 standards if an actual geothermal system is to be installed.

Assumptions were also made to simulate groundwater recharge periods. A local hydrogeological study in the vicinity of the CEN station would reduce uncertainty related to groundwater effects. However, the present numerical models allowed simulating numerous complex phenomenon that were not investigated by aforementioned studies in northern climate (Belzile et al., 2017; Garber-Slaght and Peterson, 2017; Kanzari, 2019; Giordano and Raymond, 2019; Gunawan et al., 2020). Despite various limitations, the numerical models provided an in-depth comparison of heating systems for northern communities.

### 3.5.2 Geothermal systems in northern climate

Geothermal systems have been installed (Garber-Slaght and Peterson, 2017) and studied (Belzile et al., 2017; Kanzari, 2019; Giordano and Raymond, 2019; Gunawan et al., 2020) in northern climates. These heating systems proved to reduce CO<sub>2</sub> emissions and provided energy costs savings which can contribute to address energy issues currently faced by remote northern communities using fuel oil furnaces only. Some types of heat pump and GHE may be prioritised over others depending on ground thermal interaction and the project's constraints, thus efforts should be made to differentiate their pros and cons.

ABS coupled to BHE are more suitable to provide high or low heating demand when there is no PV available. It is worth noting that ABS also requires a shorter GHE length than COMP systems because it has a low COP  $\approx 1.2$  and has lower installation costs since GHE drilling can be as expensive as 350 \$ m<sup>-1</sup> in the Nunavik context (Gunawan et al., 2020). It is not recommended to use PV energy only to provide GCHP using ABS since it minimizes  $P_{TP}$  consumption similarly to currently used furnaces (Fig.3.15). It seems more reasonable to use PV energy for the daily household appliances or to return it to the local grid to have a compensatory return. These results agree with studies that simulated ABS operation coupled to horizontal GHE (Belzile et al., 2017) or BHE (Kanzari, 2019; Gunawan et al., 2020) and CO<sub>2</sub> emissions and energy costs are reduced compared to heating systems using fuel oil furnace only when there is no PV available.

Results show that using COMP to heat buildings is more suitable than ABS when assisted with sufficient PV electricity. It is considered that COMP providing a low heating demand ( $P <$  one residential building) is profitable for the customer and society when  $\approx 50\%$  of electricity needs of the heating system is at least covered by PV electricity since required PV area and GHE length remain reasonable for a single residential building. As demonstrated by Gunawan (2020), the higher proportion of electricity derived from PV there is and the lower the energy costs will be. These estimations neglect solar energy storage in batteries and consider that COMP coupled to BHE were powered by 70% (PV area  $\approx 42 \text{ m}^2$ ) and 100% (PV area  $\approx 60 \text{ m}^2$ ) of PV energy based on an annual average solar PV potential in Kuujjuaq. Solar energy storage has a low efficiency ( $\approx 60\%$ ) and electrical needs are too high to be sustained by PV electricity in winter during which there is minimal solar radiation (Fig.3.6). Therefore, in practice, electrical needs cannot be annually covered by PV electricity as was estimated by Gunawan (2020). They considerably underestimated the required amount of PV panels considering that  $\approx 70\%$  of  $P_{TP}$  needs of BHE<sub>COMP-1</sub> can be covered with PV area  $\approx 336 \text{ m}^2$  (Fig.3.15a). Their calculated costs were then overestimated, although economical viability of such heating system would still be viable compared to diesel furnaces currently used.

Even though BTES should not be installed in permeable materials experiencing groundwater flow such as silty sand, thermal storage of heat derived from PV electricity with COMP coupled to BTES has a

great potential to provide high heating demand ( $P >$  one residential building) when installed in less permeable materials. Heat injection periods of solar energy during summer increases the ground  $T$  and allows to use COMP in a subarctic climate, leading to CO<sub>2</sub> emissions (-41%),  $Cost_{HSYS\ customer}$  (-56%) and  $Cost_{HSYS\ societal}$  (-34%) savings compared to currently used furnaces. BTES where  $\approx$ 60% of electricity needs are at least covered by PV electricity would require approximately half GHE length than BHE to provide the heating demand of two residential buildings since a BHE would require GHE  $\approx$  600 m to reach a minimal  $T_{inlet}$  of -6 °C while a BTES only need 300 m of GHE to reach the same minimal  $T_{inlet}$ . BTES are more suitable for high heating demand since it requires many PV panels to significantly increase ground  $T$  and it also requires many GHE to have a large ground thermal storage that can efficiently retain ground thermal energy from summer to winter. Giordano (2019) also assessed the potential of BTES in northern communities, but they have based their study on a massive heating system for the specific low-temperature heating of drinking water application without using heat pumps, while a study of BTES providing a more common application such as space heating was not done previously for Nunavik.

An in-depth technical study of various GCHP was made at the same study site allowing to assess their application in a subarctic climate, where none of the previous studies addressed these comparisons using thorough analysis of ground thermal interaction. This study also proved that detailed solar analysis is crucial in northern climates due to the annually unbalanced solar radiation. Simplified energy costs were estimated to demonstrate that BTES can be profitable at smaller scale than previously studied in more common applications such as space heating (Giordano and Raymond, 2019).

Using renewable energies, such as solar, to supply electricity needs for heating purposes is essential to use COMP and reduce load on the local grid during winter. It would be even more profitable to use other renewable energies, such as biomass, wind or hydro power, to provide peak heating or electrical demand not supplied by solar energy during winter. The use of geothermal systems can allow to reduce Nunavik's dependency on the fossil fuel market but also enhance the potential of other renewable sources. The penetrating rate of solar energy in a BTES is better than in a BHE due to thermal energy storage in summer, while excess solar energy in a BHE would have to be injected in the local grid. However, it would be interesting to assess societal and customer energy costs considering potential paybacks derived from excess PV electricity injected in the local grid. Installation costs of GCHP can be rapidly repaid if the designed system is optimized due to the appealing  $Cost_{HSYS\ customer}$  and  $Cost_{HSYS\ societal}$  savings. Using only fuel oil furnaces involves low installation costs but it ties customers to the unpredictable fossil fuel market and high maintenance costs. Moreover, it involves high CO<sub>2</sub> emissions,  $Cost_{HSYS\ customer}$  and  $Cost_{HSYS\ societal}$  plus other expenses and problems such as ground decontamination in case of potential oil spills (Gouvernement du

Canada, 2021; CBC, 2022). The combination of various renewable energies would significantly decrease GHG emissions, energy costs, and accelerate the energy transition in Canada.

### 3.6. Conclusions

Efficiency and energy costs of different solar assisted geothermal systems were assessed and compared to currently implemented heating systems in a subarctic climate. Three-dimensional numerical models of BHE and BTES coupled to ABS or COMP were simulated for 20-year periods to calculate their efficiency, CO<sub>2</sub> emissions, and energy costs based on field observations collected in the vicinity of the CEN research station in Whapmagoostui-Kuujjuarapik (Nunavik, Canada). Results show that when electricity is provided by the local thermal power plant only, ABS coupled to BHE is the most suitable option considering diesel and CO<sub>2</sub> emissions, providing  $Cost_{HSYS\ customer}$  and  $Cost_{HSYS\ societal}$  savings of 27% and compared to currently used diesel furnaces, respectively. However, COMP coupled to BHE or BTES can achieve significantly higher diesel and CO<sub>2</sub> emissions savings up to 61%, with  $Cost_{HSYS\ customer}$  savings up to 72% when there is at least 60% of electricity needs covered by solar PV panels compared to a fossil-fuel scenario. Solar assisted COMP coupled to BHE is more suitable to provide low heating demand ( $P <$  one residential building), while BTES with COMP is interesting for high heat demanding situations ( $P >$  one residential building).

The northern energy context in Canada not only has techno-economical restrictions, but also social and political constraints which are essential to understand in the implementation of a heating system (Paquet et al., 2021; Rodon et al., 2021). This study was part of a research project aiming to better understand energy issues in Nunavik. The contribution of this and other studies conducted by the multidisciplinary research group investigating this subject is crucial to offer a sustainable integration of renewable energies in contexts similar to the Nunavik territory.

### **III. Conclusions**

## 1. Synthèse des résultats

Le chapitre 1 du projet de maîtrise traite de l’O-TRT avec un câble chauffant installé en tranchée afin d'estimer à la fois la  $\lambda$  et la  $\alpha$  de dépôts meubles. Cette méthode a été appliquée auparavant par Oberdorfer (2014) et Giordano (2020) dans des échangeurs de chaleur géothermique où la durée des essais demeure élevée afin de composer avec les matériaux qui entourent les échangeurs de chaleur. L’O-TRT a été développé au cours du projet de maîtrise avec un câble chauffant directement en contact avec le matériel à analyser afin de repousser les connaissances dans le domaine de la caractérisation de la sous-surface à l'aide d'une méthode analytique sans résistance interne de la source de chaleur. Cette méthode analytique inspirée des études précédentes présume de simplifications et repose sur un appareillage dont les mesures apportent des incertitudes systématiques. Il a été possible de corriger les valeurs estimées à l'aide d'un matériel de référence dont la  $\lambda$  et la  $\alpha$  sont connues. Neuf essais de réponse thermique oscillatoires différents ont été réalisés en laboratoire pour un matériau standardisé (sable d'Ottawa) en condition sèche pour corriger les valeurs estimées analytiquement. Cinq O-TRT ont aussi été réalisés en condition *in situ* dans un dépôt sableux naturel à Whapmagoostui-Kuujjuarapik afin de vérifier son potentiel d'application en condition *in situ* de terrain. Une approche numérique a également été développée afin de valider les résultats des essais estimés avec l'approche analytique.

L'analyse des O-TRT réalisés dans le sable d'Ottawa a permis d'estimer un facteur de correction de la  $\lambda$  et de la  $\alpha$  de 1.062 et de 1.037, respectivement. Après validation par modélisation numérique, les résultats montrent que l'approche analytique utilisant des facteurs de correction a permis d'estimer la  $\lambda$  et la  $\alpha$  dans le sable d'Ottawa avec une différence de 1.4% et de 1.7%, respectivement. La différence entre les valeurs de la  $\lambda$  et de la  $\alpha$  analytiques corrigées et numériques dans le sable de Whapmagoostui-Kuujjuarapik sont de 1.9% et de 1.2%, respectivement. Cette étude démontre que la méthode de l’O-TRT et son approche analytique est utile pour évaluer avec exactitude à la fois  $\lambda$  et  $\alpha$ . Des essais supplémentaires dans d'autres matériaux de référence et avec différentes configurations d'appareils sont nécessaires pour améliorer la configuration expérimentale et étendre l’O-TRT vers de nouvelles applications. Néanmoins, le développement de cette méthode au cours du projet de maîtrise a permis de valider une méthode expérimentale novatrice ayant une faible durée d'essai et un faible coût tout en offrant une meilleure exactitude que ce qui est présentement offert dans le domaine pour déterminer les propriétés thermiques de la sous-surface de façon *in situ*.

Le sujet du chapitre 2 du projet de maîtrise visait à évaluer l'influence des paramètres sur la performance d'un BTES couplé à une pompe à chaleur en milieu subarctique. Pour ce faire, un scénario de base a été développé et une étude paramétrique a été réalisée variant de 10% et de 30% les 17 paramètres considérés dans la conception d'un BTES couplé à une pompe à chaleur. Un total de 68 scénarios simulant

l'opération de BTES a été développé dans des modèles numériques en trois dimensions en intégrant le calcul de l'écoulement souterrain et des transferts de chaleur d'un matériel représentant un roc granitique représentatif du sous-sol à la station du CEN de Whapmagoostui-Kuujjuarapik. Le COP de la pompe à chaleur a été moyenné pour le scénario de base ainsi que pour tous les autres scénarios afin de comparer la performance du système selon la variation des paramètres d'entrée. L'analyse paramétrique montre que l'extraction et l'injection de chaleur, le ratio surface/volume du BTES, l'espacement entre les échangeurs de chaleur, l'orientation des échangeurs de chaleur en fonction de la direction de l'écoulement d'eau souterraine et les propriétés thermiques du sol sont les paramètres ayant la plus grande influence sur le COP et la performance des BTES. Il est pertinent de se baser sur les résultats obtenus dans cette étude afin de comprendre les principaux paramètres à considérer pour offrir le dimensionnement approprié d'un BTES et rencontrer les performances attendues du système de chauffage.

Les conclusions de l'étude présentée au chapitre 2 ont été utilisées dans le chapitre 3 du projet de maîtrise afin d'étudier la performance et la pertinence de BTES et d'un BHE assistés par des PV en contexte subarctique au Nunavik. Cette étude visait à comparer différents modèles numériques simulant l'opération de BTES et de BHE couplés à des COMP et ABS afin d'estimer leur impact sur la température du sol, leur consommation énergétique, le CO<sub>2</sub> équivalent émis dans l'atmosphère ainsi que leur coût énergétique total. Douze scénarios ont été développés à l'aide de données caractéristiques de l'hydrogéologie, la thermogéologie, la consommation énergétique d'un bâtiment et la production électrique de PV obtenues dans la région de Whapmagoostui-Kuujjuarapik. La puissance de chaleur injectée dans le sol ou extraite à partir du sol, le ratio surface/volume, l'espace entre les échangeurs de chaleur, la disposition des échangeurs de chaleur en fonction de l'écoulement de l'eau souterraine et les propriétés thermiques du sol sont les paramètres ayant la plus grande influence sur l'efficacité du système géothermique.

Les simulations de modèles numériques montrent que les ABS couplées à un BHE ont les plus faibles émissions de CO<sub>2</sub> et coûts d'énergie parmi les scénarios où l'assistance solaire n'est pas considérée. Ils permettent d'économiser 27% des émissions de CO<sub>2</sub>, des coûts énergétiques sociaux et des coûts d'énergie pour les consommateurs comparativement à un système de chauffage utilisant seulement une fournaise au mazout. Cependant, une utilisation suffisante d'électricité dérivée de PV (50 à 60%) permet de justifier l'utilisation d'une COMP et de significativement améliorer les économies énergétiques et monétaires comparativement aux ABS et aux fournaises au mazout. L'injection de chaleur intégrée dans l'opération des BTES permet de contrebalancer l'extraction de chaleur annuelle à partir du sol et ainsi utiliser des COMP efficaces pour subvenir à une demande en chauffage élevée ( $P >$  bâtiment résidentiel unifamilial) afin d'économiser 41% des émissions de CO<sub>2</sub>, 34% des coûts énergétiques sociaux et 56% des coûts d'énergie pour les consommateurs comparativement à un système de chauffage utilisant seulement

une fournaise au mazout. De leur côté, l'utilisation de BHE couplé à une COMP et assisté par un nombre suffisant de PV est plus approprié pour fournir une demande en chauffage faible ( $P <$  bâtiment résidentiel unifamiliale) en raison de la basse température du sol et du débalancement thermique causé par la demande en chauffage continu. Ce type de système permet alors d'économiser 61% des émissions de CO<sub>2</sub>, 60% des coûts énergétiques sociaux et 72% des coûts d'énergie pour les consommateurs comparativement à un système de chauffage utilisant seulement une fournaise au mazout. Ce travail a eu recourt à des analyses pertinentes offrant des comparaisons technico-économiques entre les différents systèmes de chauffage en se basant sur des simulations approfondies considérant les GHE et le sol. Malgré le fait que les coûts d'installation de systèmes géothermiques sont rentabilisés après quelques années seulement en raison des économies monétaires importantes (Gunawan et al., 2020), il serait pertinent de considérer les coûts d'installation des systèmes afin d'approfondir ces analyses économiques. Ce travail donne un aperçu de la façon dont différents systèmes géothermiques devraient être utilisés dans le climat subarctique du Nunavik ou dans d'autres contextes similaires.

## 2. Conclusions du mémoire de maîtrise

Les résultats et conclusions tirés du mémoire de maîtrise peuvent être utilisés dans plusieurs secteurs du domaine de l'énergie géothermique. Le développement de la méthode de l'O-TRT avec un câble chauffant installé en tranché a permis d'améliorer l'exactitude liée à l'estimation *in situ* de propriétés thermiques comparativement aux autres méthodes disponibles dans le domaine de la caractérisation de la sous-surface. Le déploiement de cette méthode a consisté à adapter un appareillage pour placer l'élément chauffant en contact avec un matériel afin d'injecter de la chaleur de façon oscillatoire et d'enregistrer la réponse thermique du sol. Cette réponse thermique a ensuite été analysée analytiquement dans deux matériaux différents et des modèles numériques développés en trois dimensions ont permis de valider les valeurs obtenues avec la méthode analytique. Cette méthode demeure peu dispendieuse pour estimer avec exactitude les propriétés thermiques de la sous-surface. Cependant, l'appareillage utilisé pour la méthode de l'O-TRT nécessite de poser des hypothèses pour corriger l'estimation des propriétés thermiques du sol en raison de l'emmagasinement thermique des capteurs de température. Dans des travaux futurs, il serait possible d'éviter de poser ces hypothèses en utilisant des capteurs de température plus petits afin d'améliorer l'appareillage et le déploiement de la méthode.

L'O-TRT a également été appliquée pour les autres parties du mémoire de maîtrise afin d'étudier l'opération de systèmes géothermiques. Une étude paramétrique a permis de déterminer que la quantité d'énergie extraite/injectée, la disposition des échangeurs de chaleur, les propriétés thermiques et les conditions hydrogéologiques ont la plus grande influence sur la performance des BTES. Finalement, une étude approfondie intégrant la modélisation numérique du sous-sol a été réalisée afin d'évaluer l'efficacité

et de qualifier le potentiel de divers systèmes géothermiques dans le contexte complexe du Nunavik. Les simulations numériques résultantes ont permis d'estimer la consommation et les coûts énergétiques de différents systèmes de chauffage intégrant ou non les pompes à chaleur géothermiques assistées par de l'électricité produite de PV. Ces résultats ont été comparés afin de déterminer le potentiel de chacun des systèmes dans le contexte du Nunavik. Les conclusions tirées de cette étude et du mémoire de maîtrise contribuent à comprendre davantage les divers phénomènes techniques relatifs au sol intervenant dans le dimensionnement d'un système géothermique dans un milieu subarctique similaire à celui du Nunavik. Il serait pertinent de combiner les résultats de ces études pour effectuer une étude de faisabilité dans un bâtiment cible dans la région de Whapmagoostui-Kuujjuarapik. L'un des principaux objectifs du présent mémoire est de comparer les différents systèmes géothermiques et certaines hypothèses ont été posés afin de simplifier ces comparaisons. Intégrer des estimations plus exactes de la demande énergétique et de la production d'électricité produite de PV d'un ou plusieurs bâtiments dans des travaux futurs permettrait d'offrir un banc d'essai de référence pour le Nunavik et les climats nordiques. Néanmoins, les études comparatives présentées sont essentielles pour les études de faisabilité comme elles facilitent la compréhension du potentiel et des limitations relatives dans l'exploitation de systèmes géothermiques en climat nordique. Les études présentées dans ce mémoire de maîtrise permettent une implémentation durable d'énergies renouvelables pour subvenir aux besoins en chauffage de ces communautés isolées où il est plus que nécessaire de réduire leur impact environnemental.

## Références

- American Society of Heating, Refrigeration & Air-Conditioning Engineers (ASHRAE) (2001). Investigation of methods for determining soil formation thermal characteristics from short term field tests, ASHRAE (RP-1118). Atlanta, United States, 86 p.
- American Society for Testing and Materials (ASTM) (2008). Standard test method for determination of thermal conductivity of soil and soft rock by thermal needle probe procedure (D5334). ASTM International, West Conshohocken, United States, 9 p.
- Anbergen H., Rühaak W., Frank J., Sass I. (2015). Numerical simulation of a freeze-thaw testing procedure for borehole heat exchanger grouts, Canadian geotechnical journal 52(8), 1087- 1100. <https://doi.org/10.1139/cgj-2014-0177>
- Atlas climatique du Canada (2019). Carte des Degrés-jour de chauffage. Retrieved from: [https://atlasclimatique.ca/carte/canada/hdd\\_2060\\_85#](https://atlasclimatique.ca/carte/canada/hdd_2060_85#)
- Beier R.A. (2020). Deconvolution and convolution methods for thermal response tests on borehole heat exchangers, Geothermics 86, 15 p. <https://doi.org/10.1016/j.geothermics.2019.101786>
- Belzile P., Comeau F.-A., Raymond J., Lamarche L., Carreau M. (2017). Arctic climate horizontal groundcoupled heat pump. GRC Transactions 41, 1958- 1978.
- Carslaw H.S. (1945). Introduction to the mathematical theory of the conduction of heat in solids, second ed. Dover, New York, United States, 268 p.
- Carslaw H.S., Jaeger J.C. (1947). Conduction of heat in solids. Oxford University Press, Oxford, England, 249 p.
- Casasso A., Sethi R. (2014). Sensitivity analysis on the performance of a ground source heat pump equipped with a double U-pipe borehole heat exchanger, Energy Procedia 59, 301–308. <https://doi.org/10.1016/j,egypro.2014.10.381>
- Catolico N., Ge S., McCartney J.S. (2016). Numerical modeling of soil-borehole thermal energy storage system, Vadose zone journal, vol. 15, 17 p. <https://doi.org/10.2136/vzj2015.05.0078>
- CBC (2022). Government of Nunavut ordered to pay \$100k for 2020 fuel spill. Retrieved from: <https://www.cbc.ca/news/canada/north/rankin-inlet-fuel-spill-fine-1.6432633>
- CEN (2017). Données des stations climatiques de la région de Whapmagoostui-Kuujjuarapik au Nunavik, Québec, Canada, v. 1.4 (1987-2019). Nordicana D4. <https://doi.org/10.5885/45057SL-EADE4434146946A7>
- Ciesielski A. (1991). Geology of the eastern Superior Province, James Bay and Bienville subprovinces (Public file 2398), Geological Survey of Canada, 8 p.

CIMA+ (2014). Amélioration du système d'approvisionnement d'eau potable Première Nation Crie de Whapmagoostui et Communauté Inuit de Kuujjuarapik - Recherche en eau souterraine et construction du puits P-2, Hydrogeological report. Quebec City, Canada. 216 p.+ annexes.

Claesson J., Eskilson P. (1988). Conductive heat extraction to a deep borehole: Thermal analyses and dimensioning rules, Energy 13 (6), 509-527, [https://doi.org/10.1016/0360-5442\(88\)90005-9](https://doi.org/10.1016/0360-5442(88)90005-9)

Comeau F.-A., Raymond J., Malo M., Dezayes C., Carreau M. (2017). Geothermal Potential of Northern Québec: A Regional Assessment, GRC Transactions 41. 19 p.

Comeau F.-A., Giordano N., Raymond J. (2020). Shallow geothermal potential of the northern community of Whapmagoostui-Kuujjuaraapik, INRS (R1927), Quebec city, Canada, 19 p.  
<https://espace.inrs.ca/id/eprint/11360>

Compensation CO<sub>2</sub> Québec (2022). Calculateur. Retrieved from:  
<https://www.compensationco2.ca/fr/calculateur/>

Dalla Santa G., Galgaro A., Sassi R., Cultrera M., Scotton P., Mueller J., Bertermann D., Mendrinos D., Pasquali R., Perego R., et al. (2020). An updated ground thermal properties database for GSHP applications. Geothermics 85, 13 p. <https://doi.org/10.1016/j.geothermics.2019.101758>

Deerman J.D., Kavanaugh S.P. (1991). Simulation of vertical U-tube ground-coupled heatpump systems using the cylindrical heat source solution. ASHRAE Transactions 97, 287-295.

Déry P., Bourbonnais M. (2018). L'utilisation du solaire photovoltaïque pour le préchauffage de l'eau domestique résidentielle : une solution rentable pour le Québec? (Affiche scientifique) 86<sup>e</sup> Congrès de l'ACFAS,

Deslauriers J.-C. (2008). Le Plan d'approvisionnement 2008-2017 des réseaux autonomes d'Hydro-Québec Distribution (Report R-3648-2007), Régie de l'énergie. Quebec city, Canada, 50 p.

Diersch H-JG, Bauer D, Heidemann W, Ruhaak W, Schatzl P. (2011). Finite element modelling of borehole heat exchanger systems Part 2. Numerical simulation, Computers & Geosciences 37, 1136–1147.  
<https://doi.org/10.1016/j.cageo.2010.08.002>

Diersch H.-J. (2014). Finite element modeling of flow, mass and heat transport in porous and fractured media. Springer, 996 p. [www.doi.org/10.1007/978-3-642-38739-5](http://www.doi.org/10.1007/978-3-642-38739-5)

Dowfrost (2008). Engineering and Operating Guide for DOWFROST and DOWFROST HD Inhibited Propylene Glycol-based Heat Transfer Fluids, Form 180-01286-0208 AMS, 44 p.

EcoForest (2020). Fiche technique ecoGEO, pompes à chaleur géothermiques. Retrieved from :  
<http://www.ecoforest.fr>

Environment Canada (2021). Statistiques climatiques de la station de Kuujjuarapik no. 7103536 de 2012 à 2013.

Environmental Protection Agency (2021). How the 1-100 ENERGY STAR Score is Calculated. Portfolio Manager Technical Reference: ENERGY STAR Score. EPA, Washington, United States, 14 p.

Eskilson P. (1987). Thermal analysis of heat extraction boreholes. PhD thesis, University of Lund, Lund, Sweden.

Farouki O.T. (1986). Thermal properties of soils (Series on rock and soil mechanics). Trans Tech Publication 11, Clausthal-Zellerfeld, Germany.

Fortier R., Allard M., Lemieux J.-M., Therrien R., Molson J., Fortier D. (2011). Stratégie de déploiement du réseau Immatsiak: cartographie des dépôts quaternaires et compilation des informations disponibles des villages nordiques de Whapmagoostui, Umiujaq, Salluit et Kuujjuaq. Université Laval, Quebec City, Canada, 107 p.

Garber-Slaght R., Peterson R. (2017). Can Ground Source Heat Pumps Perform Well in Alaska?, Conference: IGSHPA Technical/Research Conference and Expo 2017, Denver, United Stats, 9 p.  
<https://doi.org/10.22488/okstate.17.000525>

Gehlin S. (2002). Thermal response test – method development and evaluation, Doctoral thesis, Luleå University of Technology, Lund, Sweden.

Geosmart Energy (2013). Premium Q Series Specification Catalog. Retrieved from:  
<https://www.geosmartenergy.com/products/residential/premiumq/>

Giordano N., Raymond J. (2019). Alternative and sustainable heat production for drinking water needs in a subarctic climate (Nunavik, Canada): Borehole thermal energy storage to reduce fossil fuel dependency in off-grid communities. Applied Energy 252, 20 p.  
<https://doi.org/10.1016/j.apenergy.2019.1134643>

Giordano N., Raymond J. (2020). Field report and monitoring plan of the ground source heat pump system for the community swimming pool in Kuujjuaq (Nunavik, Canada) (Research report R2007), INRS, Centre Eau, Terre et Environnement, Quebec City, Canada, 33 p. + appendices.

Giordano N., Lamarche L., Raymond J. (2021). Evaluation of subsurface heat capacity through oscillatory thermal response tests. Energies 14 (5791), 26 p. <https://doi.org/10.3390/en14185791>

Gouvernement du Canada (2021). National Pollutant Release Inventory Indigenous Series: Nunavik, Retrieved from: <https://www.canada.ca/en/environment-climate-change/services/national-pollutant-release-inventory/tools-resources-data/nunavik.html>

Gouvernement du Québec (2022). Marché du carbone : Ventes aux enchères, Ministère de l'Environnement et de la Lutte contre les changements climatiques. Retrieved from:  
<https://www.environnement.gouv.qc.ca/changements/carbone/Ventes-encheres.htm>

GPR International inc. (2002). WhapmagoostuiKuujjuarapik water project. Final report M-02546 presented to the Whapmagoostui band council. Whapmagoostui, Québec, 141 p.

Grainger E. H. (1988). The influence of a river plume on the sea– ice meiofauna in south-eastern Hudson Bay, Estuarine, Coastal and Shelf Science 27, 131–141. [https://doi.org/10.1016/0272-7714\(88\)90086-8](https://doi.org/10.1016/0272-7714(88)90086-8)

Guillou-Frottier L., Mareschal J.-C., Jaupart C., Gariépy C., Lapointe R., Bienfait G. (1995). Heat flow variations in the Grenville Province, Canada. Earth and Planetary Science Letters 136, 447-460. [https://doi.org/10.1016/0012-821X\(95\)00187-H](https://doi.org/10.1016/0012-821X(95)00187-H)

Gunawan E., Giordano N., Jensson P., Newson J., Raymond J. (2020). Alternative heating systems for northern remote communities: Techno-economic analysis of ground-coupled heat pumps in Kuujjuaq, Nunavik, Canada. Renewable Energy 147, 1540-1553. <https://doi.org/10.1016/j.renene.2019.09.039>

Hanson J.L., Neuhaeuser S., Yesiller N. (2004). Development and calibration of a large-scale thermal conductivity probe. Geotechnical Testing Journal 27 (4), 393-403. <https://doi.org/10.1520/GTJ11052>

Hellström G. (1991). Ground heat storage: thermal analyses of duct storage systems, Lund University, Lund, Sweden. 262 p.

Hydro-Québec (2021). Réseaux autonomes, portrait d'ensemble et perspectives d'avenir, Retrieved from: [http://publicsde.regie-energie.qc.ca/projets/40/DocPrj/R-3776-2011-B-0058-DEMANDE-PIECE-2011\\_08\\_01.pdf](http://publicsde.regie-energie.qc.ca/projets/40/DocPrj/R-3776-2011-B-0058-DEMANDE-PIECE-2011_08_01.pdf), 2011.

Hydro-Québec (2022). Tarif DN. Retrieved from: <https://www.hydroquebec.com/residentiel/espace-clients/tarifs/tarif-dn.html>

Ingersoll L.R., Zobel O.J., Ingersoll A.C. (1954). Heat Conduction, with Engineering, Geological, and Other Applications. McGraw-Hill, New York, United States, 325 p.

Kane D.L., Hinkel K.M., Goering D.J., Hinzman, L.D. et Outcalt, S.I. (2001). Non-conductive heat transfer associated with frozen soils, Global and Planetary Change 29, 275–292. [https://doi.org/10.1016/S0921-8181\(01\)00095-9](https://doi.org/10.1016/S0921-8181(01)00095-9)

Kanzari, I. (2019). Évaluation du potentiel des pompes à chaleur géothermique pour la communauté nordique de Kuujjuaq. Master thesis, Institut national de la recherche scientifique, Québec, Canada, 87 p.

Karanasios K., Parker P. (2016). Recent developments in renewable energy in remote aboriginal communities, Quebec, Canada, Canadian Economic Development 16. 98-108 <https://doi.org/10.15353/pced.v16i0>

Kavanaugh S.P., Rafferty K.D. (2014). Geothermal Heating and Cooling: Design of Ground-Source Heat Pump Systems, ASHRAE Research Project RP-1674, Atlanta, United States. 420 p.

Kativik (2022). Gasoline Program. Retrieved from: <http://www.krg.ca/en-CA/programs/nunavik-col/gasoline>

Kersten M.S. (1949). Thermal properties of soils. University of Minnesota, retrieved from the University of Minnesota Digital Conservancy, <https://hdl.handle.net/11299/124271>

Koubikana Pambou C.H., Raymond J., Lamarche L. (2019). Improving thermal response tests with wireline temperature logs to evaluate ground thermal conductivity profiles and groundwater fluxes, Heat and Mass Transfer 55, 1829-1843. <https://doi.org/10.1007/s00231-018-2532-y>

Langevin H., Giordano N., Raymond J., Gosselin L., Bourbonnais M. (2021). Design considerations for thermal energy storage systems in subarctic climate. Proceedings of 2nd Canadian Geothermal Students Day, Winnipeg, Canada, 4 p.

Langevin, H., Giordano, N., Raymond, J. (2022). Oscillatory thermal response test using heating cables: A novel method for in-situ thermal property analysis. [submitted]

Le Roux D., Bourbonnais M., Déry P., Rousse D.R. (2019). Modélisation et simulations technico-économiques comparatives du chauffage solaire de l'eau par des capteurs photovoltaïque et thermique. XIVème Colloque International Franco-Québécois sur l'Énergie : Énergies durables (CIFQ2019). Baie St-Paul, Canada, 6 p.

Maranghi F., Gosselin L., Raymond J., Bourbonnais M. (2022), Modeling of solar assisted ground-coupled heat pumps with or without batteries in remote high north communities, Québec, Canada. [submitted]

Márquez M.I.V., Raymond J., Blessent D., Philippe M., Simon N., Bour O., Lamarche L. (2018). Distributed thermal response tests using a heating cable and fiber optic temperature sensing. Energies 11, (3059), 24 p. <https://doi:10.3390/en11113059>

McKenzie, J.M., Voss, C.I., Siegel, D.I. (2007). Groundwater flow with energy transport and water-ice phase change: numerical simulations, benchmarks, and application to freezing in peat bogs, Advances in water resources journal 30, 966-983. <https://doi.org/10.1016/j.advwatres.2006.08.008>

Natural Resources Canada (2012). Heating with Oil, Office of Energy Efficiency, Ottawa, Canada. 65 p.

Oberdorfer P. (2014). Heat transport phenomena in shallow geothermal boreholes: Development of a numerical model and a novel extension for the thermal response test method by applying oscillating excitations. PhD thesis, Georg-August University School of Science, Göttingen, Germany.

Paquet A., Cloutier G., Blais M. (2021). Renewable Energy as a Catalyst for Equity? Integrating Inuit Interests With Nunavik Energy Planning. Urban Planning 6 (4), 338-350. <https://doi.org/10.17645/up.v6i4.4453>

Pasquier P. (2018). Interpretation of the first hours of a thermal response test using the time derivative of the temperature. Applied Energy 213, 56–75. <https://doi.org/10.1016/j.apenergy.2018.01.022>

PVGIS (2022). PVGIS data sources & calculation methods. Retrieved from: [https://joint-research-centre.ec.europa.eu/pvgis-photovoltaic-geographical-information-system/getting-started-pvgis/pvgis-data-sources-calculation-methods\\_en](https://joint-research-centre.ec.europa.eu/pvgis-photovoltaic-geographical-information-system/getting-started-pvgis/pvgis-data-sources-calculation-methods_en)

Raymond J., Therrien R., Gosselin L., Lefebvre R. (2011). A Review of Thermal Response Test Analysis Using Pumping Test Concepts. *Ground Water* 49, 932–945. <https://doi.org/10.1111/j.1745-6584.2010.00791.x>

Raymond J., Lamarche L., Malo M. (2015). Field demonstration of a first thermal response test with a low power source. *Applied Energy* 147, 30–39. <https://doi.org/10.1016/j.apenergy.2015.01.117>

Raymond J., Giordano N., Langevin H. (2020). CAN Patent No. 63257740018521070.

REQ (2022). Bulletin d'information sur les prix des produits pétrolier au Québec 25 (22), Quebec City, Canada, 6 p.

Robur (2014). Submittal data GAHP line W LB series. Retrieved from, [https://www.roburcorp.com/heat\\_pumps/water\\_to\\_water\\_gas\\_absorption\\_heat\\_pump\\_gahp\\_w\\_lb](https://www.roburcorp.com/heat_pumps/water_to_water_gas_absorption_heat_pump_gahp_w_lb)

Rodon T., Nachet L., Krolik C., Palliser T. (2021). Building energy sovereignty through community-based projects in Nunavik, *Sustainability* 13(16), 9061, 13 p. <https://doi.org/10.3390/su13169061>

Senate of Canada (2014). Standing Committee on Energy, the Environment and Natural Resources, Evidence, 2<sup>nd</sup> Session, 41<sup>st</sup> Parliament, 29 April.

Skarphagen, H., Banks, D., Frengstad, B.S., Gether H. (2019). Design Considerations for Borehole Thermal Energy Storage (BTES): A review with emphasis on convective heat transfer, *Geofluids*, 26 p. <https://doi.org/10.1155/2019/4961781>

Tarnawski V.R., Momose T., Leong W.H., Boveseccchi G., Coppa P. (2009). Thermal conductivity of standard sands. Part I. Dry-state conditions. *International Journal of Thermophysics* 30, 949–968. <https://doi.org/10.1007/s10765-009-0596-0>

Ukrainczyk N. (2009). Thermal diffusivity estimation using numerical inverse solution for 1d heat conduction. *International journal of heat and mass transfer* 52, 5675–5681. <https://doi.org/10.1016/j.ijheatmasstransfer.2009.07.029>

Witte H.J.L. (2013). Error analysis of thermal response tests. *Applied Energy* 109, 302-311. <https://doi.org/10.1016/j.apenergy.2012.11.060>

Xu, M., Eckstein, Y. (1995). Use of weighted least-squares method in evaluation of the relationship between dispersivity and field scale, *Ground Water* 33, 905-908. <https://doi.org/10.1111/j.1745-6584.1995.tb00035.x>

Yun T.S., Santamarina J.C. (2008). Fundamental study of thermal conduction in dry soils. *Granular Matter* 10, 197–207. <https://doi.org/10.1007/s10035-007-0051-5>

Zhang B., Gu K., Shi B., Liu C., Bayer P., Wei G., Gong X., Yang L. (2020). Actively heated fiber optics based thermal response test: A field demonstration. Renewable and Sustainable Energy Reviews 134, 11 p. <https://doi.org/10.1016/j.rser.2020.110336>

## **IV. Annexes**

## Annexe I - Numerical models calibration

Temperature simulated with numerical models needs to be compared to the observed temperature recorded with sensors to calibrate the simulations. However, there is uncertainty where to recover the simulated temperature with respect to the thermal storage of the temperature sensors and the heat source position since the sensors have a significant volume compared to the heating cable diameter. C-TRTs were performed for each material tested (Fig.I.1) and data was used for the calibration since  $\lambda$  analytically solved is accurate ( $\delta\lambda < 1\%$ ).

The ILS approximation used to estimate  $\lambda$  from the C-TRT data is only valid for the time criterion  $t > 5r_{cbl}^2/\alpha$ , which is as low as  $t > 3$  min for  $r_{cbl} = 2.86$  mm in a material such as the OS ( $\alpha = 0.232 \text{ mm}^2 \text{ s}^{-1}$ ). The C-TRT performed in OS injected heat at a constant rate of  $16 \text{ W m}^{-1}$  for 2 h (Fig.I.1). An averaged value of  $m$  of 4.867 for the heating period was estimated and an averaged  $\lambda = 0.259 \text{ W m}^{-1} \text{ K}^{-1}$  was calculated from the heating period with an error  $\delta\lambda = 0.8\%$  and standard deviation  $\sigma_\lambda = 0.006 \text{ W m}^{-1} \text{ K}^{-1}$  among the analyzed sensors.

The C-TRT lasted 9 h with an averaged power injected of  $16 \text{ W m}^{-1}$  (Fig.I.1).  $\lambda$  was evaluated via the heat injection period as there is negligible thermal resistance from the heating cable. An averaged  $m = 1.284$  was estimated according to the increments of temperature measured with the DST sensors over the natural logarithm time. The averaged  $\lambda$  value equals to  $0.988 \text{ W m}^{-1} \text{ K}^{-1}$ , with average  $\delta\lambda = 1.0\%$  and  $\sigma_\lambda = 0.098 \text{ W m}^{-1} \text{ K}^{-1}$ .

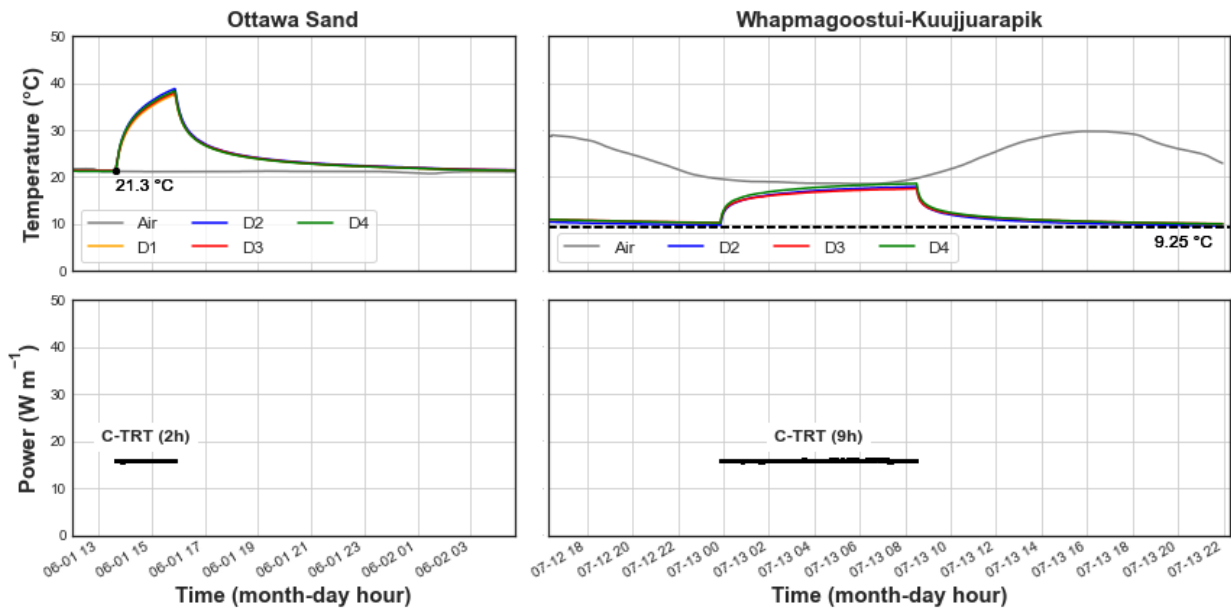


**Fig.I.1:** Temperature and power data recovered from the C-TRTs performed in the OS (left figures) and WK (right figures).

In order to properly represent the temperature recorded from a DST centi-T sensor, numerous simulations were done in 3D numerical models. 200 different scenarios were simulated for each C-TRT to calculate the optimal location at which simulated temperature have to be recovered. Temperature was recovered at 20 different locations (Figs.I.2 and I.3) and  $\rho C$  was varied at each location using 10 values ranging from  $0.75\text{-}1.20 \text{ MJ m}^{-3} \text{ K}^{-1}$  (constant steps of  $0.05 \text{ MJ m}^{-3} \text{ K}^{-1}$ ) for the OS case and from  $1.50\text{-}1.95 \text{ MJ m}^{-3} \text{ K}^{-1}$  (constant steps of  $0.05 \text{ MJ m}^{-3} \text{ K}^{-1}$ ) for the WK case. The averaged  $\lambda$  estimated from the C-TRTs ( $\lambda = 0.259 \text{ W m}^{-1} \text{ K}^{-1}$  for the OS case and  $\lambda = 0.988 \text{ W m}^{-1} \text{ K}^{-1}$  for the WK case) were used as fixed input parameter to the numerical models to reduce the number of simulations to perform. Temperature at the location for each scenario was recovered and the RMSE was calculated. The minimal calculated RMSE was considered the optimized location in the numerical model to recover the simulated temperature.

This calibration process shows that the optimized values for the C-TRT in the OS sand are  $\alpha = 0.235 \text{ mm}^2 \text{ s}^{-1}$ ,  $\rho C = 1.100 \text{ MJ m}^{-3} \text{ K}^{-1}$  and the distance to recover temperature from the heating cable =  $0.00947 \text{ m}$  (Fig.I.2). This distance is then used for the other numerical simulations of O-TRTs in the OS sand. The optimized values for the C-TRT in the WK material are  $\alpha = 0.520 \text{ mm}^2 \text{ s}^{-1}$ ,  $\rho C = 1.900 \text{ MJ m}^{-3} \text{ K}^{-1}$  and the distance to recover temperature from the heating cable =  $0.00789 \text{ m}$  (Fig.I.3). This distance is then used for the other numerical models simulating O-TRTs in the WK sand. The optimized distance from the heating cable is different for the OS and WK materials because heat is diffused at a rate characteristic to their respective investigated thermal properties values.

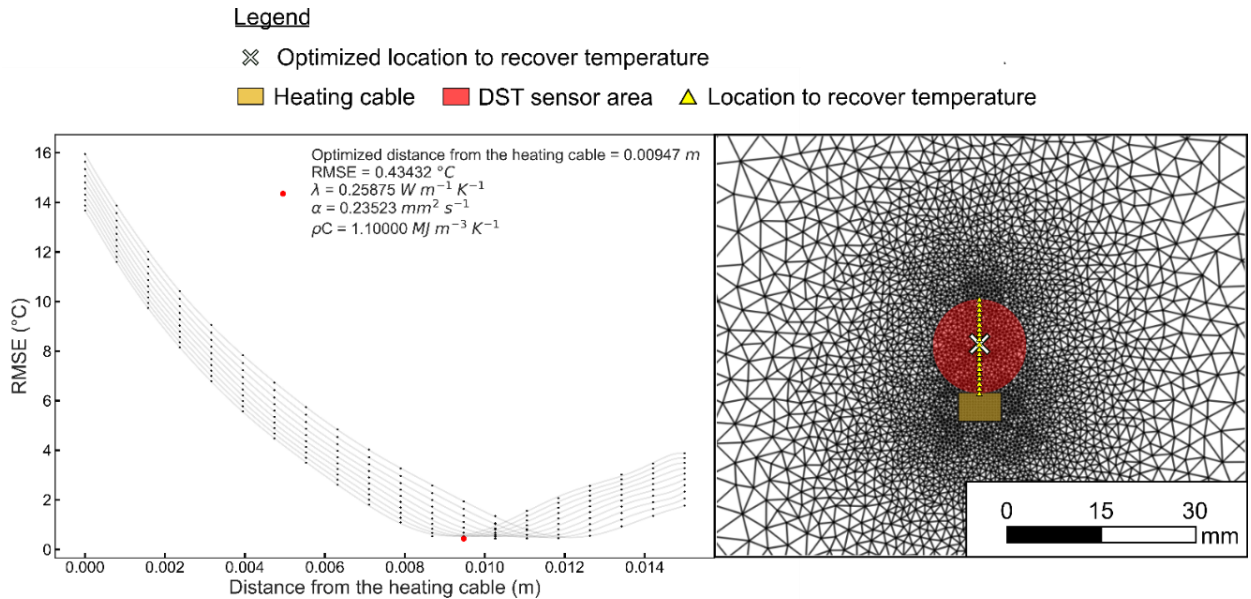


**Fig.I.2:** RMSE calculated at different distance from the heating cable in the OS C-TRT and optimized values.

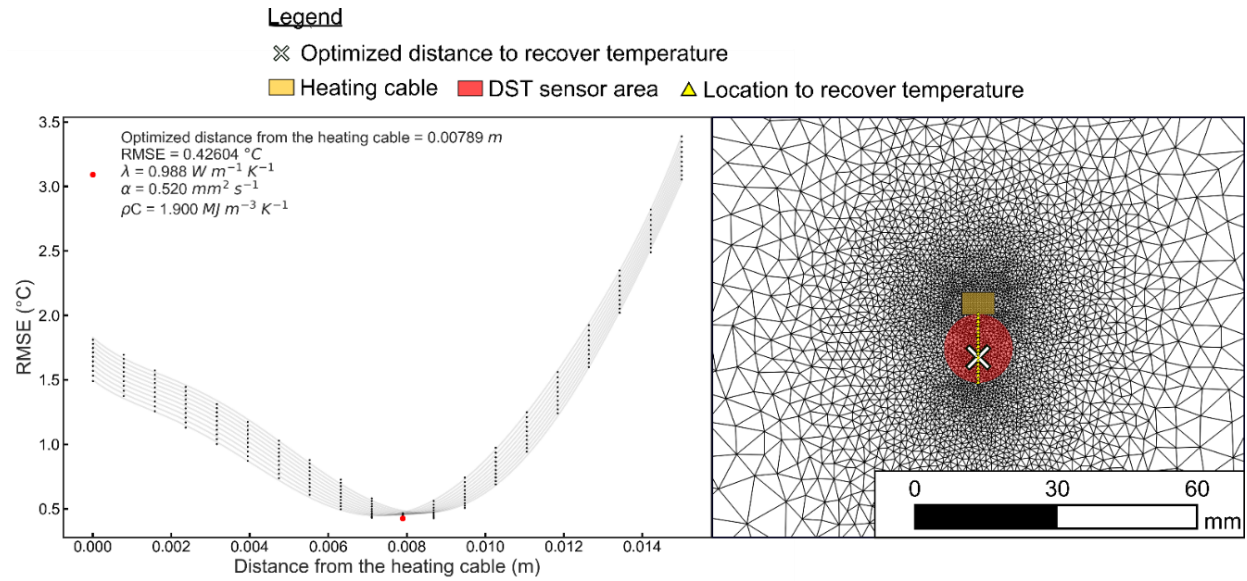


**Fig.I.3:** RMSE calculated at different distance from the heating cable in the WK sand C-TRT and optimized values.

## Annexe II – Analyses détaillées des essais de réponse thermique oscillatoires

**Table II.1 :** Results from the O-TRT analysis for the OS.

#	Sensor	$\bar{Q}$ (W m <sup>-1</sup> )	$Q_{Amp}$ (W m <sup>-1</sup> )	$t_0$ (h)	$\lambda$ (W m <sup>-1</sup> K <sup>-1</sup> )	$\delta\lambda$ (%)	$\alpha$ (mm <sup>2</sup> s <sup>-1</sup> )	$\delta\alpha$ (%)	$\rho C$ (MJ m <sup>-3</sup> K <sup>-1</sup> )	$\delta\rho C$ (%)	$\phi$ (rad)	$R_{osc}$ (°C)	$rp$ (-)
<b>O-TRT-1</b>	D1	12.8	2.6	4	0.227	1.7	0.224	5.3	1.012	5.6	0.114	0.618	0.126
	D2				0.243	1.6	0.254	5.3	0.958	5.6	0.109	0.672	0.118
	D3				0.252	1.6	0.241	5.3	1.045	5.6	0.111	0.644	0.121
	D4				0.237	1.6	0.247	5.3	0.958	5.6	0.110	0.630	0.120
<b>O-TRT-2</b>	D1	11.9	4	4	0.237	1.0	0.214	5.3	1.109	5.4	0.116	0.668	0.126
	D2				0.243	0.9	0.247	5.3	0.984	5.4	0.110	0.721	0.120
	D3				0.249	0.9	0.224	5.3	1.112	5.4	0.114	0.693	0.126
	D4				0.240	0.9	0.224	5.3	1.072	5.4	0.114	0.676	0.126
<b>O-TRT-3</b>	D1	10.5	5.3	4	0.229	1.0	0.241	5.3	0.952	5.4	0.111	0.649	0.121
	D2				0.236	0.8	0.274	5.3	0.862	5.4	0.106	0.703	0.114
	D3				0.242	0.8	0.260	5.3	0.932	5.4	0.108	0.673	0.117
	D4				0.233	0.8	0.253	5.3	0.921	5.4	0.109	0.655	0.118
<b>O-TRT-4</b>	D1	12.7	2.8	6	0.228	1.0	0.190	5.3	1.198	5.4	0.104	0.773	0.111
	D2				0.237	0.8	0.205	5.3	1.155	5.4	0.102	0.813	0.107
	D3				0.255	0.9	0.190	5.3	1.340	5.4	0.104	0.738	0.111
	D4				0.236	0.9	0.177	5.3	1.332	5.4	0.107	0.747	0.116
<b>O-TRT-5</b>	D1	11.7	4.2	6	0.229	1.3	0.211	5.3	1.087	5.5	0.101	0.775	0.106
	D2				0.244	1.2	0.228	5.3	1.069	5.4	0.098	0.803	0.102
	D3				0.253	1.2	0.228	5.3	1.108	5.4	0.098	0.734	0.102
	D4				0.237	1.1	0.205	5.3	1.154	5.4	0.101	0.745	0.107
<b>O-TRT-6</b>	D1	10.7	5.5	6	0.232	1.4	0.211	5.3	1.102	5.5	0.101	0.785	0.106
	D2				0.250	1.5	0.228	5.3	1.096	5.5	0.098	0.812	0.102
	D3				0.259	1.4	0.222	5.3	1.166	5.5	0.099	0.743	0.103
	D4				0.241	1.3	0.205	5.3	1.174	5.4	0.102	0.754	0.107
<b>O-TRT-7</b>	D1	13	2.6	12	0.223	1.0	0.232	5.3	0.960	5.4	0.078	1.036	0.071
	D2				0.208	1.3	0.232	5.3	0.896	5.4	0.078	1.066	0.071
	D3				0.210	1.4	0.212	5.3	0.989	5.5	0.080	0.977	0.075
	D4				0.222	1.0	0.212	5.3	1.046	5.4	0.080	1.001	0.075
<b>O-TRT-8</b>	D1	11.8	3.9	12	0.260	1.3	0.216	5.3	1.206	5.5	0.080	0.971	0.074
	D2				0.215	1.1	0.249	5.3	0.865	5.4	0.077	0.992	0.069
	D3				0.214	1.0	0.229	5.3	0.935	5.4	0.079	0.913	0.072
	D4				0.249	1.1	0.211	5.3	1.178	5.4	0.080	0.936	0.075
<b>O-TRT-9</b>	D1	10.7	5.4	12	0.254	1.9	0.225	5.3	1.131	5.7	0.079	0.963	0.073
	D2				0.210	1.5	0.239	5.3	0.880	5.5	0.078	0.989	0.070
	D3				0.209	1.2	0.225	5.3	0.931	5.4	0.079	0.909	0.073
	D4				0.241	1.2	0.212	5.3	1.139	5.4	0.080	0.933	0.075

**Table II.2:** Results from the O-TRT analysis for the WK.

#	Sensor	$\bar{Q}$ (W m <sup>-1</sup> )	$Q_{Amp}$ (W m <sup>-1</sup> )	$t_0$ (h)	$\lambda$ (W m <sup>-1</sup> K <sup>-1</sup> )	$\delta\lambda$ (%)	$\alpha$ (mm <sup>2</sup> s <sup>-1</sup> )	$\delta\alpha$ (%)	$\rho C$ (MJ m <sup>-3</sup> K <sup>-1</sup> )	$\delta\rho C$ (%)	$\phi$ (rad)	$R_{osc}$ (°C)	$rp$ (-)
<b>O-TRT-10</b>	D2	12.9	2.5	2	0.744	2.2	0.518	5.6	1.436	6.0	0.108	0.215	0.117
	D3				0.832	2.5	0.453	5.6	1.835	6.2	0.114	0.190	0.125
	D4				0.735	2.2	0.518	5.6	1.419	6.0	0.108	0.227	0.117
	D2				0.8	1.9	0.486	5.5	1.645	5.8	0.111	0.225	0.121
<b>O-TRT-11</b>	D3	12.1	3.8	2	0.898	2.0	0.428	5.5	2.098	5.9	0.116	0.198	0.129
	D4				0.797	1.9	0.486	5.5	1.639	5.8	0.111	0.236	0.121
	D2				0.838	1.8	0.578	5.5	1.449	5.8	0.104	0.241	0.111
	D3				0.914	2.0	0.578	5.6	1.580	6.0	0.104	0.219	0.111
<b>O-TRT-12</b>	D4	11	5.4	2	0.825	1.7	0.578	5.5	1.426	5.8	0.104	0.252	0.111
	D2				0.832	1.6	0.463	5.4	1.797	5.6	0.088	0.278	0.087
	D3				0.893	1.6	0.385	5.4	2.322	5.7	0.094	0.242	0.096
	D4				0.82	1.5	0.512	5.4	1.601	5.6	0.086	0.296	0.083
<b>O-TRT-13</b>	D2	13.1	2.3	4	0.881	1.5	0.448	5.4	1.976	5.6	0.079	0.322	0.073
	D3				0.917	1.6	0.508	5.5	1.768	5.7	0.076	0.278	0.068
	D4				0.857	1.5	0.508	5.4	1.673	5.6	0.076	0.342	0.068
	D4												

**Table II.3:** Correction factors calculated for O TRTs performed in the OS.

#	Sensor	$\bar{Q}$ (W m <sup>-1</sup> )	$Q_{Amp}$ (W m <sup>-1</sup> )	$t_0$ (h)	$F_\lambda$ (-)	$F_a$ (-)
<b>O-TRT-1</b>	D1	12.8	2.6	4	1.123	1.034
	D2				1.049	0.914
	D3				1.012	0.962
	D4				1.076	0.938
<b>O-TRT-2</b>	D1	11.9	4	4	1.076	1.085
	D2				1.049	0.939
	D3				1.024	1.036
	D4				1.063	1.036
<b>O-TRT-3</b>	D1	10.5	5.3	4	1.114	0.964
	D2				1.081	0.847
	D3				1.054	0.893
	D4				1.094	0.917
<b>O-TRT-4</b>	D1	12.7	2.8	6	1.118	1.219
	D2				1.076	1.130
	D3				1.000	1.219
	D4				1.081	1.310
<b>O-TRT-5</b>	D1	11.7	4.2	6	1.114	1.101
	D2				1.045	1.016
	D3				1.008	1.016
	D4				1.076	1.130
<b>O-TRT-6</b>	D1	10.7	5.5	6	1.099	1.102

	D2				1.020	1.017	
	D3				0.985	1.045	
	D4				1.058	1.131	
	D1				1.143	0.999	
<i>O-TRT-7</i>	D2	13	2.6	12	1.226	0.999	
	D3				1.214	1.093	
	D4				1.149	1.093	
	D1				0.981	1.076	
<i>O-TRT-8</i>	D2	11.8	3.9	12	1.186	0.933	
	D3				1.192	1.014	
	D4				1.024	1.098	
	D1				1.004	1.033	
<i>O-TRT-9</i>	D2	10.7	5.4	12	1.214	0.972	
	D3				1.220	1.033	
	D4				1.058	1.096	

**Table II.4:** Results from the O-TRT numerical simulations for the OS.

#	$\bar{Q}$ (W m <sup>-1</sup> )	$Q_{\text{Amp}}$ (W m <sup>-1</sup> )	$t_0$ (h)	$\lambda$ (W m <sup>-1</sup> K <sup>-1</sup> )	$\alpha$ (mm <sup>2</sup> s <sup>-1</sup> )	$\rho C$ (MJ m <sup>-3</sup> K <sup>-1</sup> )	$\phi$ (rad)	$R_{\text{osc}}$ (°C)	$rp$ (-)
<i>O-TRT-1</i>	12.8	2.6	4	0.259	0.234	1.115	0.112	0.744	0.123
<i>O-TRT-2</i>	11.9	4.0	4	0.259	0.232	1.106	0.113	0.742	0.124
<i>O-TRT-3</i>	10.5	5.3	4	0.259	0.241	1.077	0.111	0.751	0.121
<i>O-TRT-4</i>	12.7	2.8	6	0.258	0.231	1.127	0.098	0.842	0.101
<i>O-TRT-5</i>	11.7	4.2	6	0.258	0.239	1.071	0.096	0.851	0.100
<i>O-TRT-6</i>	10.5	5.5	6	0.256	0.236	1.084	0.097	0.854	0.100
<i>O-TRT-7</i>	13.0	2.6	12	0.260	0.232	1.124	0.078	1.018	0.071
<i>O-TRT-8</i>	11.8	3.9	12	0.261	0.236	1.102	0.078	1.019	0.071
<i>O-TRT-9</i>	10.7	5.4	12	0.258	0.239	1.078	0.078	1.034	0.070

**Table II.5:** Results from the O-TRT numerical simulations for the WK.

#	$\bar{Q}$ (W m <sup>-1</sup> )	$Q_{\text{Amp}}$ (W m <sup>-1</sup> )	$t_0$ (h)	$\lambda$ (W m <sup>-1</sup> K <sup>-1</sup> )	$\alpha$ (mm <sup>2</sup> s <sup>-1</sup> )	$\rho C$ (MJ m <sup>-3</sup> K <sup>-1</sup> )	$\phi$ (rad)	$R_{\text{osc}}$ (°C)	$rp$ (-)
<i>O-TRT-10</i>	12.9	2.5	2	1.137	0.635	1.792	0.101	0.186	0.106
<i>O-TRT-11</i>	12.1	3.8	2	0.895	0.515	1.735	0.108	0.222	0.118
<i>O-TRT-12</i>	11.0	5.4	2	0.895	0.521	1.721	0.108	0.223	0.117
<i>O-TRT-13</i>	13.6	2.3	4	0.986	0.557	1.764	0.084	0.253	0.080
<i>O-TRT-14</i>	13.1	2.4	6	0.915	0.500	1.834	0.077	0.295	0.069

### Annexe III – Subsurface georadar assessment at the CEN research station

A common midpoint (CMP) and two reflection ground penetrating radar (GPR) survey lines were conducted at the CEN research station in 2019 to investigate subsurface structures (Fig.III.1). This geophysical method using high frequency electromagnetic impulsion waves was carried out in order to estimate the lithologies and bedrock elevation or other relevant information. Surveys were performed at a 200 MHz nominal frequency with a 0.5 m antenna separation and 0.1 m step size.

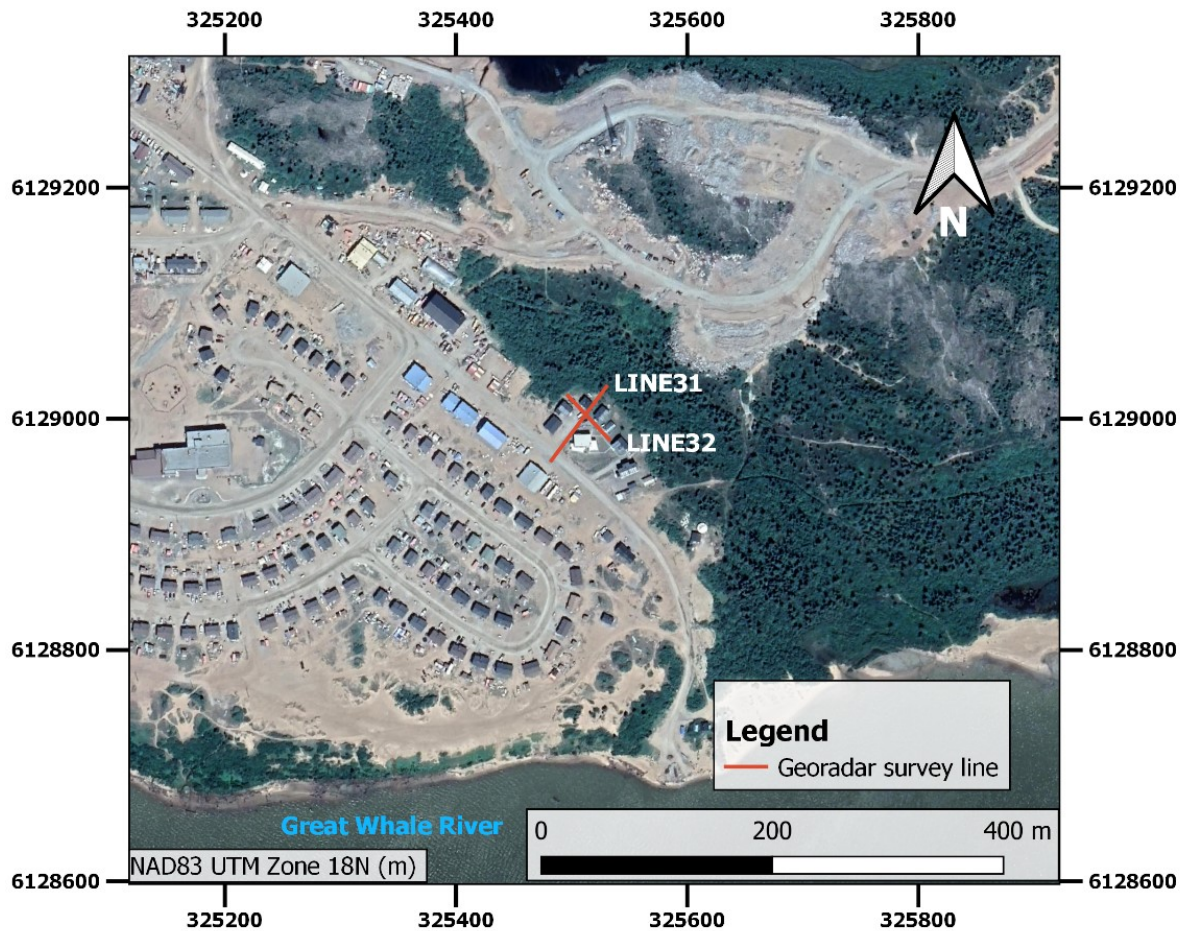


**Fig.III.1:** Location of the GPR survey lines at the CEN research station.

The CMP test allowed to estimate electromagnetic waves speed of 0.14 to 0.15 m ns<sup>-1</sup> and corresponds to a dry silty sand material (Fig.III.2a). The northern part of Line 31 is characterized by two elevated ground steps from 10 to 30 m on the profile position (Fig.III.2b), while Line 32 have few elevations variation (Fig.III.2c). Cross-sections show a stratified silty sand material without noticeable structures buried. Stratified material is mainly preserved until a -10 to -5 m elevation. This signal contrast can either be a clear water content variation, a lithological contrast or the attenuation of the emitted signal. It is assumed that this contrast is the bedrock elevation since it corresponds to what it is expected according to outcropping bedrock

and observed stratigraphy of the wells in the vicinity of the CEN. The silty sand layer is therefore 15 to 20 m thick at the CEN research station.

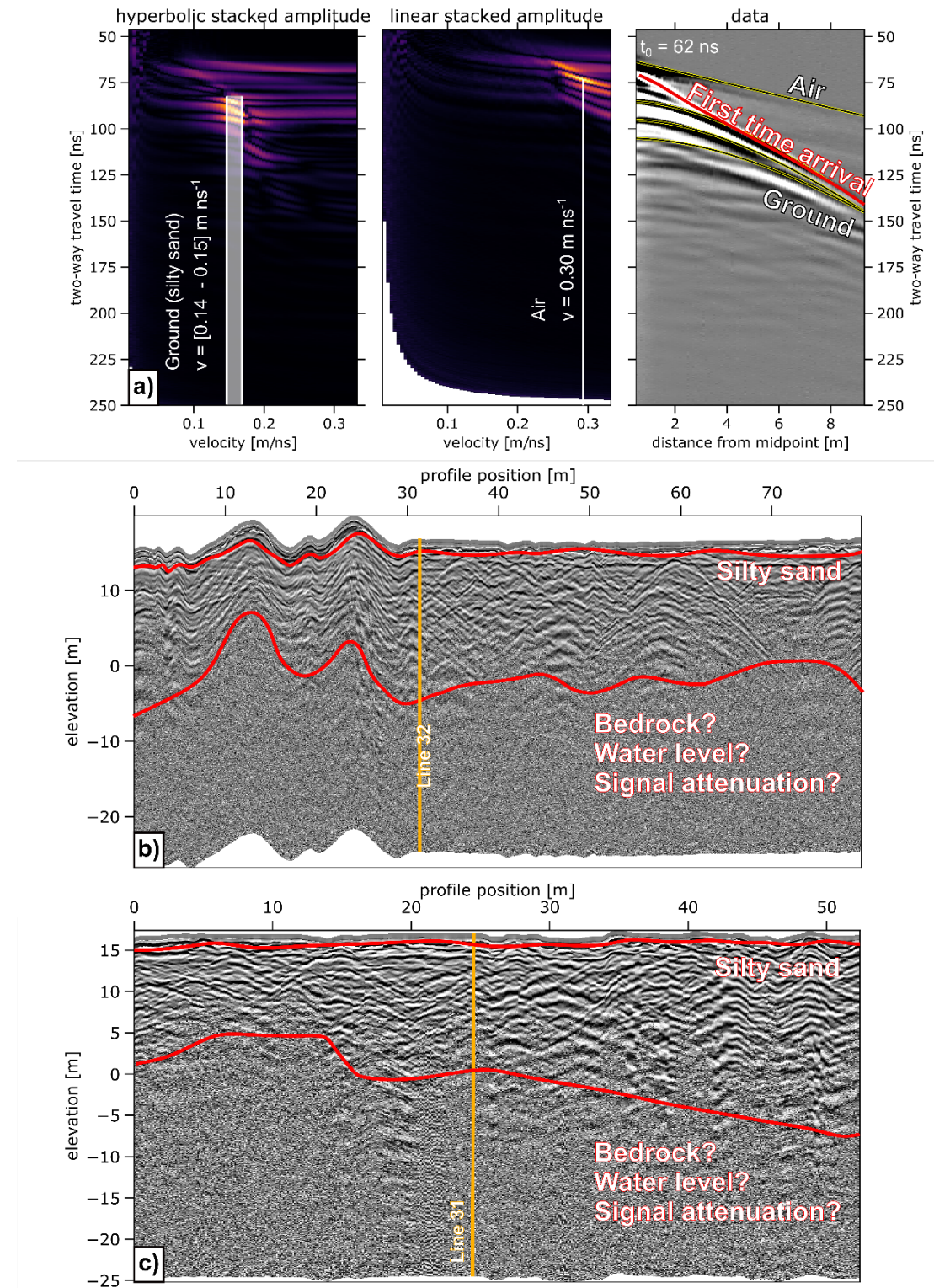


**Fig.III.2:** Common midpoint and reflection analysis at the CEN research station.

## Annexe IV – Regional hydrogeological numerical model

The site under study is characterized by a hydrogeological context without permafrost and influenced by the Hudson Bay, the Great Whale River, regional water bodies, major structural lineaments and groundwater pumping (CIMA+, 2014). In order to take into account the different factors influencing groundwater velocities in the region, a 3D regional groundwater flow model was developed with unconfined aquifer conditions and two distinct materials: unconsolidated sediments and bedrock. To represent these materials in the numerical model, the top of the unconsolidated sediments layer corresponds to the regional surface topography, while the top of the bedrock corresponds to the interpolation of the measured bedrock depth in the observation wells and its extrapolation. Five different major vertical 1-m width lineaments in bedrock were also implemented in the model because it has been noted by Géophysique GPR International inc. (2002) and CIMA+ (2014) that major structural lineaments were influencing the regional groundwater flow as they have higher homogenous and isotropic hydraulic conductivity and porosity than its host bedrock. The model maximal elevation is 114 m above sea level, while the base of the model is at a -200 m elevation. The southern and western part of the model is bordered by the Hudson Bay and the Great Whale River. The eastern and northern part of the model are bordered by topographic lows were not influenced by the groundwater extraction at the pumping wells and where the groundwater flow is considered symmetric along the borders.

Model dimensions are 5,826 m × 3,555 m × 315 m in the  $x$ ,  $y$  and  $z$  directions, respectively. Numerical models were resolved into 2,466,100 nodes with 4,574,609 lateral prismatic triangular elements ranging from a maximum of  $\approx 200.0$  m (edge of the Hudson Bay) and a minimum of 0.1 m (around the pumping wells). Also, mesh is refined to a minimal 1-m distance between nodes around the faults because of high hydraulic properties contrasts. Vertical element dimensions are distributed within 14 slices ranging from 1 m to  $\approx 30$  m (Fig.IV.1a).

An annual groundwater recharge of  $162.2 \text{ mm yr}^{-1}$  was estimated for the Whapmagoostui-Kuujjuarapik region considering rain and snow precipitations, surface runoff and evapotranspiration according to CIMA+ (2014) and set at the top of the model. The northern eastern border was considered symmetrical (Neumann BC of  $0 \text{ m s}^{-1}$ ), while the bottom of the model was impermeable (Neumann BC of  $0 \text{ m s}^{-1}$ ). The western and south borders were considered at sea level (Dirichlet BC of 0 m) neglecting tide effects. The water level of the main water bodies of the region was set to nodes (Dirichlet BC) according to their location and calculated elevation in a digital elevation model (DEM). Two water levels close to pumping wells were monitored by CIMA+ during a pumping test performed in October 2012. Calculated flows at the nodes corresponding to the water bodies were considered according to their respective water level and a conductance parameter ( $K [\text{m s}^{-1}]$ /thickness [m]) of  $1.74 \times 10^{-5} \text{ s}^{-1}$  (Cauchy BC), which was

determined from the expected hydraulic conductivity and the average thickness of unconsolidated sediments beneath the water bodies. Multilayer wells (Diersch, 2014) were placed at location of pumping wells P1 and P2 to simulate a pumping test extracting water at a constant rate of  $899 \text{ m}^3 \text{ d}^{-1}$  and  $1,090 \text{ m}^3 \text{ d}^{-1}$ , respectively (Fig.IV.1b).

First, the steady-state groundwater flow was solved considering isotropic and homogeneous materials, BC conditions and topography (Fig.IV.2). Then, the solved hydraulic head and pressure were used as initial conditions to solve the steady-state groundwater flow with the influence of pumping wells P1 and P2. The numerical solution converged within three iterations with an error tolerance of  $10^{-3}$  between two iterations. The calculated differences between simulated and observed heads ( $\Delta h_{c-o}$ ) in 18 wells at the end of the 72 h pumping test were used to calibrate solved groundwater velocities according to the estimated  $v_1$  and  $v_2$  (Fig.IV.1b).  $K$  and  $q_i$  were varied until the  $\Delta h_{c-o}$  and the calculated root-mean squared error (RMSE) were minimized. Therefore, the ratio  $q_i/K$  was then calculated according to the Darcy Law (Eq.3.2) and  $v$  was evaluated at  $v_1$  and  $v_2$  locations. The calibration factors solved with Eqs.IV.1 and IV.2 were averaged and then  $K$  and  $q_i$  were multiplied to those factors to calibrate and adjust solved  $v$  to the groundwater velocities estimated by CIMA+, and thus keeping the ratio  $q_i/K$  to minimize the RMSE (Eqs.IV.3 and IV.4).

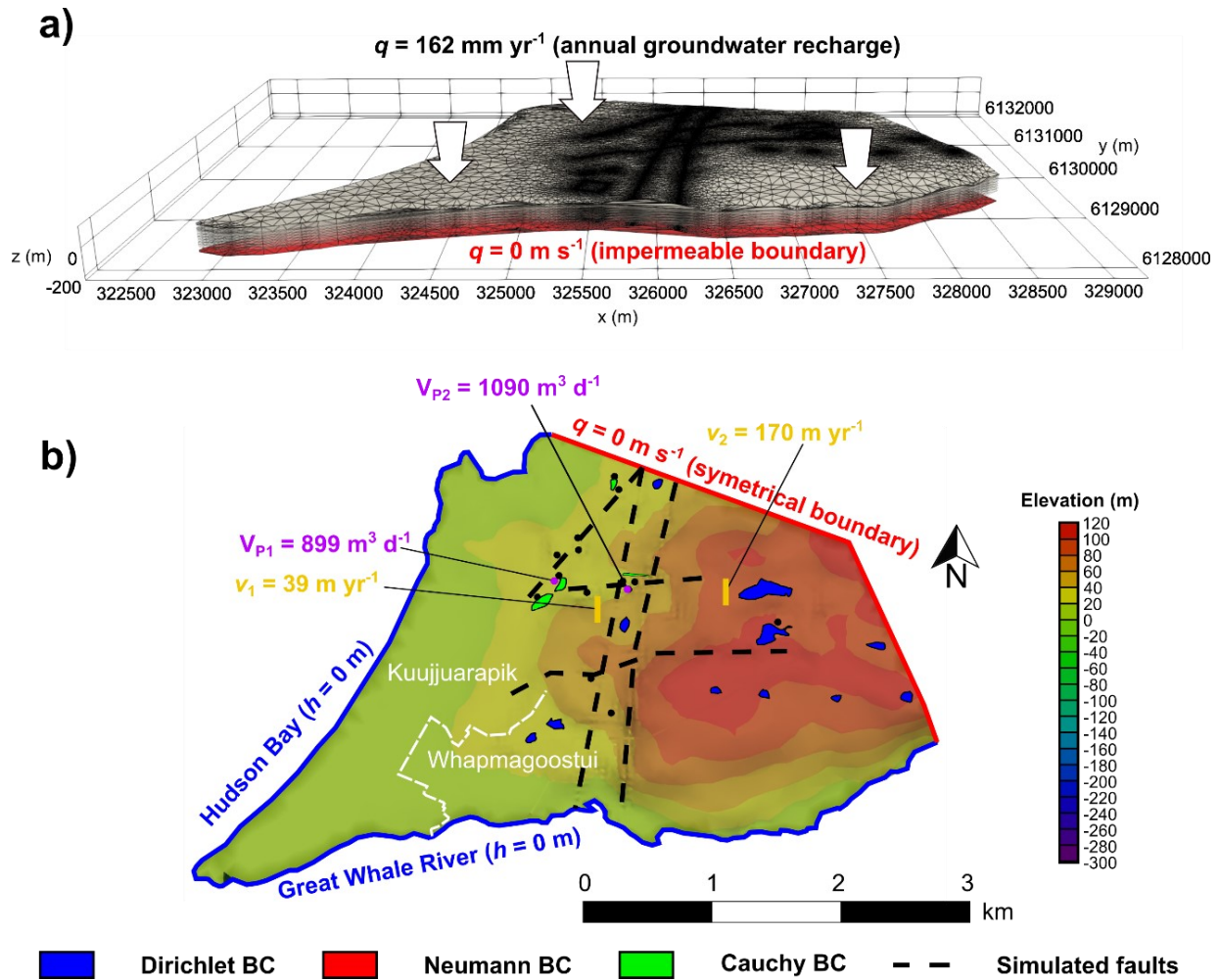


**Fig.IV.1:** a) 3D view of the mesh showing top and bottom boundary conditions of the regional groundwater numerical model b)  $x$ - $y$  top view showing the elevation, lateral and top boundary conditions of the regional groundwater numerical model.

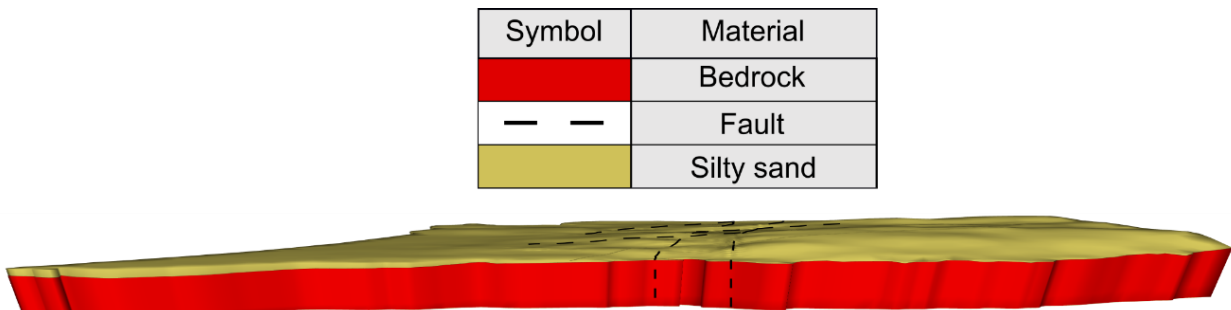


**Fig.IV.2:** Material properties of the regional groundwater numerical model.

$$Cal_1 = \frac{v_1}{v} \quad (\text{IV.1})$$

$$Cal_2 = \frac{v_2}{v} \quad (\text{IV.2})$$

$$K_{\text{calibrated}} = K \cdot \left( \frac{Cal_1 + Cal_2}{2} \right) \quad (\text{IV.3})$$

$$q_{i-\text{calibrated}} = q_i \cdot \left( \frac{Cal_1 + Cal_2}{2} \right) \quad (\text{IV.4})$$

The simulated drawdown at the end of the 72-h pumping test is shown on Fig.IV.5. The resulting annual groundwater recharge is equal to 182.5 mm yr<sup>-1</sup> and calibrated material properties values are shown in Fig.IV.3. Results of the simulated hydraulic heads with (Fig.IV.4) and without the influence of the P1 and P2 pumping wells at the end of the 72-h pumping test (Fig.IV.5). The drawdown caused by the pumping test is shown in Fig.IV.6.

Lithology	Property	Value	Property	Value
	$K_{\text{bedrock}} (\text{m s}^{-1})$	$5.78 \times 10^{-7}$	$\Theta_{\text{bedrock}}$ (-)	0.02
— —	$K_{\text{fault}} (\text{m s}^{-1})$	$1.45 \times 10^{-3}$	$\Theta_{\text{fault}}$ (-)	0.11
	$K_{\text{silty sand}} (\text{m s}^{-1})$	$2.89 \times 10^{-4}$	$\Theta_{\text{silty sand}}$ (-)	0.20

**Fig.IV.3:** Calibrated material properties of the regional groundwater numerical model.

A RMSE of 7.61 m was calculated according to the final calibration (Fig.IV.7). The maximal  $\Delta h_{c-o}$  were observed in the wells 75 m north of the P2 groundwater well, where substantial thickness of unconsolidated sediments deposit ( $\approx 20$  m) was observed. This difference can be explained by the fact that this deposit has irregular hydraulic properties with values significantly different from the whole region that, were not considered in the regional groundwater flow numerical model. Another irregularity was also observed in a well located 500 m south of the P2 groundwater well and 40 m north of two faults, where permeability of faults and fractures is unpredictable. The numerical solution underestimates the measured groundwater level because of the assumptions made on this part of the model misrepresents the conditions. However,  $\Delta h_{c-o}$  observed in the other wells were reasonably minimized with a RMSE of 4.43 m and solved groundwater velocities at the CEN station can be considered representative for the numerical models used in this study. Moreover, the estimated  $K_{\text{calibrated}}$  was validated as its value lies within a reasonable range of calculated values with a Guelph permeameter at different locations in the region in a field campaign done in 2021 (Fig.IV.8).

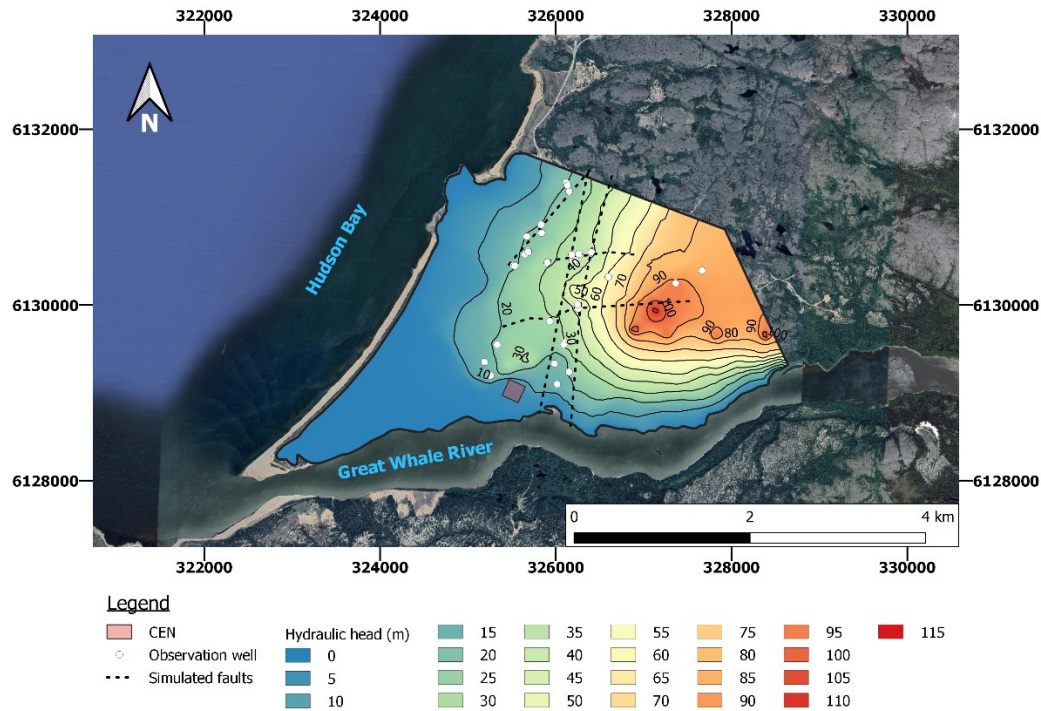


**Fig.IV.4:** Hydraulic head simulated without the influence of the P1 and P2 pumping wells for the regional numerical model.

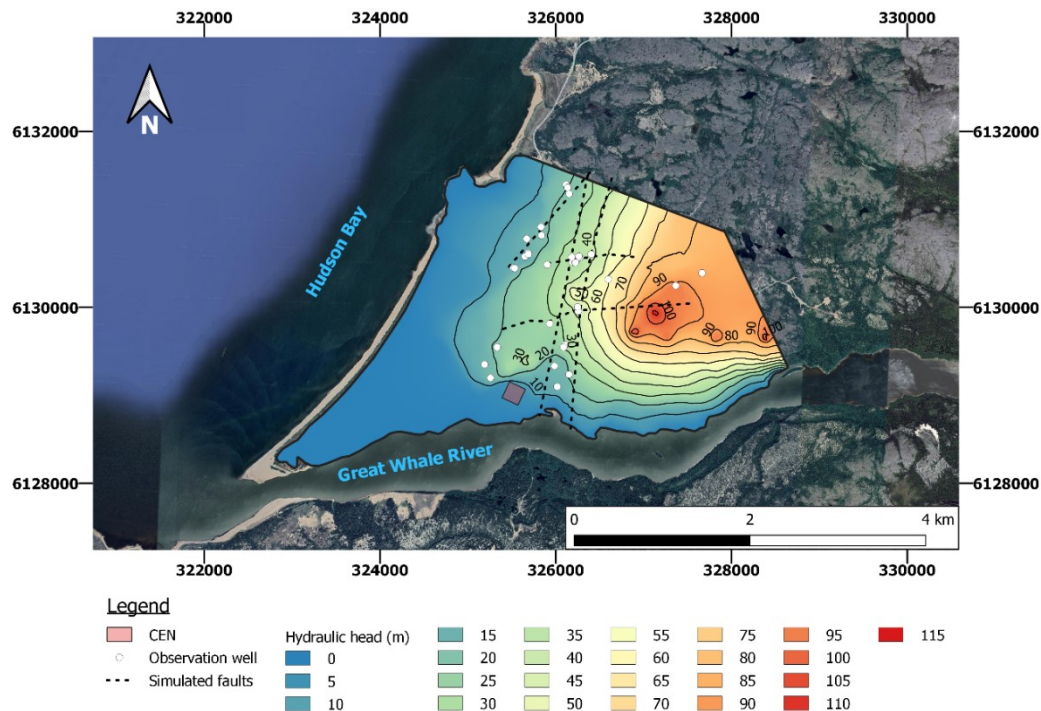


**Fig.IV.5:** Hydraulic head simulated with the influence of the P1 and P2 pumping wells for the regional numerical model.

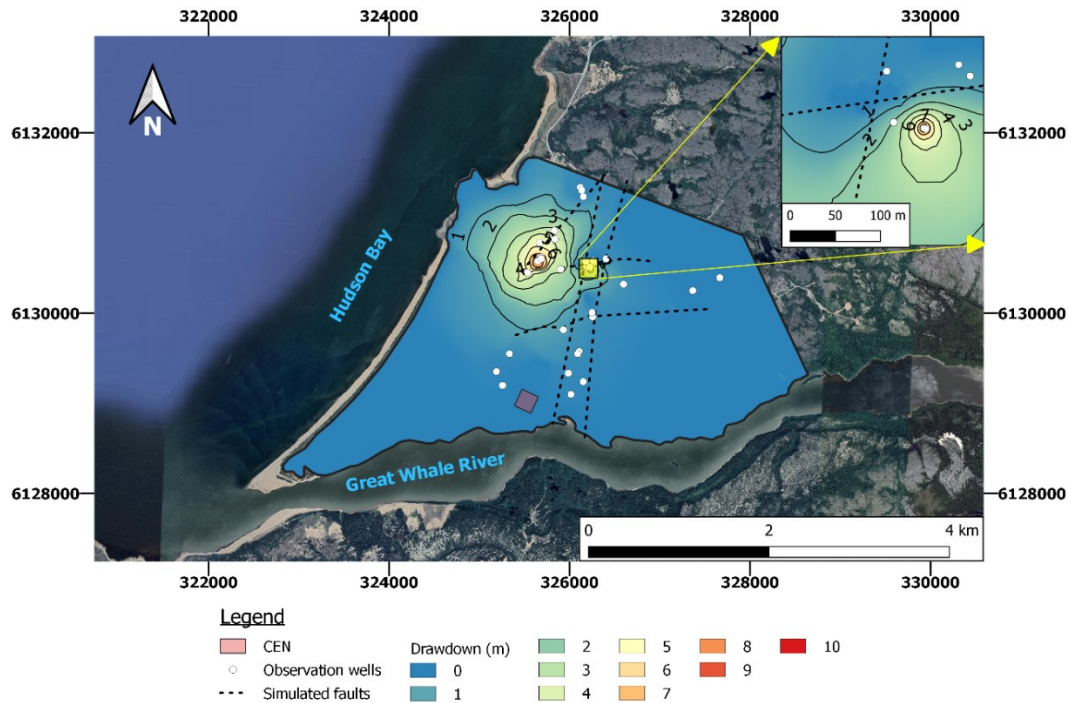


**Fig.IV.6:** Drawdown simulated at the end of the 72-h pumping test for the regional numerical model.

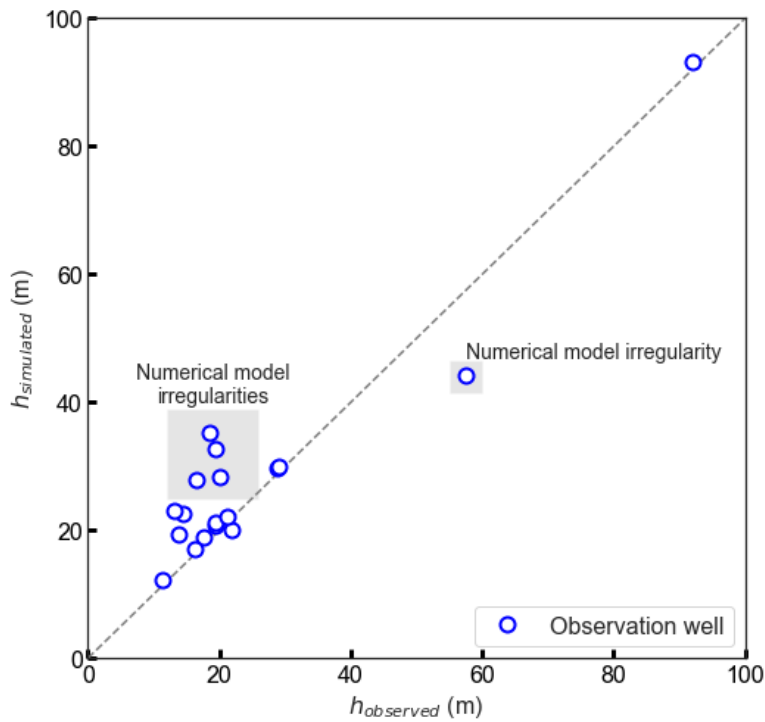


**Fig.IV.7:** Hydraulic head observed vs. simulated of the calibrated regional numerical model.

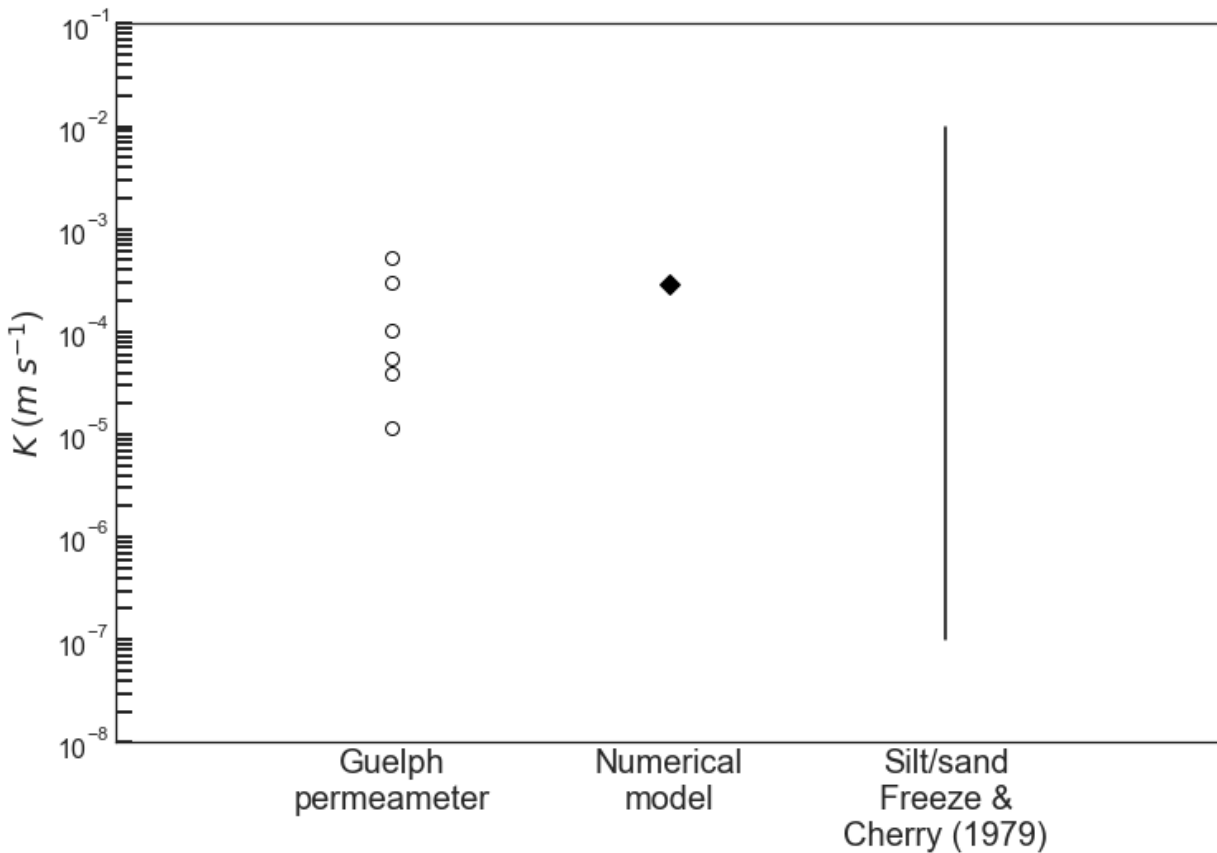


**Fig.IV.8:** Comparison of hydraulic conductivity measurements with the Guelph permeameter method, the numerically calibrated method, and the literature range of values for silt and sand (Freeze and Cherry, 1979).

Limitations of the numerical model can be listed as follows:

- It does not include ground heterogeneities within each material as well as bedrock fractures density and interconnection. Due to the regional scale of work, it is not possible to represent these aspects, which can however have a considerable influence on the local groundwater level.
- Groundwater recharge rate is applied uniformly on the numerical model while it is not necessarily so in the region.
- Feflow does not allow digital models with laterally discontinuous layers. Even though the thickness of the deposits has been reduced to less than 0.1 m and that this effect has been minimized, further errors can be related to this.
- Solved numerical models represents steady-state groundwater flow, while hydraulic head data during a pumping test is usually analyzed in transient state shortly after pumping begins. However, the hydraulic heads analyzed do not vary significantly after 48 h of pumping. Therefore, the assumption that the hydraulic heads analyzed after 72 h of pumping used for the calibration of the numerical model was in steady state is considered appropriate.

- Data to calibrate the model are concentrated near pumping wells P1 and P2 since the studies made by Geophysics GPR International inc. (2002) and CIMA+ (2014) aimed to ensure groundwater supply to the community. This induces a lower reliability of the model since there is an over-representation in one sector while there is a lower concentration of data elsewhere in the model. In addition, the model calibration is based on data located near the pumping wells, while it is likely that the rock in this sector is more fractured than elsewhere.

To improve the quality of the regional groundwater flow numerical model, it would be necessary to obtain more water level, bedrock surface and hydrogeological properties data elsewhere in the region and not only near wells P1 and P2. It is necessary to consider the limits of the model in order to interpret the simulated hydraulic heads and thus understand the modeled hydrogeological processes. On the other hand, the results obtained with this model are sufficient to simulate the thermal processes at CEN as the order of magnitude of the estimated values are reasonable. Therefore, this gives a reliable idea of the expected groundwater velocities at the CEN station.

## Annexe V – Ground temperature monitoring and assessment of the linear heat transfer coefficient

Air temperature recorded at the CEN's meteorological station from 1987 to 2016 (CEN, 2017) and ground temperature measured from 2018 to 2020 at 0.5, 0.7, 1.0 and 2.0 m depth were used to set a BC at the top of the numerical models. According to the ground temperature data, a layer of snow was assumed to be covering the ground surface during winter because temperature did not follow the typical sinusoidal pattern of the air temperature observed during winter (Fig.V.1).

In order to represent the insulating effect of the snow layer, a temperature of -1 °C was assumed at ground surface from 0 to 152 and from 304 to 365 days for a yearly temperature profile ( $T_{\text{ref}}$ ; Fig.V.1). Air temperature recorded at the CEN's meteorological station was averaged ( $T_{\text{air}}$ ; Fig.V.1) and assigned to  $T_{\text{ref}}$  from 152 to 304 days (Fig.V.1).  $T_{\text{ref}}$  was implemented in the UTES numerical model with a silty sand layer to determine a reasonable linear heat transfer coefficient  $l$  value, which was implemented in a Cauchy BC (Eq.V.1) at the top of the model.  $l_{\text{gr}}$  values ranging from 0.1 to 50 W m<sup>-2</sup> °C<sup>-1</sup> were assessed through different simulations and solved temperature at 0.5, 0.7, 1.0 and 2.0 m below ground level were compared to their corresponding measured temperature. According to the phase shift and the temperature amplitude, an  $l_{\text{gr}}$  value of to 20 W m<sup>-2</sup> °C<sup>-1</sup> allowed the best fit between solved and observed temperature values (Fig.V.2).

$$W_{\text{gr}} = \text{Area}_{\text{gr}} l_{\text{gr}} (T_{\text{ref}} - T_{\text{gr}}) \quad (\text{V.1})$$

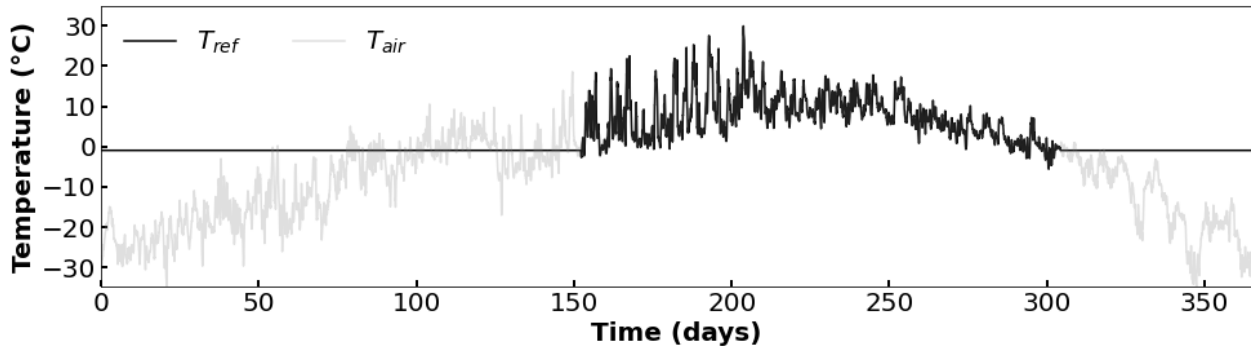


**Fig.V.1:** Temperature reference used to represent air temperature at top of the numerical models.

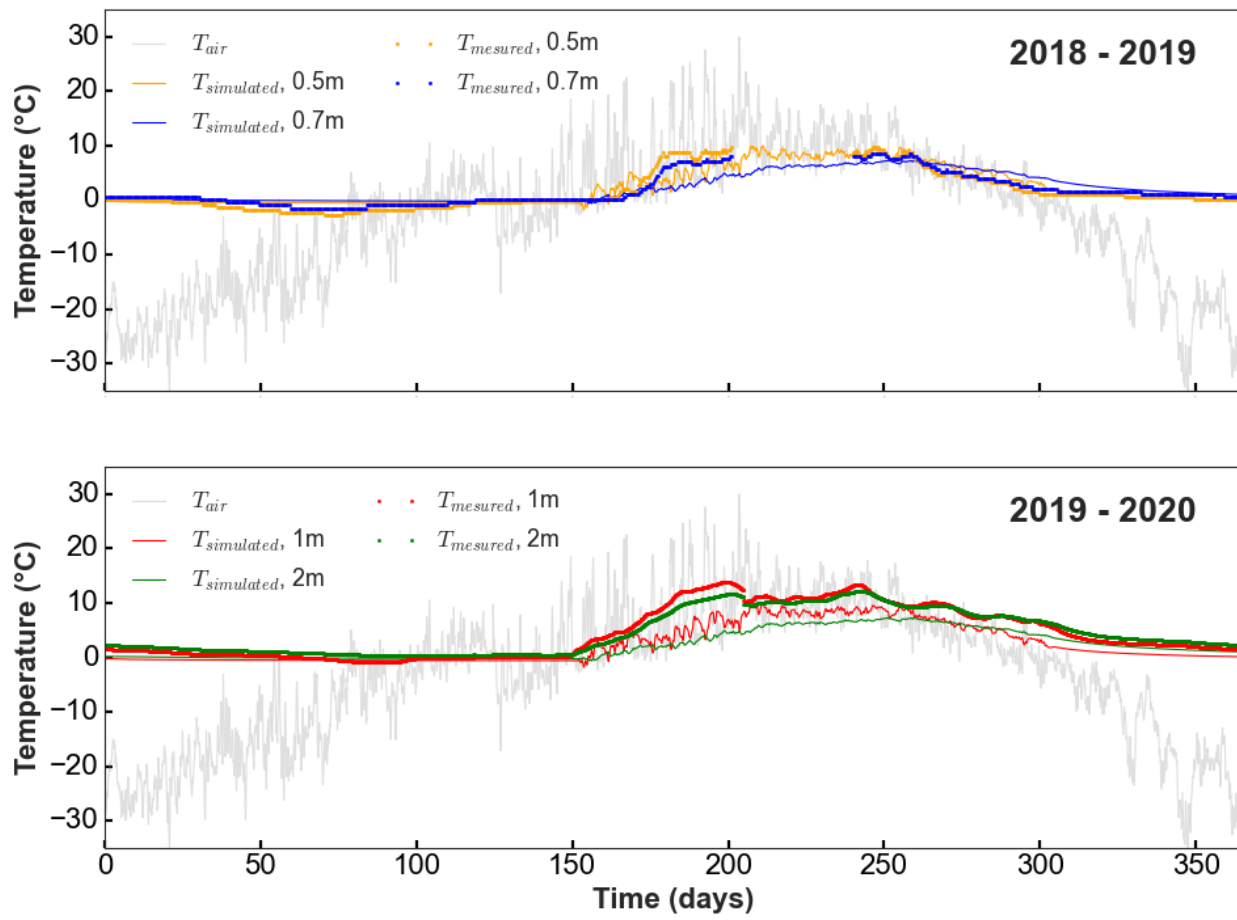


**Fig.V.2:** Comparison of the solved temperature with a linear heat transfer coefficient of  $20 \text{ W m}^{-2} \text{ }^{\circ}\text{C}^{-1}$  at a) 0.5 and 0.7 m where temperature was measured in 2018 to 2019, and b) 1.0 and 2.0 m where temperature was measured in 2019 to 2020.

## **Annexe VI –Thermal response test**

A constant-heat injection thermal response test (CTRT) was carried out near the CEN station in the TF05-12 well from a depth of 16 to 43 m with a 27-m heating cable. 19 temperature sensors placed along the cable (Fig.VI.1) allowed to estimate the in situ thermal conductivity of the bedrock (Raymond et al. 2015). The apparatus was set up as described in Fig.VI.1 and a temperature profile was performed after thermal equilibrium in the well was reached. Then, a heat injection rate of a  $17 \text{ W m}^{-1}$  was injected for 50 h and thermal recovery was measured for 62 h. Thermal recovery data for each temperature sensor were used to evaluate the in situ thermal conductivity with the slope method, which approximates the infinite line-source (ILS) equation (Carslaw and Jaeger 1947; Ingersoll et al. 1954). Three sets of temperature data (sensors #17 to #19) were neglected since the sensors were too close to the end of the cable and edge effects were important (Fig.VI.2). The calculated average effective thermal conductivity is  $2.68 \text{ W m}^{-1} \text{ K}^{-1}$  under groundwater flow influence. In order to extrapolate the thermal conductivity of the bedrock matrix without the influence of groundwater flow, the methodology described by Koubikana Pambou (2019) allowed to calculate a value of  $2.67 \text{ W m}^{-1} \text{ K}^{-1}$ .

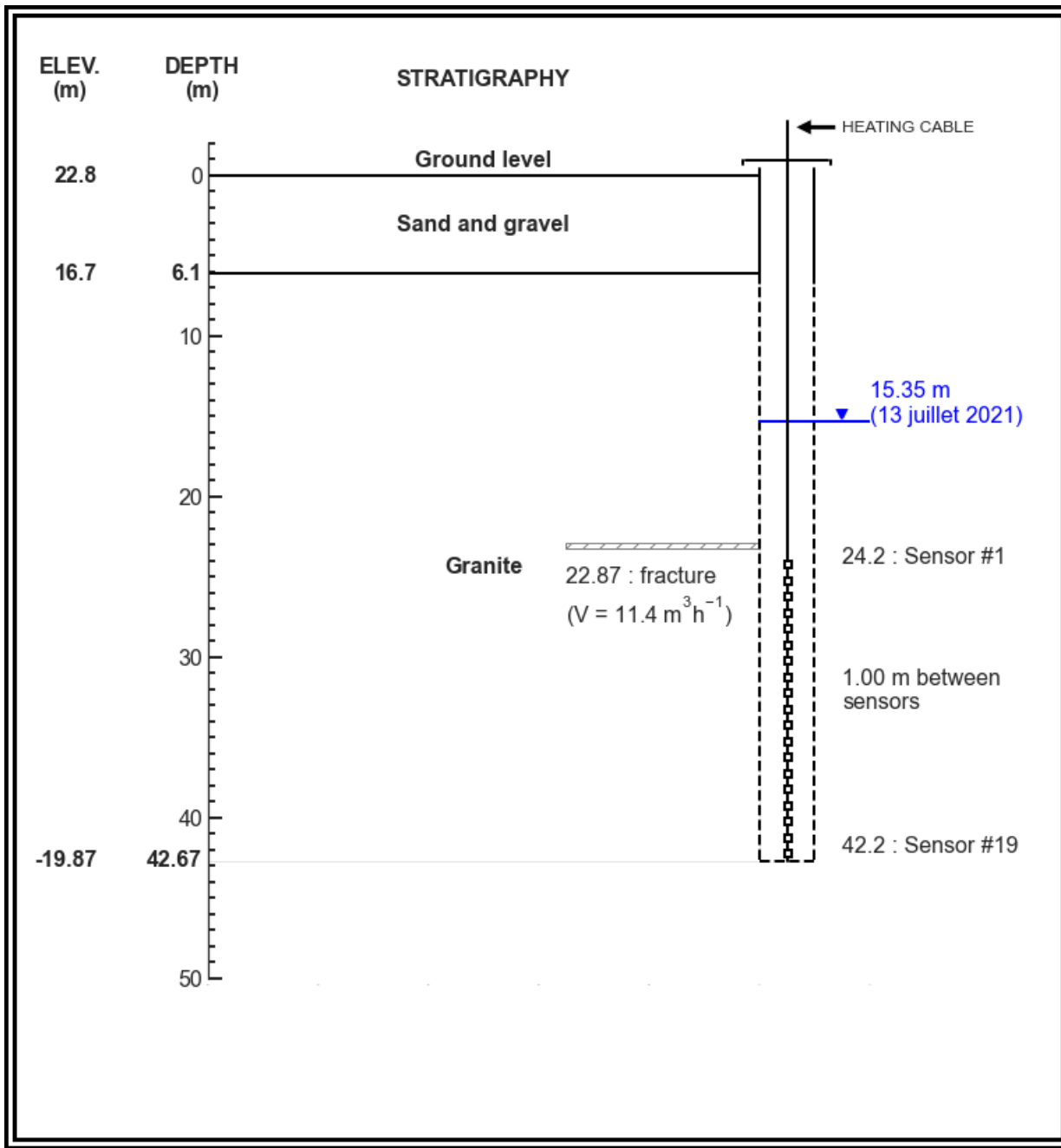


**Fig.VI.1:** Layout diagram of the constant thermal response test in the TF05-12 observation well.

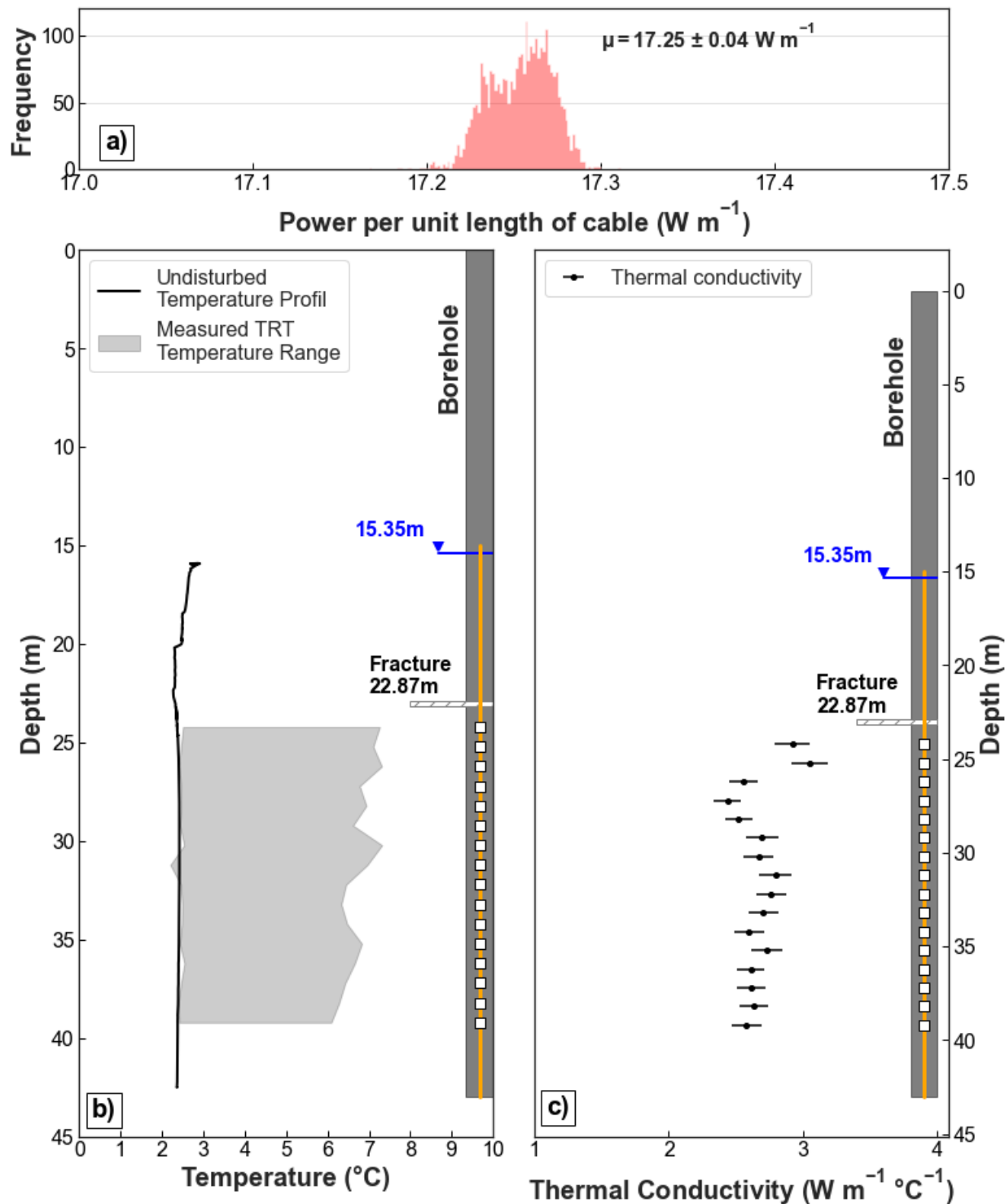


**Fig.VI.2:** Summary of the constant thermal response test showing a) calculated heat injection rate data, b) measured temperature data and c) calculated thermal conductivity for temperature sensors #1 to #16.